



DOTTORATO DI RICERCA IN FISICA

XXIII CICLO

# **Theoretical and Experimental Investigation of Single Spike Regime with the SPARC Free-Electron Laser**

Maurizio Serluca

A.A. 2010-2011

Tutor: Prof.D.Levi e Dott.M.Ferrario

Coordinatore: Prof.G.Altarelli

---

---

1. Reviewer:

2. Reviewer:

Day of the defense:

Signature from head of PhD committee:

---

# Contents

<b>List of Figures</b>	<b>iii</b>
<b>List of Tables</b>	<b>vii</b>
<b>1 Introduction</b>	<b>1</b>
<b>2 Free Electron Laser Theory</b>	<b>9</b>
2.1 One-dimensional Theory of Steady-State FELs . . . . .	10
2.1.1 Electron motion in an undulator . . . . .	10
2.1.2 The interaction of electrons with a radiation field in an undulator	13
2.1.3 Solution of one-dimensional FEL equations . . . . .	18
2.1.4 Nonlinear harmonics generation theory . . . . .	24
2.2 Three Dimensional Effects and 3D FEL Theory . . . . .	26
2.2.1 A scaling law for the three-dimensional effects in FEL: the Xie model . . . . .	28
2.3 1D Theory of Superradiance of FEL with Ultra-Short Electron Bunch and Single Spike . . . . .	29
2.4 FEL Radiation Properties: Transverse Coherence, Temporal Structure, Spectrum and Fluctuations . . . . .	35
<b>3 Charge Scaling Law for Single Spike Operation</b>	<b>39</b>
3.1 Charge Scaling Law and Slippage Effect in Short Electron Bunch . . . .	39
3.1.1 Single Spike start-to-end simulations at SPARC . . . . .	48
<b>4 Layout of the Free Electron Laser (FEL) SPARC</b>	<b>57</b>
4.1 SPARC Layout . . . . .	57
4.1.1 SPARC undulator system and FEL laser diagnostic . . . . .	62

## CONTENTS

---

<b>5</b>	<b>Production of Short Electron Bunches</b>	<b>67</b>
5.1	Electron Bunch from BLOW-OUT Regime . . . . .	68
5.2	Bunch Compression: Magnetic Chicane vs <b>V</b> elocity <b>B</b> unching (VB) . .	70
5.2.1	Experimental results of VB compression with emittance compensation at SPARC . . . . .	73
5.2.2	Results for VB compression of BLOW-OUT beam for Single Spike application at SPARC . . . . .	75
<b>6</b>	<b>Experimental and Simulation Results of SASE Single Spike FEL at SPARC</b>	<b>79</b>
6.1	Single Spike SASE at SPARC . . . . .	79
6.2	Single Spike SASE with Energy Chirped Electron Beam . . . . .	82
<b>7</b>	<b>Experimental and Simulation Results of Superradiant Single Spike in a HGHG-FEL</b>	<b>97</b>
7.1	Beam Characterization and SASE Simulation for SEED Experiments . .	98
7.2	Superradiant Spike Generation in HGHG SEED FEL . . . . .	99
	<b>References</b>	<b>111</b>

# List of Figures

1.1	Single Spike spectrum . . . . .	4
1.2	Experimental spectrum sequences . . . . .	5
2.1	Schematic cross section of a planar undulator . . . . .	11
2.2	Electron emission scheme in an undulator . . . . .	12
2.3	Undulator spontaneous radiation . . . . .	13
2.4	Longitudinal phase space . . . . .	15
2.5	Madey theorem graphical representation . . . . .	16
2.6	Slowly Varying Envelope . . . . .	17
2.7	FEL interaction cartoon . . . . .	19
2.8	Solution of the FEL dispersive relation vs detuning . . . . .	22
2.9	FEL gain and bunching evolution . . . . .	23
2.10	FEL field evolution . . . . .	24
2.11	SPARC 3D gain and power scaling of FEL from M.Xie model . . . . .	30
2.12	SASE FEL transverse profile along the undulator . . . . .	35
2.13	Temporal profile and spectrum of SASE-FEL . . . . .	36
3.1	Single Spike 1D charge scaling . . . . .	41
3.2	Single Spike 3D charge scaling . . . . .	41
3.3	Power profile evolution of a short electron bunch . . . . .	43
3.4	Power profile evolution of a long electron bunch . . . . .	44
3.5	Single Spike average energy growth along the undulator . . . . .	45
3.6	Normalized level curves of the power and spectrum for long bunch simulation . . . . .	46
3.7	Scaling of the peak power vs. the beam current . . . . .	47

## LIST OF FIGURES

---

3.8	Simulated electron longitudinal phase space: PARMELA output . . . . .	49
3.9	Power and energy evolution along z for 4 different electron bunches . . . . .	53
3.10	Power profile for 4 different electron bunches . . . . .	54
3.11	Scaling results of the 3D-number of spikes M . . . . .	56
4.1	SPARC layout . . . . .	58
4.2	SPARC laser system layout . . . . .	58
4.3	GUN Photo-cathode cartoon . . . . .	59
4.4	S-band SLAC-type accelerating section . . . . .	60
4.5	Magnetic elements of transfer line . . . . .	61
4.6	Undulator picture . . . . .	62
4.7	Harmonic generation chamber realized at CEA . . . . .	63
4.8	Seed and harmonics pulses generated in gas injection scheme . . . . .	64
4.9	Spectrometer . . . . .	64
4.10	Frequency resolved optical gating . . . . .	65
5.1	Main BLOW-OUT beam measurement at the end of the linac without VB compression . . . . .	69
5.2	Principle of longitudinal electron bunch compression in magnetic chicane	71
5.3	Velocity Bunching cartoon . . . . .	72
5.4	Simulated evolution of the main beam parameters . . . . .	74
5.5	Slice current and emittance for uncompressed beam . . . . .	75
5.6	Velocity Bunching compression results . . . . .	76
5.7	Beam parameter evolution: experimental results and PARMELA simu- lation . . . . .	76
5.8	Longitudinal phase-space and current profile of compressed bunch at SPARC . . . . .	77
6.1	Simulation results for an ideal Gaussian beam ( $L_b^{RMS} = 400\text{fs}$ ) lasing at 540 nm . . . . .	81
6.2	Simulation results for an ideal Gaussian beam ( $L_b^{RMS} = 400\text{fs}$ ) . . . . .	83
6.3	Chirp-taper cartoon scheme . . . . .	84
6.4	Longitudinal phase-space and current profile of compressed bunch at SPARC . . . . .	85



## LIST OF FIGURES

---

6.5	Experimental spectrum with three undulator sections closed . . . . .	86
6.6	Experimental spectrum at the exit of the untapered undulator . . . . .	87
6.7	Experimental histograms of the energy and the relative linewidth . . . . .	87
6.8	Genesis simulation evolution of chirped beam in untapered undulator . . .	88
6.9	Reconstructed spectrum by the simulated data for untapered undulator . .	89
6.10	Energy exponential gain: Genesis and experimental results . . . . .	90
6.11	Resonant wavelength for taper and untaper undulator . . . . .	90
6.12	Experimental histograms of the energy and the relative linewidth . . . . .	91
6.13	Experimental Single Spike spectrum . . . . .	92
6.14	Genesis simulation of chirped beam with tapered undulator . . . . .	93
6.15	Reconstructed spectrum by the simulated data for tapered undulator . . .	93
6.16	Energy vs bandwidth experimental results . . . . .	94
6.17	Comparison between experimental and simulated statistic results . . . . .	95
7.1	Simulated linewidth and power evolution of the harmonics in SASE at 400nm . . . . .	100
7.2	Spectrum of the seeded amplifier with different seed energy . . . . .	101
7.3	Overlap of some measured spectra at 400nm . . . . .	102
7.4	Reconstructed spectrum from simulation at 400 nm SEED FEL . . . . .	103
7.5	Experimental shot-to-shot energy of the SEED FEL at 400 nm . . . . .	103
7.6	Experimental spectrum of the HGHG FEL at SPARC . . . . .	104
7.7	Power pulse profile and longitudinal phase space with microbunching for the seed pulse FEL at saturation . . . . .	105
7.8	Experimental bandwidth and energy of the first eleven harmonics in HGHG at SPARC . . . . .	106
7.9	Simulated exponential gain of fundamental wavelength . . . . .	106
7.10	Genesis simulation for the fundamental and the third harmonics . . . . .	108
7.11	Energy of the first eleven harmonics: experimental and simulated . . . . .	109

## LIST OF FIGURES

---

# List of Tables

3.1	Correspondence between regions and parameters in Fig.3.2 . . . . .	42
3.2	Main bunch properties . . . . .	49
3.3	Table with the principal results. $\alpha$ : Cases where the secondary peaks are lower than half maximum value, $b_w$ is the normalized bandwidth . .	51
4.1	Electron beam parameters . . . . .	61
6.1	Ideal beam parameters . . . . .	80
6.2	Ideal beam results . . . . .	81
6.3	Compressed beam parameters . . . . .	86
7.1	Beam parameters for HGHG . . . . .	98
7.2	High harmonics in SASE regime results . . . . .	99

## LIST OF TABLES

---

# 1

## Introduction

In the last years ***F**ree **E**lectron **L**asers* (FEL) have demonstrated to be the main devices of the fourth generation of coherent radiation sources. First lasing at 1 Å wavelength and with a pulse duration in the femtosecond scale was observed at SLAC [1]. Free-electron lasers are based on the coherent emission of synchrotron radiation of relativistic electrons within an undulator or wiggler. The resonant radiation wavelength depends on the electron beam energy and can be tuned over the entire spectrum from micrometer to X-ray radiation. The basic regimes of operation are the FEL oscillator, the FEL amplifier (SEED FEL) and the **S**elf **A**mplified **S**pontaneous **E**mission (SASE)-FEL. The FEL oscillator device is composed by an undulator inside an optical cavity, the process is based on the multipass low gain amplification of the laser pulse interacting with the oscillating electron beam in the undulator. The minimum wavelength achievable is limited by the mirror reflectivity and breakdown.

The SEED-FEL regime, instead, is characterized by the amplification of a coherent seeding pulse in a single pass through a sufficiently long undulator. The output power level depends on the deviation of the mean energy of the electron beam from the resonant energy  $\gamma_R$ . The **S**elf **A**mplified **S**pontaneous **E**mission (SASE)-FEL, on the other hand, uses the broadband signal of the spontaneous emission to start the FEL amplification. A FEL pulse generated by SEED scheme is a full coherent pulse while the SASE is a quasi-coherent pulse. At the moment only the SASE regime is able to produce high power X-ray radiation, even if some techniques are promising to generate coherent seed at these short wavelengths. The lack in the coherence properties of SASE-FEL is in the longitudinal time structure where the pulse is composed by many regions (spikes)

## 1. INTRODUCTION

---

that are independently one from each others. This is due to the different velocity of the radiation and the electron beam. The electrons in the beam are causally connected only within the part of the beam, reached by the light emitted by themselves. Therefore the amplitude pulse at saturation is composed by many spikes and, of consequence, also the spectrum of the SASE-FEL has a multispike structure. To obtain a full coherent laser pulse a seed pulse is needed or, in SASE mode, it can be done with very short electron bunches, i.e. a bunch length as long as the region of the beam that radiates coherently due to the FEL interaction. The regime is called the Single Spike regime. The pulses generated are fully coherent, moreover given that the laser pulse length is comparable to the electron beam length, its duration can reach femtosecond scale. So these kind of pulses have many interesting properties: the connection with the SuperRadiant and soliton physics, the challenge in the production, manipulation and diagnostic of FEL ultra-short pulses and the ability to look the ultrafast and ultrasmall dynamics involved in matter physics, chemistry and biology[2].

This regime has become an interesting topic in FEL community in the last years due to the special properties of single spike pulses often requested by the users. The Single Spike regime is characterized by low charge bunch that allows to work with shorter bunches (higher current), very low emittance, reduced space-charge and wakefield effects. To obtain a single spike pulse for X-ray FEL the difficulties are due to the extremely short electron beams needed. Some techniques are based on the post-processing of the FEL pulse like 'pulse slicing' of a chirped SASE FEL pulse with a monochromator or the compression of the chirped pulse with optical dispersion, but the first is inefficient due to the high energy losses and the second has a wide band width. In Italy there are two FELs, one is SPARC (Sorgente Pulsata Autoamplificata di Radiazione Coerente) at Frascati, and the other is FERMI at Trieste that is developed to emit in the so-called water window(2-5 nm). The *SPARC* project [3] is a research and development experiment for high brightness electron beam photo-injectors (150 - 200 MeV), where the beam is characterized by short electron bunch with extremely low emittance  $\epsilon_n < 2$  mm-mrad and high current  $I > 100$ A, i.e. high brilliance  $B = 2I/\epsilon_n^2$ . The photo-injector guide a FEL device lasing from IR to UV wavelengths with a pulse duration from ps to fs range and can operate both in SEED or SASE FEL regime. This PhD thesis regards the theoretical and experimental analysis of the single spike regime at SPARC. For SPARC FEL lasing in the visible range, the single spike bunch length

---

is in the order of hundreds of fs. The generation of high brightness ultra-short electron beam is achieved at SPARC with the so called **V**elocity **B**unching (VB) technique [4]. The compression mechanism introduces a linear chirp in the electron bunch energy and the compression ratio must be chosen accurately in order to have the maximum brilliance. The resulting bunch is longer than the single spike length yet, but it has a peaked current shape combined with a strong linear chirp along the beam. With this kind of bunch we use the idea first proposed in Ref.[5], where short energy chirped electron beams are injected into a tapered undulator to compensate the chirp. This scheme allows to select the brightest region of the bunch to operate in the single spike regime. A theoretical investigation on the Single Spike regime at SPARC is presented in Ref.[6], where, imposing the single spike condition on beam length, a scaling law of the charge vs. the length of the beam is introduced in order to obtain the single spike pulse. The superradiant properties of the pulse by means of three-dimensional simulation are also investigated. All the FEL simulations are done with GENESIS[7] code. The real e-beam properties are taken into account in the start-to-end simulations, where the output of the accelerator simulation code are used as the input for the FEL simulations. For the theoretical paper on Single Spike regime I developed the focusing channel for the transport of the electron beam and the GENESIS simulations in order to compare the theoretical results against the simulated ones. The near future experiments of the SPARC collaboration are pump and probe experiments, X-ray production by Compton backscattering and experiments on plasma wave-based acceleration *PLASMONX*[8] and a newly proposed experiment **C**oherent plasma **O**scillation excitation by **M**ultiple electron **B**unches (*COMB*).

In the last years the main goals achieved by the *SPARC* team are the transport of the beam through the vacuum chamber up to the beam dump consistently with the matching condition in the undulators, the characterization of the spontaneous and stimulated radiation in the undulators and the demonstration of the "Velocity Bunching" technique in the linac with emittance compensation. All these steps were carried out during winter 2009, with the first SASE FEL spectra obtained on February 17th [9] and beam compression via velocity bunching with emittance compensation demonstrated in April 2009 [10]. In July 2009 a substantial increase of the extracted radiation from the FEL source was obtained with a longitudinally flat top e-beam by increasing the bunch charge. During 2008-2009 the data acquisition shifts were my training as

## 1. INTRODUCTION

---

a SPARC machine operator. I learned the software programs in order to check the SPARC machine status, to measure the beam parameters and to solve the inevitable hardware problems. My contribution to the last cited papers is mainly in the data acquisition. During 2009-2010 a comb beam with two bunches was characterized using VB technique and used for THz generation, the preliminary results are been published [11]. In May 2010 the first full coherent pulses of SASE-FEL in the so called "Single Spike" regime with the maximum energy ever obtain in SPARC were observed using an energy chirped electron beam compressed with VB technique and a tapered undulator configuration [12],[13](See Fig.1.1).

At the same time an intense activity on HGHG-SEED schemes, implemented with the

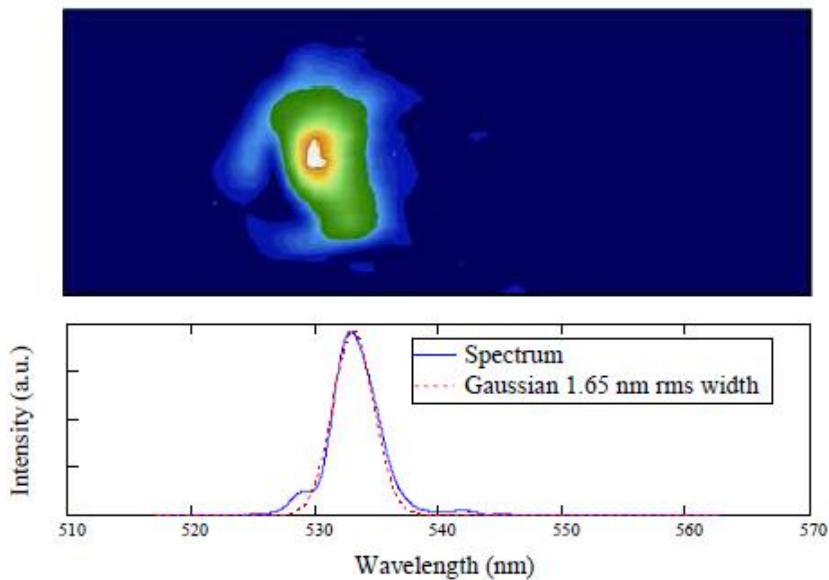


**Figure 1.1: Single Spike spectrum** - Typical spectrum showing a single coherent pulse

high harmonics generation in gas[14; 15] and the cascade configuration [16], was carried out and from the fundamental 400 nm wavelength and the fourth to eleventh harmonic wavelengths (36.18nm - 99.5nm) with energies in the  $\mu\text{J}$  -nJ range have been observed in June [16](See Fig.1.2). For the Single Spike Regime and the High Harmonics Generation in seeded FEL experiments I have collaborated to the planning, the seed laser system setup, the simulations, the data acquisition and analysis.



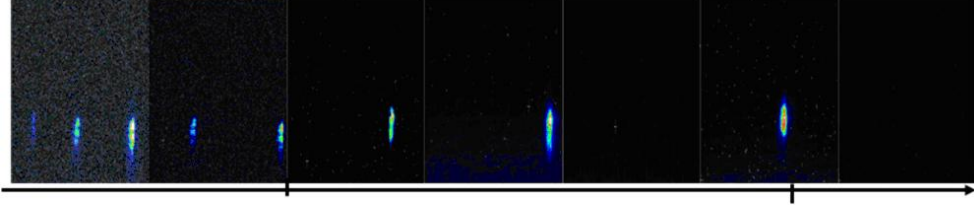


**Figure 1.2: Experimental spectrum sequences** - Spectrum from 32 up to 115 nm is shown with the presence of eight harmonics from 11th up to 4th from left (in sequence: 36.18 nm, 39.8nm, 44.2 nm, 49.75 nm, 58.6 nm, 66.3 nm, 79.6 nm, 99.5 nm).

The main topic of this thesis is a theoretical and experimental analysis of the FEL Single Spike Regime with ultra-short or energy chirped e-beam and the Superradiance evolution of short seed pulse during the interaction with a longer electron beam in the undulator. Starting from the 1-Dimensional theory of FEL with ultra short bunch and **SuperRadiant** SR-FEL it's possible to predict the behaviour of the laser properties and check them with the experimental results obtained in SPARC project. The 3D effects are evaluated with the help of the code GENESIS [7] and other numerical calculation. We have a theoretical estimate of three-dimensional effects [17] only for long electron bunch, then the theory is extended for short beam taking into account the effects from theory of the 1D SR-FEL. For this reasons a charge scaling law is introduced versus the beam length to predict the Single Spike operation parameters, moreover the possible effect is discussed due to the shortness of the electron beam that causes a superradiant stimulated emission given by the theory of SR-FEL. The theory and simulation results are then checked against the Single Spike SASE pulses obtained experimentally at SPARC, where we generate an energy chirped beam via VB technique and inject it into a tapered undulators scheme that allows a control of the beams interaction dynamics. In addition SEED-cascade regimes with seed pulse length lower than the electron bunch length are investigated for the superradiance evolution of the seed spike injected at the tail of the electron beam and slipping towards the head. The harmonics in the FEL pulses are ultra-short pulses in the UV range with sub- $\mu$ J energy. The experimental results are the spectrum and the energy content of the pulses and they are in a good agreement with the simulations and theory.

The outline of this Ph.D. thesis is as follow.

## 1. INTRODUCTION

---

In Chapter 2 are introduced the 1D steady state FEL theory, the 3D extension of the theory given by Xie, which is in a good agreement with simulations and experiments, and the superradiance theory of FEL.

In Chapter 3 the 3D effects are estimated in single spike FEL regime with the introduction of a charge scaling law that defines the relation between the charge and the beam length so that is possible to establish the number of longitudinal spikes in the FEL pulse. The analytical results are in good agreement with start-to-end simulation obtained with PARMELA and GENESIS simulations. The results has been accepted for publication in NIM [6].

In Chapter 4 a description of the main SPARC components is reported. After a brief introduction on the Ti:SA laser coupled to the copper photocathode, an analysis of acceleration cavities and undulator scheme is reported with the various techniques for electron and laser beam diagnostic. Finally are shown the undulator sections and the laser pulse diagnostic.

In Chapter 5 the techniques are introduced for the short beam generation on cathode the so called BLOW-OUT regime and the beam compression schemes: Velocity Bunching and magnetic chicane. The experimental results of the first compression technique used at SPARC are shown and they has been published in PRL[10].

In Chapter 6 the layout and the experimental results for the various regimes at SPARC are analyzed and compared with the simulation results and the theoretical predictions. Full Single Spike SASE operation has been achieved by combining the velocity bunching compression with an undulator tapering, to compensate the chirp in the longitudinal phase space. The interesting aspect of this regime is that the single spike can be achieved also with an electron beam longer than the single spike length. In fact, already in the visible range the single spike length is of the order of few hundreds fs while in the X-ray regime it can be lower than 1 fs. The simulation results show the same behaviour of the experiments with the formation of a single coherent spike, and the main parameters are almost the same. A paper with an analysis of the experimental

---

results and simulations is submitted for publication to PRL[13]

In Chapter 7 the seeded mode operation with harmonics generation is analyzed. The seed regime has been accomplished in a single amplifier with the input seed wavelength of 400nm and the amplification of the first eleven harmonic has been observed. The simulation results are in a good agreement with the main parameters for the odd harmonics powers, but for the even harmonics the simulated power are systematically lower than the experimental results. The results of single spike regime and HGHG have been presented at FEL conference 2010 [12; 16], a paper with an analysis of the experimental results and simulations will be submitted for publication to PRL.

## 1. INTRODUCTION

---

## 2

# Free Electron Laser Theory

In this chapter the FEL theory is introduced. The physics of FEL is described by a system of partial differential equations. Two approximations are often made in order to solve them. First, the **S**lowly **V**arying **E**nvelope **A**pproximation (SVEA) is introduced to reduce the second order derivate in Maxwell equation to a first order one. Second the steady-state approximation to drop the time derivate term in Maxwell equation, it can be thought of as an infinite long electron beam. The solution of the system of corresponding linear equations describes the exponential growth of the radiation power emitted by a slice of the infinite electron beam along the undulator. The numerical solution of the system of non-linear equations leads to an "universal scaling" law of the radiation power and describes the saturation of the radiation field amplitude by means of collective variables of the electron beam slice. Thus, effects due to the finite length of the electron pulse cannot be treated with the steady-state theory.

The chapter describes the dynamics of the electrons in the undulator and the interaction of the bunch with the radiation field in the low and high gain FEL regime. The solution of the steady-state model and the nonlinear harmonics generation are also presented. The 3-dimensional effects and the condition on beam parameters and the effects on the FEL performance are taking into account with the 3-dimensional extension of the FEL theory given by Xie[17]. The steady-state FEL theory describes a slice of the electron beam in the approximation of an infinite electron bunch, i.e. it describes the evolution of a single resonant mode of FEL laser. This approximation is valid as long as the bunch length is longer than the slippage length to estimate correctly the saturation power and length. To describe the temporal pulse profile along the whole beam the

## 2. FREE ELECTRON LASER THEORY

---

system of partial differential Eq. 2.32 must be solved without taking the steady-state approximation. The solution depends strongly on the ratio between e-bunch length and the cooperation length  $L_c$  (Eq.2.31), which depends on the properties of the electron beam and the undulator parameters. The typical cooperation length are roughly  $[10-300]\mu\text{m}$  in the visible FEL radiation and  $[10-100]\text{nm}$  in the X-ray FEL. The possible regimes are: the long pulse regime ( $L_B \gg L_c$ ), the single spike regime ( $L_B \sim 2\pi L_c$ ) (this interaction is described by the Superradiant regime of short bunch [18]), and slippage dominated regime ( $\lambda_r < L_B < L_c$ ) where the slippage is so significant that no steady-state region exists [19]. However for ( $L_B \leq \lambda_r$ ) the distribution of the electron beam can lead to the **C**oherent **S**pontaneous **E**mission (CSE) that enhances the FEL pulse properties. The electron bunch length definition depends on the electrons statistical distribution in the longitudinal phase space. For a flat top beam it is the length itself, for a gaussian one the length used as reference is the FWHM ( $2.35\sigma_z$ ).

### 2.1 One-dimensional Theory of Steady-State FELs

#### 2.1.1 Electron motion in an undulator

We consider a planar undulator for which the magnetic field is in the vertical y direction and varies sinusoidally along the z direction (See Fig.2.1):

$$B_y = B_0 \sin(k_u z). \quad (2.1)$$

Here  $k_u = 2\pi/\lambda_u$ ,  $\lambda_u$  is the undulator period, and  $B_0$  is the magnetic peak field on-axis.

A relativistic electron entering the undulator will oscillate periodically in the horizontal x direction due to the Lorentz force:

$$\frac{d(\gamma m \mathbf{v})}{dt} = -e(\mathbf{E} + \mathbf{v} \wedge \mathbf{B}). \quad (2.2)$$

It's convenient to change the independent variable from t to  $z = \beta_z c t$  to get:

$$\frac{d\gamma\beta}{dz} = -\frac{e}{mc^2\beta_z}(\mathbf{E} + \mathbf{v} \wedge \mathbf{B}). \quad (2.3)$$

The equation of the energy evolution of the electron is:

$$\frac{d\gamma}{dt} = -\frac{e}{mc}(\mathbf{E} \cdot \mathbf{v}) \quad (2.4)$$

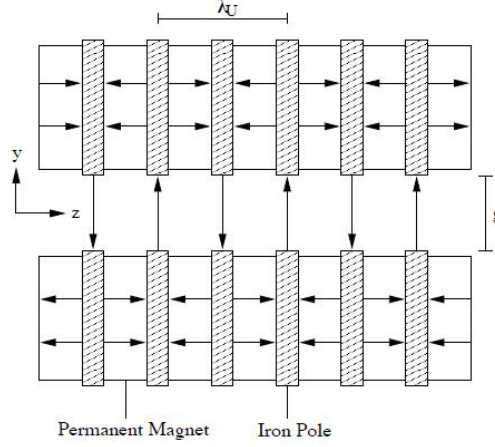


**Figure 2.1: Schematic cross section of a planar undulator** - Schematic cross section of a planar undulator with a gap width  $g$  and a periodicity  $\lambda_u$ . The direction of the magnetic field is indicated by arrows. credit figure [20]

and without an external electric field ( $\mathbf{E} = 0$ ) the  $\gamma$  value is constant:  $\gamma = \gamma_0$ .

The Eq.2.3 is reduced to

$$\frac{d\beta}{dz} = -\frac{e}{\gamma_0 mc \beta_z} (\beta \wedge \mathbf{B}). \quad (2.5)$$

The evolution of the x component of the electron velocity is dominantly given by

$$\frac{d\beta_x}{dz} = -\frac{e}{\gamma_0 mc \beta_z} (\beta_z \cdot B_y) = -\frac{eB_0}{\gamma_0 mc} \sin(k_u z). \quad (2.6)$$

The electron path and the x-velocity of the electron along the undulator can be found integrating the above differential equation:

$$v_x = -\frac{K}{\gamma_0} \cos(k_u z); \quad x(z) \approx -\frac{K}{\gamma_0 k_u} \sin(k_u z) \quad (2.7)$$

where  $K = eB_u/mck_u = 0.93B_u[T]\lambda_u[cm]$  is the dimensionless undulator strength parameter. Due to the energy conservation ( $\beta^2 = \beta_x^2 + \beta_z^2; \beta_y \approx 0$ ), the z-component of the velocity is:

$$\beta_z = \sqrt{1 - \beta_x^2 - \frac{1}{\gamma_0^2}} \approx 1 - \frac{1}{2\gamma_0^2} \left( 1 + \frac{K^2}{2} + \frac{K^2 \cos(2k_u z)}{2} \right) \quad (2.8)$$

and the average on the undulator period gives

$$\bar{v}_z = c - \frac{c}{2\gamma_0^2} \left( 1 + \frac{K^2}{2} \right). \quad (2.9)$$

## 2. FREE ELECTRON LASER THEORY

---

Due to the oscillation by the magnetic field the electron emits spontaneously radiation in the undulator(See. Fig.2.2).

There is a constructive interference if the optical delay path  $d$  is an integer multiple of

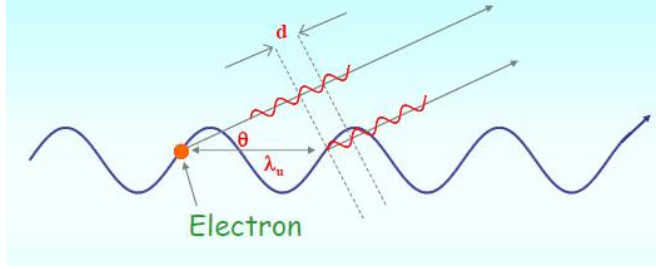


**Figure 2.2: Electron emission scheme in an undulator** - There is a constructive interference if the optical delay path  $d$  is an integer multiple of a given wavelength  $\lambda_r$

a given wavelength  $\lambda_r$ :

$$d = n\lambda_r = \frac{\lambda_u}{\beta_z} - \lambda_u \cos(\theta) \quad (2.10)$$

where  $n$  is the odd harmonic number and  $\theta$  is the observation angle relative to the undulator  $z$  axis. The emitted wavelength is found when substituting the average velocity  $\bar{v}_z$  (Eq.2.9) in Eq.2.10:

$$\lambda_r(n) = \frac{\lambda_u}{2n\gamma_0^2} \left( 1 + \frac{K^2}{2} + \gamma_0^2 \theta^2 \right) \quad (2.11)$$

This is the "resonance condition" of FEL, including the harmonics and the off-axis emission. For  $n=1$ , an electron passing an undulator with  $N_u$  periods produces a wavetrain with  $N_u$  periods. The time duration of the wave train is  $T = N_u \lambda_r / c$  and due to the finite duration the radiation is not monochromatic but contains a frequency spectrum which is obtained by Fourier transformation. The spectral intensity is

$$I(\omega) \propto \left( \frac{\sin \xi}{\xi} \right)^2 \quad \text{with} \quad \xi = \frac{\Delta \omega T}{2} = \pi N_u \frac{\omega - \omega_r}{\omega_r}. \quad (2.12)$$

It has a maximum at  $\omega = \omega_r = 2\pi/\lambda_r$  and a width proportional to  $1/N_u$  (See Fig.2.3). The total radiation power (integrated over frequency) is the same as in a bending magnet:

$$P_{rad} = \frac{2\alpha \hbar c^2 \gamma^4}{3r^2}, \quad (2.13)$$



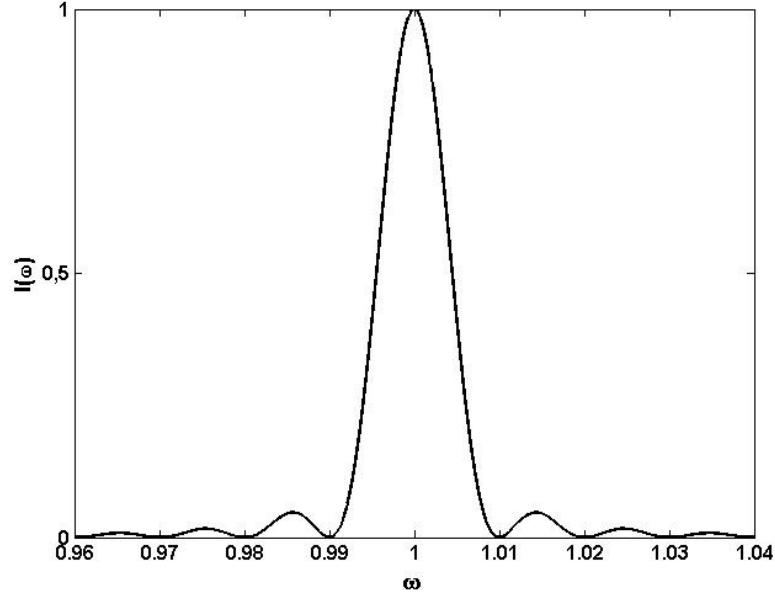


**Figure 2.3: Undulator spontaneous radiation** - Example of spectral intensity for a wave train with  $N_u = 100$  periods

where  $r = \beta E / (eB_0)$  is the radius of curvature. The main differences to synchrotron radiation in bending magnets are that undulator radiation is confined to a narrow spectral line and the radiation is well collimated. Note, however, that the synchrotron radiation emission is an incoherent process of emission (poissonian distribution of the time arrival of the electrons at the undulator entrance). Different electrons radiate independently both in bending magnets and in undulators, the total amplitude of the electric field is  $A = \sqrt{N_e} A_e$  ( $N_e$  is the electron numbers per bunch and  $A_e$  is the field emitted by one electron) and, hence, the intensity depends linearly on  $N_e$ :  $P_{tot} = N_e P_{rad}$ .

### 2.1.2 The interaction of electrons with a radiation field in an undulator

In the presence of a horizontal electric field  $E_x = E_0 \cos(kz - \omega t + \psi_0)$  with  $E_0, \psi_0$  are the initial amplitude and phase, the change in the electron energy is given by

$$mc^2 \frac{d\gamma}{dt} = ev_x E_x = \frac{eE_0 K}{2\gamma} \cos[(k + k_u)z - \omega t + \psi_0] + \cos[(k - k_u)z - \omega t + \psi_0] \quad (2.14)$$

## 2. FREE ELECTRON LASER THEORY

---

It is convenient to use the distance  $z$  from the undulator entrance as the independent variable and change the time variable to a phase variable relative to the EM wave:

$$\theta = (k + k_u)z - \omega\bar{t} \quad (2.15)$$

where  $\bar{t} = \int dz/\bar{v}_z$  is the electron arrival time averaged over the undulator period at  $z$ . The phase change can be calculated as

$$\frac{d\theta}{dz} = k + k_u - \frac{\omega}{\bar{v}_z} = k_u - k \frac{1 + K^2/2}{2\gamma^2} \quad (2.16)$$

Defining a relative energy variable  $\eta = (\gamma - \gamma_0)/\gamma_0$  and inserting the resonant condition (Eq.2.11) the last equation becomes:

$$\frac{d\theta}{dz} = 2k_u\eta \quad (2.17)$$

The electrons phase relative to the EM wave remains constant if its energy satisfies the resonant condition [i.e., Eq.2.11]. Thus, the first term on the right-hand side of Eq.2.14 varies slowly, contributing to the resonant energy exchange, while the second term varies quickly, with an oscillatory period  $\lambda_u/2$ . Properly taking into account the fact that the electrons longitudinal motion also has an oscillatory part as given in Eq.2.8; Eq.2.14 after retaining only the slowly varying part becomes:

$$\frac{d\eta}{dz} = \frac{eK_1}{2\gamma_0^2 mc^2} E_0 \cdot \cos(\theta + \psi_0), \quad (2.18)$$

where  $K_1 = K[JJ]$  is the first order of the effective coupling factor strength of the  $h^{th}$  harmonic  $K_h$ :

$$K_h = K(-1)^{(h-1)/2} [J_{(h-1)/2}(h\xi) - J_{(h+1)/2}(h\xi)] \quad (2.19)$$

where  $J_h$  is the Bessel function of order  $h$  with  $\xi = K^2/(4+2K^2)$  for a planar undulator trajectory. Equations 2.17 and 2.18, known as the pendulum equations, describe the motion of electrons under the influence of the ponderomotive potential due to the combined undulator and radiation fields [21]. The motion of electrons in the  $(\theta, \eta)$  phase space under the influence of the ponderomotive potential is illustrated in Fig.2.4. A nearly monoenergetic electron beam, satisfying the resonant condition, develops an energy modulation at the resonant wavelength according to Eq.2.18. After a certain undulator distance, the energy modulation causes a density modulation as the relative longitudinal position of an electron changes by an amount determined by its energy

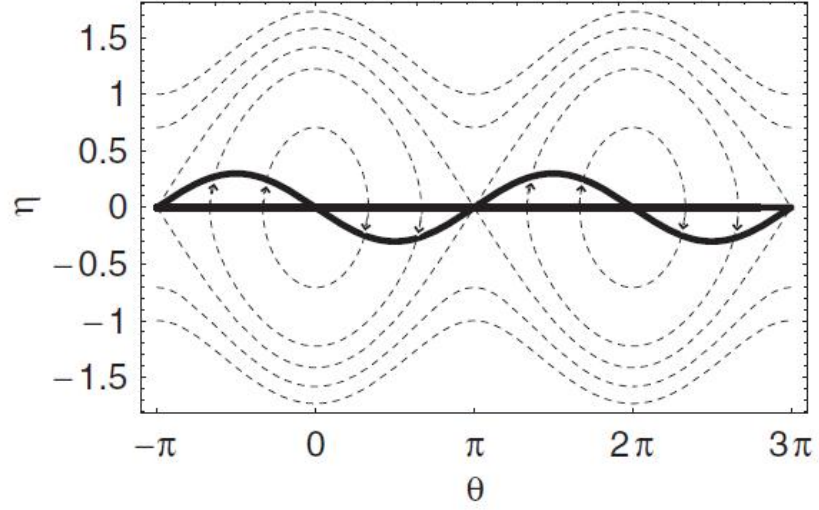


**Figure 2.4: Longitudinal phase space** - Electron motion in the longitudinal phase space  $(\theta, \eta)$  due to the presence of a resonant EM wave (with an initial phase  $\psi_0 = \pi/2$ ) in the undulator, in this picture  $\eta = (\gamma - \gamma_0)/(\rho\gamma_0)$  is normalized to the the Pierce parameter  $\rho$  defined in Eq.2.28. An initial distribution of the electron beam, shown as a straight line at  $\eta = 0$ , changes into a distribution on a sinusoidal line, implying that the energy and the density of the electron beam is modulated, i.e., microbunched. The dashed lines are the phase space trajectories.credit figure [22]

## 2. FREE ELECTRON LASER THEORY

---

deviation from the resonant energy [see Eq.2.17]. If the total energy gain in the undulator is a small fraction of the EM energy, the FEL is said to operate in the small-signal, low-gain regime. In this case, an FEL oscillator using an optical cavity together with many electron bunches is necessary to build up the radiation intensity. The total energy  $P_{Tot} = P_{EM} + P_{Beam}$  is conserved, thus  $\Delta P_{Beam} = -\Delta P_{EM}$ . In the Low Gain regime we have  $|\Delta P_{EM}| \ll P_{EM}$  per turn. The essential results in the FEL low-gain regime is given by [23]

$$G(\xi) = -\frac{\pi e^2 K^2 N_u^3 \lambda_u^2 n_e}{4\epsilon_0 m_e c^2 \gamma_r^3} \cdot \frac{d}{d\xi} \left( \frac{\sin^2 \xi}{\xi^2} \right) \quad (2.20)$$

where  $n_e$  is the electron density and  $\epsilon_0$  is the permeability of the vacuum. This results in the mathematical formulation of the Madey theorem: The FEL gain curve is obtained by taking the negative derivative of the line-shape curve (See Fig.2.5). For a sufficiently

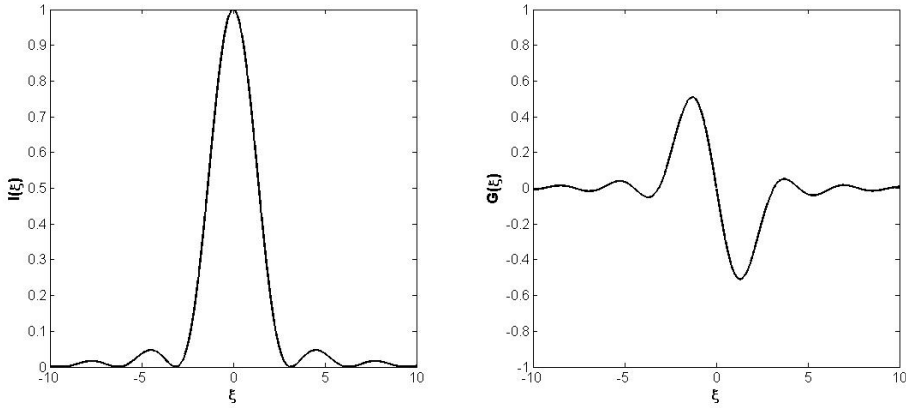


**Figure 2.5: Madey theorem graphical representation** - The FEL gain curve is the negative derivative of the spectral line-shape curve

bright electron beam and a sufficiently long undulator, the collective interaction of the beam-radiation system leads to an exponential growth of the radiation intensity along the undulator distance. In this regime the amplitude of the radiation field cannot be considered constant and a complete description of the interaction needs a self-consistent set of equations including the Maxwell equation for the field evolution.

The Maxwell equation can be simplified by assumption of the radiation field. Consider a single mode laser, and assume, as is almost reasonable, that the field amplitude  $E(t)$  has quasi sinusoidal quantities, with slowly varying envelope and phases referenced to

## 2.1 One-dimensional Theory of Steady-State FELs

some carrier frequency  $\omega$  (See Fig.2.6).

The SVEA merely says that the amplitudes and phases of all quantities vary slowly

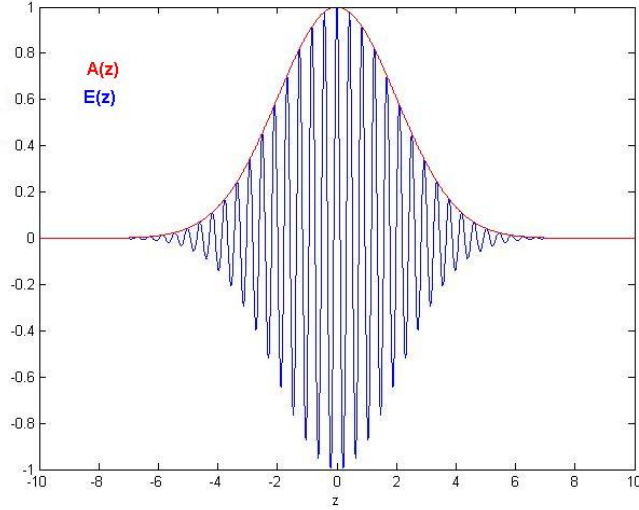


**Figure 2.6: Slowly Varying Envelope** - Here  $A(z)$  is the slow varying envelope

with respect to the optical carrier frequency  $\omega$  itself. This means that the SVEA can still accurately describe large signal or fast-pulse effects. It takes advantage of the fact that, as short as they are, most ultrashort laser pulses are still longer than an optical cycle (about 2 fs for visible wavelengths). Thus the electric field can be written as the product of the carrier wave and a relatively slowly varying envelope function. We write the electric field in terms of slowly varying envelopes[24]:

$$E(\mathbf{x}, t) = \frac{1}{2} A(\mathbf{x}, t) e^{i(\omega t - k z)} + c.c. \quad (2.21)$$

The wave equation calls for taking the second derivatives of  $A$  with respect to  $t$  and  $z$ :

$$\frac{\partial^2 E}{\partial^2 t} = \frac{1}{2} \left[ \frac{\partial^2 A}{\partial^2 t} + 2i\omega \frac{\partial A}{\partial t} - \omega^2 A \right] e^{i(\omega t - k z)} + c.c. \quad (2.22)$$

Assuming that derivatives are small and that derivatives of derivatives are even smaller:

$$\left| 2i\omega \frac{\partial A}{\partial t} \right| \ll |\omega^2 A|, \quad (2.23)$$

the term on the r.h.s. of the last equation vanishes with  $A \partial_z^2 e^{ikz - i\omega t}$ . Letting  $\omega = 2\pi/T$ , we find that this condition will be true as long as:

$$\left| 2 \frac{2\pi}{T} \frac{\partial A}{\partial t} \right| \ll \left| \frac{4\pi^2}{T^2} A \right| \quad (2.24)$$

## 2. FREE ELECTRON LASER THEORY

---

where  $T$  is the optical period of the light. These conditions hold if the field envelope is not changing on a time scale of a single cycle, which is nearly always true. So the smallest term can be neglected and we keep the larger two. The same is true for the spatial derivatives. The second spatial derivative of the electric field envelope can also be neglected.

The Maxwell wave equation for FEL interaction is:

$$\left[ \left( \frac{1}{c} \frac{\partial}{\partial t} \right)^2 - \left( \frac{\partial}{\partial z} \right)^2 - \nabla_{\perp}^2 \right] E_x(\mathbf{x}, t; z) = -\frac{1}{\epsilon_0 c^2} \left[ \frac{\partial j_{\perp}}{\partial t} \right] \quad (2.25)$$

where  $\nabla_{\perp}^2$  is the transverse Laplacian,  $\epsilon_0$  is the permittivity of free space,  $n_e$  is the electron volume density,

$$j_{\perp} = ev_x n_e = eK \cos(k_u z) \sum_{j=1}^{N_e} \frac{1}{\gamma_j} \delta[\mathbf{x} - \mathbf{x}_j(z)] \delta[t - t_j(z)] \quad (2.26)$$

is the transverse current, and  $N_e$  is the total number of electrons in the beam. We simplify the wave equation by using the SVEA, by changing the variable from  $t$  to  $\theta$  and by averaging the r.h.s. of the Maxwell equation properly over the fast wiggling motion to obtain[22]

$$\left[ \frac{\partial}{\partial z} + \frac{\nabla_{\perp}^2}{2ik_r} \right] A = -\frac{eK_1}{2\gamma_0 \epsilon_0} e^{-ik_u z} \int \frac{kd\theta}{2\pi} e^{-i\theta} \sum_{j=1}^{N_e} \delta(\mathbf{x} - \mathbf{x}_j) \delta(\theta - \theta_j), \quad (2.27)$$

$\theta_j$  is the position of the  $j^{th}$  electron relative to the bunch center in units of  $\lambda_r/(2\pi)$  at the undulator distance  $z$ . In the majority of FEL physics papers the SVEA is extensively used to describe the growth of the FEL radiation pulse. In fact the excited spectrum is considered to be very narrow around the resonant frequency and, as a consequence, the pulse can be pictured as a slowly modulated wave packet with a well-defined carrier frequency.

### 2.1.3 Solution of one-dimensional FEL equations

For a sufficiently bright electron beam and a sufficiently long undulator, the collective interaction of the beam-radiation system leads to an exponential growth of the radiation intensity along the undulator as illustrated in Fig.2.7. Such a high-gain FEL does not require any optical cavity and can amplify either an input seed signal or the

## 2.1 One-dimensional Theory of Steady-State FELs

spontaneous undulator radiation produced by the electron shot noise: SASE process. Both the radiation intensity and the electron beam microbunching reach a maximum saturation level (see Fig.2.7).

A fundamental scaling parameter for a high-gain FEL is the dimensionless Pierce pa-

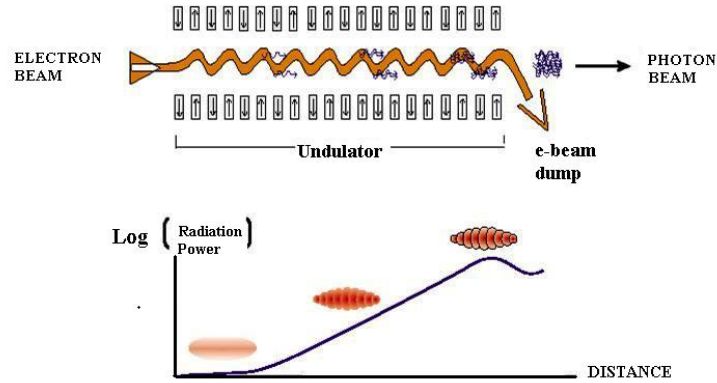


**Figure 2.7: FEL interaction cartoon** - The cartoon shows the exponential amplification and the microbunching of FEL power until the saturation

rameter  $\rho$  defined as in Ref.[25]:

$$\rho = \left[ \frac{1}{16} \frac{I}{I_A} \frac{K_1^2}{\gamma^3 \sigma_x^2 k_u^2} \right]^{\frac{1}{3}} \quad (2.28)$$

where  $K_1$  is the first order effective coupling factor [JJ] defined in Eq.2.19,  $I$  is the electron peak current,  $I_A = ec/r_e \approx 17kA$  is the Alfvén current,  $r_e = 2.8fm$  is the classical electron radius and  $\sigma_x$  is the rms transverse size of the electron beam. The fundamental scaling parameter  $\rho$  allows to define the one-dimensional power gain length of a mono-energetic beam:

$$L_G^{1D} = \frac{\lambda_u}{4\pi\rho} \quad (2.29)$$

The FEL interaction and the microbunching mechanism produce a slicing of the bunch at  $\lambda_r$  distance and a measure of this mechanism is given by the normalized microbunching parameter:

$$b = \frac{1}{N_e} \left| \sum_{j=1}^{N_e} e^{-i\theta_j} \right|. \quad (2.30)$$

## 2. FREE ELECTRON LASER THEORY

---

The coherence between the longitudinal slices is characterized by the cooperation length:

$$L_c^{1D} = \frac{\lambda_r}{4\pi\rho}, \quad (2.31)$$

that is a measure of the slippage of the radiation over the electron bunch in a gain length.

The FEL interaction can be described by the following system of partial differential equations:

$$\frac{\partial A}{\partial \bar{z}} + \frac{\partial A}{\partial \bar{z}_1} = b(\bar{z}, \bar{z}_1) \quad (2.32)$$

$$\frac{d\theta_j}{d\bar{z}} = p_j \quad (2.33)$$

$$\frac{dp_j}{d\bar{z}} \simeq -(Ae^{-i\theta_j} + c.c.) \quad (2.34)$$

where  $p_j = (\gamma_j - \gamma_r)/(\rho\gamma_r)$  is the mean energy variation of j-electron and

$$\bar{z}_1 = c \frac{z - \bar{v}_{\parallel} t}{\bar{v}_{\parallel} L_c} \quad (2.35)$$

$$\bar{z} = \frac{z}{L_g} \quad (2.36)$$

where  $\bar{v}_{\parallel}$  is the mean velocity of the electron bunch (see Eq.2.9).

The linear regime of the FEL is defined by the following periodic boundary condition:

$$A_0 \ll 1; \quad (2.37)$$

$$p_j = p_j^0 + p_j^1; \quad p_{j_0} = \delta,$$

$$\theta_j = \theta_j^0 + \theta_j^1; \quad \theta_j^1 \ll 1,$$

$\delta = (\langle \gamma \rangle - \gamma_r)/(\rho \langle \gamma \rangle)$  is the detuning parameter. The phase  $\theta_j$  is the sum of the equally spaced  $\theta_j^0$  and a small perturbation  $\theta_j^1$ , the mean energy variation is the sum of the detuning parameter and a small perturbation  $P_j^1$ . We introduce the collective variables  $b$  and  $P$  ( $\langle \dots \rangle$  is the average value):

$$b = \langle e^{-i\theta_j} \rangle \approx \langle -i\theta_j^1 e^{-i\theta_j^0} \rangle, \quad (2.38)$$

$$P = \langle p^1 e^{-i\theta_j^0} \rangle.$$



## 2.1 One-dimensional Theory of Steady-State FELs

---

The last approximation in the eq. 2.32 is the steady-state approximation that is equivalent to drop the partial derivative respect to  $\bar{z}_1$  in the SVEA equation ( $b(\bar{z}, \bar{z}_1) = b(\bar{z})$ ). The steady-state solution describes with the collective variables a slice of electron belonging to an infinite long electron beam. In this case one can see that the radiation field can only be a function of the distance through the undulator and no pulse effects can be present. The steady-state FEL equations are

$$\frac{db}{d\bar{z}} = -iP - i\delta b, \quad (2.39)$$

$$\frac{dP}{d\bar{z}} = -A + i\delta P, \quad (2.40)$$

$$\frac{dA}{d\bar{z}} = b(\bar{z}).$$

The solution of system of equations 2.39 depends on the detuning parameter  $\delta$ . First we find the zero detuning solution ( $\delta = 0$ ), i.e. only resonant electrons, by differentiating the linear equations:

$$\frac{d^2 A}{d\bar{z}^2} = \frac{db}{d\bar{z}} = -iP \quad \Rightarrow \quad \frac{d^3 A}{d\bar{z}^3} = -i \frac{dP}{d\bar{z}} = iA. \quad (2.41)$$

Looking for exponential solutions ( $A(\bar{z}) = A_0 e^{i\Lambda\bar{z}}$ ) we obtain a simple dispersion relation:

$$\Lambda^3 = -1 \quad (2.42)$$

$$\text{with the roots: } \Lambda_j = \left( 1; \left( \frac{1}{2} + i\frac{\sqrt{3}}{2} \right); \left( \frac{1}{2} - i\frac{\sqrt{3}}{2} \right) \right) \quad (2.43)$$

The solution is

$$A(\bar{z}) \simeq \frac{A_0}{3} \sum_{j=1}^3 e^{i\Lambda_j \bar{z}} \quad (2.44)$$

the real zeros of the dispersion relation are oscillating terms, while the imaginary parts give an exponential growth and an exponential decay. For  $\bar{z} > 1$  we have

$$A(\bar{z}) \approx \frac{A_0}{3} e^{\frac{\sqrt{3}}{2}\bar{z}}, \quad (2.45)$$

$A_0$  is the initial value of the seed normalized amplitude. If the detuning  $\delta$  is taking into account the dispersion relation became

$$\Lambda^3 - \delta\Lambda^2 + 1 = 0 \quad (2.46)$$

## 2. FREE ELECTRON LASER THEORY

---

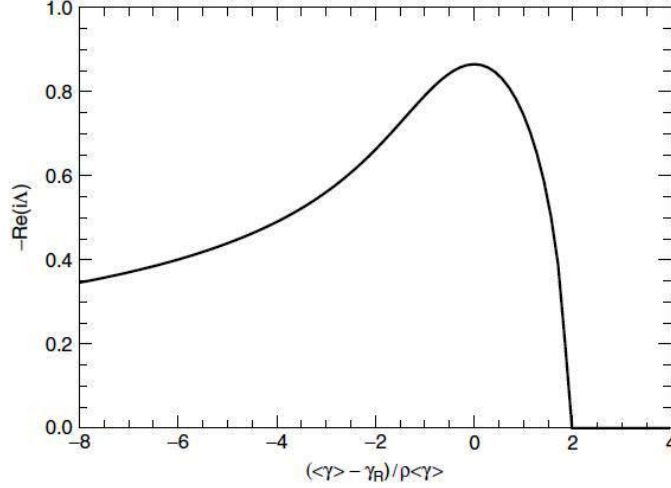


**Figure 2.8: Solution of the FEL dispersive relation vs detuning** - Growth rate of the FEL amplification as a function of the detuning-the deviation of the mean energy of the electron beam from the resonant energy.credit figure [20]

The equation 2.46 is the known cubic equation [25; 26]. The solution of the dispersive relation for the dominant growing mode is shown in Fig.2.8.

In Fig.2.9 the evolution is shown of the gain vs. the detuning  $\delta$  and the microbunching at resonant wavelength of the electrons along the undulator:

a) This picture shows the lethargy effects at the beginning of the first gain length, the gain is the low-gain of FEL and the interference of all 3 solutions dominates in the solution of FEL equation, the  $(z_1/\lambda_r, y)$  space below shows that the electron are randomly distributed on the  $\lambda_r$  scale. b) After two gain length the gain start to change it shape due to the modulation in energy, the solution is slightly dominated by the exponential term and in the  $(z_1/\lambda_r, y)$  space the electrons start to have a defined phase relationship. c) After some gain length the exponential term of the solution dominate and the power of the radiation grows exponentially along the undulator. The bunching factor is limited to  $|b| \leq 1$  and the power must saturate at a certain level. The nonlinear effects at this stage are relevant and can be studied by a quasi-linear extension of the linear theory [27]. A numerical solution of the non-linear equation shows a universal scaling of the squared amplitude of the radiation field (See Fig.2.10) that at saturation has a value close to one. After the saturation there is a cyclic energy exchange between the radiation field and the electron bunch. A SASE FEL uses the broadband signal of the

## 2.1 One-dimensional Theory of Steady-State FELs

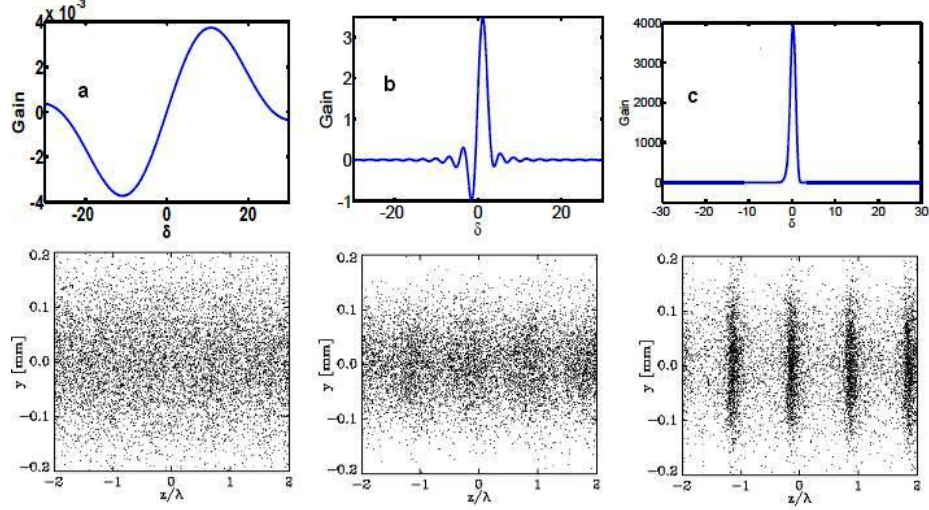


**Figure 2.9: FEL gain and bunching evolution** - From a to c the pictures show the evolution of the FEL gain vs. the detuning  $\delta$  and  $(z_1/\lambda_r, y)$  space during the lethargy or start-up process and the exponential gain. credit figure [20]

spontaneous emission to start the FEL amplification. Independent of the beam energy, the resonance condition is always fulfilled, but the SASE FEL amplifies all frequency components within the acceptance bandwidth of the FEL as well. The relative width is  $\Delta\omega/\omega \sim \rho$  and is typically much larger than the observed width of an FEL amplifier. The initial emission level of the spontaneous radiation depends on the fluctuation in the electron density. The effective power level, emitted because of spontaneous radiation and then further amplified by the FEL interaction, is called the "shot noise power" 2.48 [28].

$$P_{in} = 3\sqrt{4\pi}\rho^2 \frac{P_{beam}}{N_\lambda \sqrt{\ln|N_\lambda/\rho|}} \quad (2.47)$$

$$\text{with } N_\lambda = \frac{I\lambda_r}{ec}. \quad (2.48)$$

An FEL amplifier, seeded with a power signal smaller than the shot noise power level does not operate as an FEL amplifier but as an SASE FEL instead. Typical values are a few watts for free-electron lasers in the IR regime to a few kilowatts for FELs in the VUV and X-ray regime.

## 2. FREE ELECTRON LASER THEORY

---

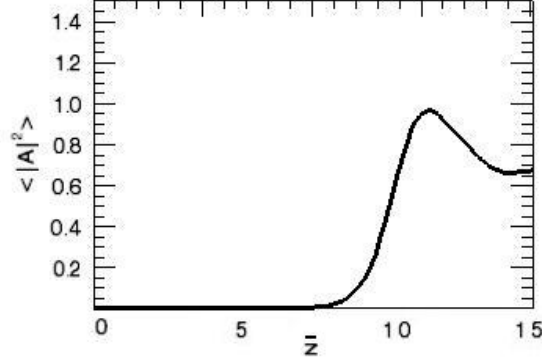


**Figure 2.10: FEL field evolution** - A numerical solution of the non-linear equation shows a universal scaling of the squared amplitude of the radiation field, that at saturation has a value close to one

The radiation power evolution and saturation are

$$P_{rad}(\bar{z}) \approx \frac{P_0}{9} e^{\sqrt{3}\bar{z}} \quad (2.49)$$

$$P_{SAT} = \rho |A|^2 P_{beam} \simeq \rho P_{beam} \quad (2.50)$$

where  $P_0 = P_{in}$  for the SASE regime or  $P_0 = P_{seed}(freeparameter)$  for the SEED regime and  $P_{beam}[W] = I[A] \cdot E[eV]$  is the electron beam power.

From the last two equations the saturation length for SASE regime is

$$L_{sat} \approx \frac{\ln(N_\lambda/\rho)}{\sqrt{3}} \sim 4\pi L_g \quad (2.51)$$

where  $N_\lambda$  is the number of electrons in a resonant wavelength. The bandwidth of SASE FEL at saturation is almost  $\rho$  with a decrease toward it as  $b_\omega \sim \sqrt{z^{-1}}$  (See Ref.[28]).

### 2.1.4 Nonlinear harmonics generation theory

The ability to generate coherent harmonic radiation is an important aspect of the FEL. When we change the dependent coordinate from  $t$  to  $\theta$  in the paraxial wave

## 2.1 One-dimensional Theory of Steady-State FELs

---

Eq.2.27, we should use the exact arrival time of the electron  $t = \bar{t} + (K^2/8ck_u\gamma^2)\sin(2k_uz)$ , and the relation

$$\theta(z) = (k_u + k)z - ck\bar{t} = (k_u + k)z - ckt + \xi\sin(2k_uz),$$

where  $\bar{t}$  is the undulator period averaged arrival time and  $\xi = K^2/(4 + 2K^2)$ . The Eq.2.27 is averaged over the undulator period with the help of the Bessel function expansion[22]

$$e^{i\nu\xi\sin(2k_uz)} = \sum_{p=-\infty}^{+\infty} J_p(\nu\xi)e^{i2pk_uz}. \quad (2.52)$$

This undulator period averaging is nonzero only when  $\nu$  is close to an odd integer  $h = 2p \pm 1$ , thus the harmonic field amplitude  $A_\nu(\mathbf{x}, z)$  at  $\nu \sim h$  is given by [22]

$$\left(\frac{\partial}{\partial z} + \frac{\nabla_\perp^2}{2ihk}\right) A_\nu(\mathbf{x}, z) = \frac{eK_h}{2\epsilon_0\gamma_0} e^{i\Delta\nu_h k_uz} \cdot \int \frac{kd\theta}{2\pi} e^{i\nu\theta} \sum_{j=1}^N \delta(\mathbf{x} - \mathbf{x}_j) \delta(\theta - \theta_j) \quad (2.53)$$

where  $K_h$  is the effective coupling strength of the  $h^{th}$  harmonic (see Eq.2.19) Thus, in the forward  $z$  direction, the electric field consists of a series of nearly monochromatic waves around the harmonic frequencies  $hck$ , with the frequency detuning  $\Delta\nu_h = \nu - h \ll 1$ . The FEL interaction introduces both energy and density modulations of the electron beam with the period  $\lambda_r$ . Close to saturation, strong bunching at the fundamental frequency  $\omega_r$  produces rich harmonic bunching and significant harmonic radiation in a planar undulator[29]. In the linear regime the harmonics experiences an asymptotic exponential growth and at the end of the undulator strong signals at harmonics wavelength are found both theoretically and experimentally. In general, the third harmonic radiation is the most significant harmonic component and can naturally extend the wavelength reach of the FEL by a factor of 3. The naturally synchronized fundamental and thirdharmonic radiation open up possibilities for two-color pump-probe experiments. Even harmonic radiation exists at an angle away from the undulator  $z$  axis. Although the microbunched electron beam at saturation contains more second-harmonic bunching than the third-harmonic bunching, the coupling strengths to even harmonic radiation are usually much weaker for x-ray FELs employing high-energy electrons[30]. For instance, the second harmonic radiation for the LCLS FEL is negligible. Nevertheless, the second harmonic radiation may still be significant for long wavelength FELs using relatively low-energy electron beams as experimentally observed in Refs.[31; 32].

## 2. FREE ELECTRON LASER THEORY

---

### 2.2 Three Dimensional Effects and 3D FEL Theory

The basic FEL process, as described previously, remains the same when 3-dimensional effects are included in the discussion, although the one-dimensional FEL parameter  $\rho$  (Eq.2.28) might not be valid anymore. However, an effective three-dimensional FEL parameter can be found. Two major effects contribute to the extended, three-dimensional model of the FEL process: the spread in the transverse velocity of the electron beam and the diffraction of the radiation field. A measure for the transverse spread in the electron beam is the normalized emittance  $\epsilon_n$ , which is the area covered by the electron beam distribution in the transverse phase space. It is invariant in linear beam optics. Focusing along the undulator is necessary to prevent the growth of the transverse electron beam size, reducing the electron density and decreasing the gain. Electrons that drift away from the axis are deflected back to the undulator axis. As a result, electrons perform an additional oscillation even slower than the 'slow' oscillation due to the periodic magnetic field of the undulator. Because part of the electron energy goes into this so-called betatron oscillation, the electron is slower in the longitudinal direction than an electron without a betatron oscillation. The spread in the betatron oscillation, which scales with the normalized emittance, has a similar impact as an energy spread. Thus, the requirement for the transverse emittance is

$$\epsilon_n < \frac{4\lambda_r \beta < \gamma >}{\lambda_u} \rho \quad (2.54)$$

where the beta-function  $\beta$  [33] is a measure for the beam size of the electron beam. Stronger focusing would increase the electron density ( $\beta$  becomes smaller) and consequently, the  $\rho$  parameter. But at the same time, the impact of the emittance effect is enhanced, reducing the amount of electrons that can stay in phase with the radiation field. It requires the optimization of the focusing strength to obtain the shortest possible gain length. A rough estimate for the optimum  $\beta$ -function is  $\beta = L_g^{1D} \approx \lambda_u/(4\pi\rho)$ . Inserting this into Eq.2.54 shows that the beam emittance  $\epsilon = \epsilon_n/\gamma$  has to be smaller than the photon beam 'emittance'  $\lambda_r/(4\pi)$ . If this condition is fulfilled, the electron beam does not diverge faster than the radiation field and all electrons stay within the radiation field. The betatron oscillation, which yields a change in the transverse position of the electron, contributes to the growth of transverse coherence as well. As a degrading effect, the radiation field escapes from the electron beam in the transverse

## 2.2 Three Dimensional Effects and 3D FEL Theory

---

direction. The field intensity at the location of the electron beam is reduced and the FEL amplification is inhibited. The compensation for field losses due to diffraction is the FEL amplification itself. After the lethargy regime, the FEL achieves equilibrium between diffraction and amplification. The transverse radiation profile becomes constant and the amplitude grows exponentially.

This 'quasi-focusing' of the radiation beam is called gain guiding [34] and the constant profile of the radiation field is an eigenmode of the FEL amplification. So in order for FEL devices to work, the radiation beam must be guided and focused by the electron beam, the so-called optical guiding [35]. There are two separate mechanisms which result in optical guiding: gain guiding and refractive guiding. Gain guiding occurs in any gain medium which is localized in the transverse direction. This mechanism is observed in conventional lasers, and it can be understood simply as light tending to be strongest where it is being amplified. Refractive guiding is analogous to propagation in an optical fibre, in which case a medium having a refractive index larger than unity is used to guide the light. The index of refraction is larger than unity in an FEL because of the electron bunching produced by the ponderomotive force. Refractive guiding can occur even after the FEL interaction has saturated and the radiation has ceased to grow. In the exponential gain regime of the FEL, both mechanisms are present. The index of refraction in a planar-wiggler FEL with an axially symmetric electron beam having a Gaussian radial density profile can be written as [36]:

$$n(r, z) = 1 + \frac{\omega_p^2(r)}{2\omega^2} \frac{K}{A(r, z)} \left\langle \frac{e^{-i\theta}}{\gamma} \right\rangle \quad (2.55)$$

where the angular brackets denote an average over the electron distribution and the average term depends on the radius  $r$ . Clearly, the index can exceed unity so that guiding can occur. In the exponential gain regime, gain guiding dominates and is strong enough to tightly focus the radiation. However, for  $\bar{z} \sim 4\pi$ , the FEL interaction begins to saturate, and gain guiding is no longer strong enough to provide focusing. Refractive guiding works only when the optical mode is smaller than the beam size, which is only the case for hard X-ray FELs. Otherwise refractive guiding is negligible. Similar to the eigenmodes of the freespace propagation of a radiation field (e.g., Gauss:Hermite modes), there are an infinite number of FEL eigenmodes [37]. Each couples differently to the electron beam and thus has a different growth rate or gain length. That mode, which has the largest growth rate, dominates after several gain lengths and, in the case

## 2. FREE ELECTRON LASER THEORY

---

of a SASE FEL, the radiation field becomes transversely coherent. At saturation gain guiding vanishes and the electron beams radiate into multiple modes. Typically, the fundamental FEL-eigenmode is similar to that of free space propagation and the resulting reduction in transverse coherence at saturation is negligible. The characteristic measures for diffraction and FEL amplification are the Rayleigh length  $z_R$  and gain length  $L_g^{1D}$ . To calculate  $z_R$ , we approximate the radiation size at its waist by the transverse electron beam size  $\Sigma$  as the effective size of the radiation source, resulting in  $z_R = k\Sigma/2$ . For  $z_R \ll L_g^{1D}$ , the FEL amplification is diffraction limited with a gain length significantly larger than that in the one-dimensional model. In the opposite limit ( $z_R > L_g^{1D}$ ), the one-dimensional model becomes valid.

### 2.2.1 A scaling law for the three-dimensional effects in FEL: the Xie model

In 1D theory if the value of Pierce parameter  $\rho$  increase then the gain length decreases and the saturation power of the FEL increases. Looking at the definition of  $\rho$ , given a resonant wavelength (constant beam energy), this can be done by increasing the current or decreasing the transverse size of the beam  $\sigma_r$ . Nevertheless the effective gain length is conditioned by the beam quality and diffraction loses and the scaling of the FEL gain and power change this behaviour. To taken into account these effects, it's useful to use the 3-dimensional Xie model of FEL [17]. The parameters of the model are:

$$\eta_d = \frac{L_g^{1D}}{Z_R} \quad \text{diffraction term} \quad (2.56)$$

$$\eta_\epsilon = \frac{4\pi\epsilon_n L_g^{1D}}{(\beta_T \gamma \lambda_r)} \quad \text{emittance term} \quad (2.57)$$

$$\eta_\gamma = \frac{4\pi\sigma_E L_g^{1D}}{\lambda_u} \quad \text{energy spread term} \quad (2.58)$$

where  $\beta_T[m]$  is the Twiss's parameter and  $\sigma_E = \Delta E/E$  is the normalized energy spread. The scaling law of the gain length:

$$L_g^{3D} = L_g^{1D} F(\eta_d, \eta_\epsilon, \eta_\gamma)$$



### 2.3 1D Theory of Superradiance of FEL with Ultra-Short Electron Bunch and Single Spike

---

is found with a fit on a numerical solution of the 3-dimensional FEL equations.

$$\eta = a_1\eta_d^{a_2} + a_3\eta_e^{a_4} + a_5\eta_\gamma^{a_6} + a_7\eta_e^{a_8}\eta_\gamma^{a_9} + a_{10}\eta_d^{a_{11}}\eta_\gamma^{a_{12}} + a_{13}\eta_e^{a_{15}}\eta_d^{a_{14}} + a_{16}\eta_e^{a_{18}}\eta_\gamma^{a_{19}}\eta_d^{a_{17}}$$

	$a_1 = 0.45$	$a_2 = 0.57$	$a_3 = 0.55$	$a_4 = 1.6$	$a_5 = 3$	$a_6 = 2$
	$a_7 = 0.35$	$a_8 = 2.9$	$a_9 = 2.4$	$a_{10} = 51$	$a_{11} = 0.95$	$a_{12} = 3$
where	$a_{13} = 5.4$	$a_{14} = 0.7$	$a_{15} = 1.9$	$a_{16} = 1140$	$a_{17} = 2.2$	$a_{18} = 2.9$
	$a_{19} = 3.2$					

The 3-dimensional parameters are given by

$$L_g^{3D} = (1 + \eta) \cdot L_g^{1D} \quad (2.59)$$

$$P_{sat} = \frac{1.6\rho \cdot E \cdot I_p}{(1 + \eta)^2} \quad (2.60)$$

$$L_{sat} \simeq 4\pi \cdot L_g^{3D} \quad (2.61)$$

This model allows to find the shortest gain length admissible for a variable parameter of the beam or its transport. As example, varying the Twiss's parameter  $\beta_T$ , i.e. varying the magnetic fields of the beam transport lattice, the scaling of the gain length and saturation power (see Fig.2.11) have, respectively a minimum and a maximum at a value of the  $\beta_T$  that can be found numerically or in the simplest case analitically. The scaling of the FEL performance with others beam parameters are included in the model as well. In the next chapter we will introduce the scaling of the bunch charge vs. its length in order to predict the number of spikes in the pulse in the 3-dimensional FEL theory.

### 2.3 1D Theory of Superradiance of FEL with Ultra-Short Electron Bunch and Single Spike

The Superradiance concept was introduced by Dicke [38] in 1954, he describes it as " an effect can convert disordered energy of various kinds into coherent electromagnetic energy". The Superradiance is a macroscopic collective emission of an ensemble of excited elementary sources. The maximum intensity of the emitted light scales with square of the number of the elementary sources  $P_{tot} \sim N^2 P_s$ . This happens when there is a fixed phase relationship between them, i.e. coherence. When the source is

## 2. FREE ELECTRON LASER THEORY

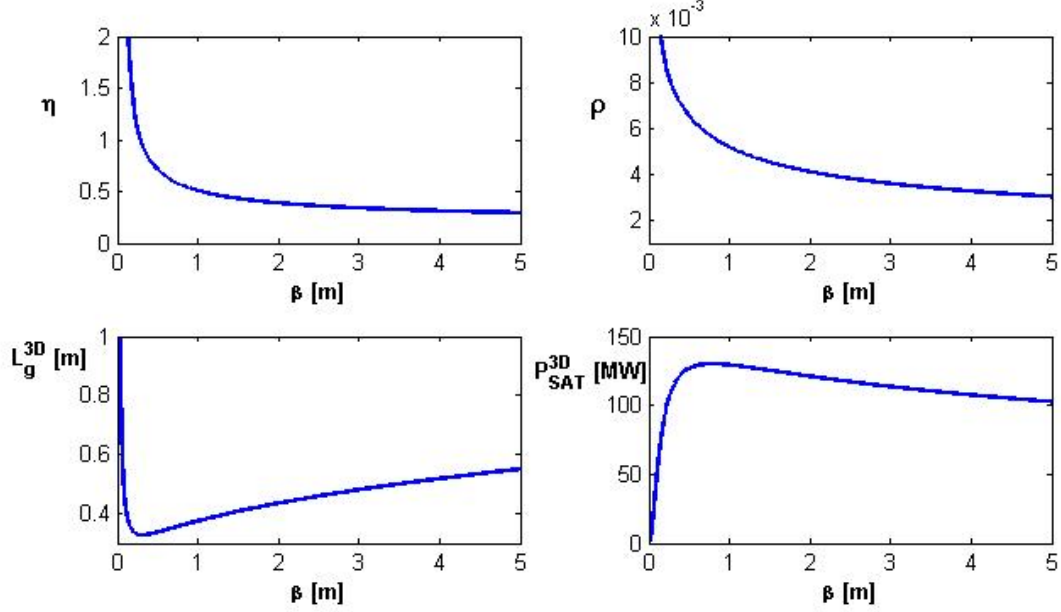


**Figure 2.11: SPARC 3D gain and power scaling of FEL from M.Xie model -** The pictures show the scaling of the fundamental FEL parameters ( $\eta, \rho, L_g^{3D}, P_{SAT}^{3D}$ ) vs. the Twiss parameter  $\beta_T$

composed by relativistic electrons oscillating in an undulator the superradiance nature of the emission depends on the beam characteristics, the wavelength of the emitted radiation and the FEL regime. The  $N$  elementary sources within a distance smaller than the emitted wavelength are a macroscopic coherent source. For the FEL the situation is slightly different, in the transverse plane the coherence properties depends on the emittance of the beams and due to the optical guiding the SASE FEL can reach almost a perfect transverse coherence. In the longitudinal direction if the electrons are separated by exactly one or multiple  $\lambda_r$  the emission sums up coherently (constructive interference), this happens due to the combined effects of collective instabilities, that "bunch" the beam at the resonant wavelength and the slippage of the radiation over the electron bunch. The slippage is due to the different velocity of the e-beam ( $v_{//} \simeq 1 - \frac{1-K^2/2}{2\gamma^2}$ ) and the light ( $v=c$ ), after an undulator period the difference path is given by

$$c\Delta T = \lambda_u - \frac{c\lambda_u}{v_{//}} \simeq -\lambda_r \quad (2.62)$$

### 2.3 1D Theory of Superradiance of FEL with Ultra-Short Electron Bunch and Single Spike

---

After a gain length the radiation slips over the bunch of a cooperation length and for the whole undulator the total slippage is

$$L_S = N_u \lambda_r \quad (2.63)$$

When the beam length is a few resonant wavelengths the FEL interaction is dominated by the strong slippage and the dominant contribution to the power is carried by the radiation that escapes through the leading edge of electron beam. Therefore the final length pulse is as long as the slippage length, and it has low power and a multiple-spikes spectrum. Until the e-beam length is of the order of a cooperation length the situation is similar but in this situation a contribution to the emission comes from the CSE emission. Analytically this can be shown solving the Maxwell-Klimontovich equation [39] or with a multi-frequency approach to the FEL equations[40]. The effect is due to the fast change in the gradients of electrons longitudinal distribution. The length for a single temporal spike is, as defined for the first time by R.Bonifacio in Ref.[19] by numerical solution of 1D FEL equation,

$$L_{SS}^{1D} \approx 2\pi L_c^{1D}. \quad (2.64)$$

Taking into account the relation between the undulator wavelength and the Pierce parameter  $\rho$  ( $N_u \sim 1/\rho$ ), follows that the single spike length is simply the half of the slippage length  $L_{SS}^{1D} = L_S/2$ . The single spike regime occurs when the radiation emitted by the electrons, travelling from the tail towards the head of the beam, covers all the distance inside the bunch in a time shorter than few gain times, correlating all the electrons of the beam during the emission process itself. This regime, called also weak super-radiance, has been widely studied theoretically and numerically in the 1d approximation[41], and has deserved also attention from an experimental point of view, with experiments [42; 43] that have confirmed its occurrence and its properties. A regime at very low charge is being studied at LCLS with application to production of X-rays [43]. Another characteristic of the single spike emission, pointed out in Refs.[19; 41], is that the peak radiation power scales with the charge like  $Q^2$ , i.e. superradiance emission, contrarily to the usual long bunch regime.

In 1-dimensional model the Single Spike length  $L_{SS}^{1D}$  is the shortest e-beam length which allows to obtain a fully coherent pulse with ultra-short superradiant spike emission. A detailed description about the evolution of the single spike regime is discussed at the

## 2. FREE ELECTRON LASER THEORY

---

end of the next section after a theoretical description of the solution of FEL equations for superradiance. For long e-beam ( $L_B \gg L_c$ ), the usual 1D steady-state theory accurately describes the evolution of the correlation and optical power [19; 34]. In the steady-state theory of FEL the power of the electron slice at saturation is  $P_{sat} \approx \rho P_{beam} \sim N_e^{1/3} \cdot N_e \sim N_e^{4/3}$ , which shows the collective emission nature of FEL emission. Taking into account the slippage and the length of the bunch we have a regime of superradiance for bunch length of order of the single spike e-bunch length for the SASE regime[18]. For this regime the scaling of the power is  $P_{sat} \sim N_e^2$ . Instead, for SEED regime using short seed pulses and a long e-beam, the superradiant pulse evolution can be observed when the pulse at saturation starts to slip over the bunch at  $c$  velocity, extracting other energy by the fresh electrons behind it. The theoretical analysis follows the Ref.[18; 41]. As shown in the last chapter, the linear regime can be described by this system of partial differential equations 2.32:

$$\frac{\partial A}{\partial \bar{z}} + \frac{\partial A}{\partial z_1} = b + i\delta A \quad (2.65)$$

$$\frac{b}{\partial \bar{z}} = -iP \quad (2.66)$$

$$\frac{\partial P}{\partial \bar{z}} \simeq -A \quad (2.67)$$

The boundary condition for  $b$ ,  $P$  and  $A$  are  $b(z_1, \bar{z} = 0) = b_o$ ,  $P(z_1, \bar{z} = 0) = 0$ , the FEL start up from noise in the electron distribution (SASE) if the initial field amplitude  $A_0$  is 0, the interaction can be simulated by a small initial bunching coefficient  $b_0$ . Hence the boundary condition for the field are  $A(z_1, \bar{z} = 0) = b(z_1 = 0, \bar{z}) = 0$ . Solving the system of equation 2.65 by using the Laplace transform in  $\bar{z}$  for the transformed field

$$\bar{A}(\omega, z_1) = \int_0^\infty d\bar{z} e^{-\omega \bar{z}} A(z_1, \bar{z}) \quad (2.68)$$

we obtain the results:

$$\bar{A}(\omega, z_1) = \bar{A}_S(\omega) + \bar{A}_1(\omega, z_1), \quad (2.69)$$

$$\bar{A}_S(\omega) = -b_o \frac{\omega}{\Delta(\omega)}, \quad (2.70)$$

$$\bar{A}_1(\omega, z_1) = b_0 \frac{\omega}{\Delta(\omega)} e^{-i\Delta(\omega)/\omega z_1} \quad (2.71)$$

### 2.3 1D Theory of Superradiance of FEL with Ultra-Short Electron Bunch and Single Spike

---

where  $\Delta(\omega) = \omega^3 - \delta\omega^2 + 1$  is the usual FEL characteristic equation.  $\bar{A}_S$  is the solution of the linear regime in steady-state limit, the fields is a sum of three modes:

$$A_S(\bar{z}) = -ib_0 \sum_{j=1}^3 \frac{e^{i\omega_j \bar{z}}}{3\omega_j - 2\delta} \quad (2.72)$$

one of which is unstable for values of detuning parameter  $\delta$ .  $\bar{A}_1$  has the same singularities and in an essential singularity  $\omega = 0$ . By inversion of the Laplace transform,  $\bar{A}_1$  gives

$$A_1(\bar{z}, z_1) = e^{i\delta z_1} \frac{b_0}{2\pi} \int_B d\omega \frac{\omega}{\Delta(\omega)} e^{\omega(\bar{z}-z_1) - i\frac{z_1}{\omega^2}}, \quad (2.73)$$

where the integration contour B is parallel to the real axis and lies below all the singularities of  $\bar{A}_1$ . For  $z_1 > \bar{z}$  B can be closed in the lower half plane and the integral vanishes, the complex field amplitude A is given by  $\bar{A}_1$ . For  $z_1 < \bar{z}$ , the counter must be closed in the upper half plane and the integral is given by  $2\pi i$  times the residues at the singularities of the function  $\bar{A}_1$ . In this case we have  $A_1 = -A_S + A_{SR}$  and  $A = A_{SR}$ , where

$$A_{SR} = e^{i\delta z_1} \frac{b_0}{2\pi} \oint_{C_0} d\omega \frac{\omega}{\Delta\omega} e^{i\omega z_2 - i\frac{z_1}{\omega^2}}, \quad (2.74)$$

where  $z_2 = \bar{z} - z_1$  and  $C_0$  is the counterclockwise path enclosing the singularity  $\omega = 0$  but excluding the simple poles. Introducing  $y = \sqrt{z_1}(z_1 - \bar{z})$ , the integral may be estimated asymptotically for large y, by using the stationary-phase method. Keeping only the amplifying exponential solution, we obtain

$$A_{SR} \simeq \frac{b_0}{\sqrt{3\pi}} \frac{e^{i\delta z_1}}{y} \frac{z_1}{Q(z_1, z_2)} e^{\frac{3}{2}(\sqrt{3}+i)(\frac{y}{2})^{2/3} - \frac{i\pi}{4}}, \quad (2.75)$$

where

$$Q = 1 + \delta e^{i\pi/3} \left( \frac{2z_1}{z_2} \right)^{2/3} - \frac{2z_1}{z_2}.$$

In the strong slippage limit ( $L_S > L_b$ ) and in the linear regime,  $A_{SR} = z_1 \exp(i\delta z_1) A_1(y)$  and  $b_{SR} = b_1(y)$ . It assumed the same self-similar structure to be valid in the nonlinear regime:

$$A = z_1 e^{i\delta z_1} A_1(y) \quad (2.76)$$

$$\theta_j = \theta_{1j}(y) - \delta z_1 \quad (2.77)$$

$$p_j = \sqrt{z_1} p_{1j}(y) \quad (2.78)$$

## 2. FREE ELECTRON LASER THEORY

---

The system of partial differential equations 2.65 reduces to the following ordinary differential system:

$$\frac{d\theta_j}{dy} = p_{1j}, \quad (2.79)$$

$$\frac{dp_{1j}}{dy} = -[A_1 e^{i\theta_{1j}} + c.c.], \quad (2.80)$$

$$\frac{y}{2} \frac{dA_1}{dy} + A_1 = \langle e^{-i\theta_1} \rangle. \quad (2.81)$$

The solution does not depend on  $z_1$  and  $\delta$ , but only by the initial condition. It follows that  $|A|^2 \propto z_1^2 \propto \rho^2$  and the peak intensity scales as  $|E|^2 \propto \rho N_e |A|^2 \propto N_e \rho^3 \sim N_e^2$ . The width of the pulse scales as  $\bar{z}^{-1/2}$ , i.e. the inverse of the square root of the peak field. Numerical solution of system 2.65 plotted vs  $y$  are in a good agreement with the solution of self-similar equation:

$$|A_1|^2 = \frac{1}{y} \text{Sech}^2 \left[ \frac{3\sqrt{3}}{2} \left( \frac{y}{2} \right)^{2/3} + \log \left( \frac{|b_0|}{2\sqrt{e\pi y}} \right) \right]. \quad (2.82)$$

After the saturation the beam continues to extract energy by the electron bunch emitting others peaks that have a different resonant wavelength due to the lost energy carried out by the first peak of emission. So in this situation the growing of the energy can be stopped at the first saturation to obtain a single spike pulse with a low bandwidth or the multispikes emission with more energy but higher bandwidth in the next undulator sections. For the SEED-FEL case the superradiance can be observed in the amplification of the power of the seed pulse and its shape evolution. Using a seed pulse we obtain a fully coherent pulse, the amplification behaviour depends on the power and length of the seed pulse. For seed power lower than the noise power the interaction is essentially a SASE process while for higher seed power the amplification starts and reaches the saturation in a distance that depends on the ratio between the input and the saturation power. If the seed is shorter than the electron bunch its evolution is characterized by an amplification stage in which the pulse peak slips with a velocity  $v_s$  [19]:

$$v_s = \frac{3v_{\parallel}}{2 + v_{\parallel}/c} \quad (2.83)$$

## 2.4 FEL Radiation Properties: Transverse Coherence, Temporal Structure, Spectrum and Fluctuations

---

over the electron bunch. At saturation the pulse starts to slip with the velocity of light over the electron bunch and compressing its width while its energy continues to grow thanks to the fresh electrons in front of the pulse.

## 2.4 FEL Radiation Properties: Transverse Coherence, Temporal Structure, Spectrum and Fluctuations

The development of the transverse and longitudinal coherence of the FEL SASE pulse along the undulator is discussed in this section. Due to the optical guiding, the SASE FEL can reach the full transverse coherence before saturation. This happens when the emittance of the electron beam  $\epsilon$  is smaller than the diffraction-limited radiation emittance  $\epsilon_{r0} = \lambda_r/(4\pi)$ . Figure 2.12 shows the evolution of the LCLS angular patterns at different  $z$  locations. At the initial start-up, the beam excites many transverse modes, and the radiation is dominated by incoherent spontaneous emission ( $\epsilon_r \approx \epsilon$ )(Fig.2.12(a)).

The mode pattern cleans up in the exponential gain due to the optical guiding (Fig.2.12(b)).

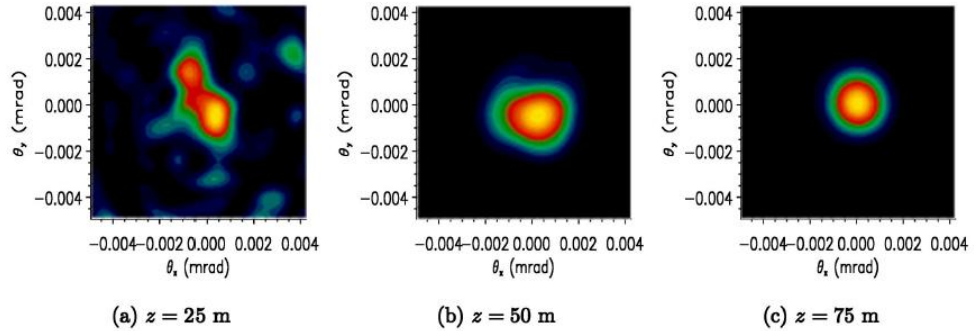


**Figure 2.12: SASE FEL transverse profile along the undulator** - Example of evolution of the transverse profiles at different  $z$  locations: LCLS case(credit figure[22])

Near saturation, the guided fundamental mode dominates the radiation pattern (Fig.2.12(c)) and the radiation emittance  $\epsilon_r$  is almost  $\epsilon_{r0}$ . The transverse mode parameter is defined as[22]

$$M_T^2 = \left( \frac{\epsilon_r}{\epsilon_{r0}} \right) \quad (2.84)$$

## 2. FREE ELECTRON LASER THEORY

then  $M_T^2 \gg 1$  at the start-up stage and decreases slightly above unity at saturation. For beam with non-ideal parameters the transverse coherence mode size and divergence require numerical solution of FEL equations.

The temporal structures of the pulse depend by the electron bunch length  $L_B$  and the Single Spike length  $L_{SS}^{1D}$ . For electron beam much longer than the Single Spike length, the radiation profile contains many spikes. The spikes are also present in the frequency spectrum as shown in Fig.2.13(LCLS case).

The origin is the random fluctuation in the beam density. The shot-to-shot fluctuation

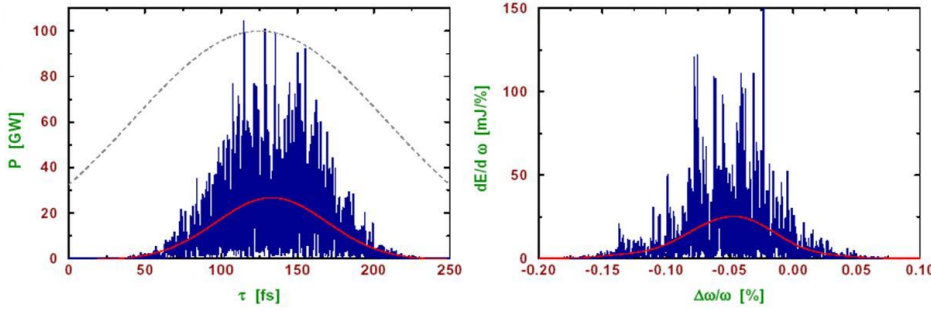


**Figure 2.13: Temporal profile and spectrum of SASE-FEL** - The plots show the many spikes for a simulation of SASE-FEL lasing in Ångstrom range. For UV-optical FELs the number of spikes decrease but the fluctuations in energy increase

in the radiation pulse energy follows a Gamma distribution [44]:

$$W = \frac{\Sigma}{Z_0} \int_{-\infty}^{\infty} |E(z, t)|^2 dt \quad (2.85)$$

$$p(W) = \frac{M^M}{\Gamma(M)} \frac{W^{M-1}}{\langle W \rangle^M} e^{-M \frac{W}{\langle W \rangle}} \quad (2.86)$$

with  $M = 1/\sigma_W^2$  ( $\sigma_W$  is the fluctuation of the radiation energy) and  $\Gamma(M)$  as the gamma function. The only free parameter of this distribution,  $M$ , is the product of transverse and longitudinal modes:  $M = M_T \cdot M_L$ . If  $M_T = 1$  (transverse coherence) then  $M$  can be interpreted as the number of the spikes in the radiation pulse. The gamma distribution is identical with a negative exponential distribution if the independent parameter  $M$  is equal to unity. For  $M > 1$  the distribution peaks at the mean value of the negative exponential distribution and the relative root-mean square width narrows as  $1/\sqrt{M}$ . In the limit  $M \rightarrow +\infty$  the probability distribution becomes a Gaussian distribution.



## 2.4 FEL Radiation Properties: Transverse Coherence, Temporal Structure, Spectrum and Fluctuations

---

The length of the spikes is approximately  $2\pi L_c^{1D}$  [19].

For  $M_T = 1$  a shorter pulse would result in a larger fluctuation of the radiation energy. The fluctuation of the instantaneous power is given by a negative exponential distribution. The shortest pulse duration achievable is based on the Fourier transformation limit that defines the shortest pulse duration which is possible for a given optical spectrum of a pulse. A pulse at this limit is called transform limited. The condition of being at the transform limit is essentially equivalent to the condition of a frequency-independent spectral phase (which leads to the maximum possible peak power), and basically implies that the timebandwidth product is at its minimum and that there is no chirp. The minimum timebandwidth product of a pulse is the product of its temporal duration and spectral width (in frequency space). The minimum timebandwidth product depends on the pulse shape, and is e.g.  $\sim 0.315$  for bandwidth-limited  $\text{sech}^2$ -shaped pulses and  $\sim 0.44$  for Gaussian-shaped pulses (These values hold when a full-width-at-half-maximum criterion is used for the temporal and spectral width). For a Gaussian-shape pulse then we have  $\Delta\omega \cdot \tau \sim 0.44$ , the minimum of the FEL bandwidth at saturation is  $\rho$ , so we can compute the minimum length of the FEL pulse to be transform limit:

$$c\tau \sim 0.44 \frac{\lambda_r}{2\pi\rho} \approx L_c.$$

So for a FEL at saturation the pulse length should be as long as a cooperation length to achieve the transform limit value. The temporal property of the SASE pulse can be tailored to a given application by suitable manipulations. One is the use of frequency chirped SASE pulse generated by an energy chirped electron bunch followed by monochomator[45]. Nevertheless, it is pointed out in Ref.[5], that the FEL gain degradation due to a linear energy chirp can be perfectly compensated for by a proper taper of the undulator parameter. Thus, a tapered undulator can automatically select a small fraction of an energy-modulated bunch that has the right chirp with a pulse duration of fs in visible, UV range and hundreds of attoseconds in x-ray range. This technique is been followed by SPARC team for the generation of single spike pulse in visible range [12](See Chap.6.2) for description of the technique and the experimental results). In order to provide fully coherent FEL pulses, the intrinsic noise of the SASE radiation must be overcome with some form of seeding. The **H**igh-**G**ain **H**armonic **G**eneration (HGHG) FEL relies on a coherent seed at subharmonic wavelengths. In

## 2. FREE ELECTRON LASER THEORY

---

this scheme[46], a small energy modulation is imposed on the electron beam by interaction with a seed laser in a short undulator (the modulator). The energy modulation is converted to a coherent spatial density modulation as the electron beam traverses a dispersive section. A second undulator (the radiator), tuned to a higher harmonic of the seed frequency, causes the microbunched electron beam to emit coherent radiation at that harmonic frequency. This shorter-wavelength radiation may then be used as the coherent seed to the next stage HGHG. Single-stage HGHGs at infrared and ultraviolet wavelengths have been demonstrated at Brookhaven National Laboratory [47]. The HGHG technique is implemented in SPARC project with the harmonics pulses generated in gas [14; 15] and in cascade scheme. Another scheme is the Self-seeding FEL [48] that improve the temporal coherence using two undulators (of the same undulator period and strength) and a monochromator located between them. The first undulator operates in the exponential gain regime of a SASE FEL. After the exit of the first undulator, the electron beam is guided through a dispersive bypass that smears out the microbunching induced in the first undulator. The SASE output enters the monochromator, which selects a narrow band of radiation. At the entrance of the second undulator the monochromatic beam is combined with the electron beam and is amplified up to the saturation level. Since the SASE power over a narrow bandwidth at the exit of the first undulator fluctuates 100% for a single mode, the length of the second undulator is chosen to exceed the saturation length sufficiently to suppress fluctuation of the final output power level. Thus, this approach requires an undulator system almost twice as long as a single-stage SASE FEL.

## 3

# Charge Scaling Law for Single Spike Operation

In this chapter we analyse the extension of the 3-dimensional effects on FEL interaction evolution for SASE regime with short electron bunch length. Applying the Xie model to the FEL theory we use the 3D-scaling law of Ref. [49] to analyze the scaling of the charge vs bunch length for single spike regime. The scaling is applied at SPARC, the results are checked then against Genesis1.3 simulations [7]. The study of single-spike ultra-short radiation in the X rays range[50], as well as in the visible light [49], by means of start-to-end simulations from the photocathode to the end of the undulator, has shown that transverse and non-homogeneity effects due to radiation diffraction, and to non-ideal characteristics of the electron beam, like, for instance, emittance and energy spread, have a strong impact on the performance of the free-electron laser.

### 3.1 Charge Scaling Law and Slippage Effect in Short Electron Bunch

The dependence of the saturation power on the current  $I$  of the beam follows the  $P \sim I^{4/3}$  law and the longitudinal structure of the power profile presents a sequence of several chaotic peaks whose number is  $M \approx L_B/(2\pi L_c)$ , separated by a distance of about  $2\pi L_c$ , each width being therefore shorter than  $2\pi L_c$ . From the Xie model is possible to evaluate the degrading effects on the gain length and power given by

### 3. CHARGE SCALING LAW FOR SINGLE SPIKE OPERATION

---

non-ideal beam parameters:

$$L_g^{3D} = L_g^{1D} \cdot (1 + \eta), \quad (3.1)$$

$$L_c^{3D} = L_c^{1D} \cdot (1 + \eta), \quad (3.2)$$

$$L_b^{3D} \simeq 2\pi L_c^{1D} \cdot (1 + \eta), \quad (3.3)$$

$$P_{sat}^{3D} = \frac{1.6\rho \cdot P_{beam}}{(1 + \eta)^2}, \quad (3.4)$$

$$L_{sat}^{3D} \simeq 4\pi \cdot L_g^{3D}. \quad (3.5)$$

We define a 3D single spike condition as

$$L_B = 2\pi L_c^{1D}(1 + \eta), \quad (3.6)$$

inserting this expression in the charge definition we obtain

$$Q = \left( \frac{\pi^2 I_a}{3\sqrt{3}c} \right) \left( \frac{\lambda_u \sigma^2 (1 + K^2/2)^3}{K^2 J J^2 \gamma^3} \right) \left( \frac{(1 + \eta)^3}{L_B^2} \right) \quad (3.7)$$

$$M = \frac{L_B}{2\pi L_c^{1D}(1 + \eta)} \quad (3.8)$$

now M is the 3D spike number.

In 1D theory the scaling of the bunch charge vs the beam length is simply given by the definition of the current and Pierce parameter  $\rho$ :

$$Q \leq \left( \frac{\pi^2 I_A}{3\sqrt{3}c} \right) \left( \frac{\lambda_u}{2K^2 [J J^2]} \right) \left( \frac{\sigma_x^2}{L_B^2 \gamma^3} \right) (1 + K^2)^3. \quad (3.9)$$

The plot of this 1D-relation for a set of typical values of the SPARC injector and undulator, namely,  $K=1.47$ ,  $\lambda_u = 2.8\text{cm}$ ,  $\gamma_R = 306$ ,  $\lambda_R = 474\text{nm}$ , is shown in Fig.3.1. In the 3D case the scaling of the charge vs. the beam length, for different sets of values of emittance, energy spread and radiation diffraction, is shown in Fig.3.2. The single spike operation regions for the various parameters are represented in the figure by the coloured areas down to the axes. All the values of the parameters with their connection to the regions presented in the picture, are shown in Table 3.1. The other parameters are taken as in the reference case.

In Fig.3.2(a) the effect of the radiation diffraction is shown, considering various values of the r.m.s. radius of the electron beam. As can be seen, the effect of the variation, of  $\sigma_x$  is not strong, an increase of a factor 6 in the radius corresponding, with these parameters, to a moderate increase in the dimension of single spike operation region.

### 3.1 Charge Scaling Law and Slippage Effect in Short Electron Bunch

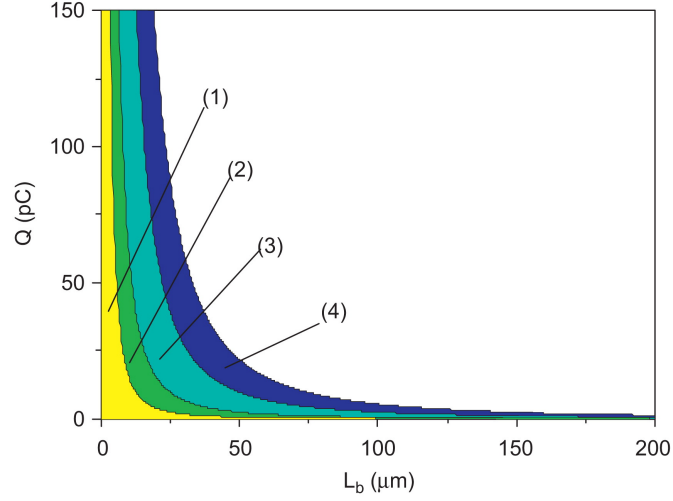


**Figure 3.1: Single Spike 1D charge scaling** - Single Spike condition of  $Q[\text{pC}]$  vs  $L_B[\mu\text{m}]$   $K=1.47$ ,  $\lambda_u = 2.8\text{cm}$ ,  $\gamma_R = 306$ ,  $\lambda_R = 473\text{nm}$ , (1)  $\sigma_x = 50\mu\text{m}$  (blue), (2)  $\sigma_x = 100\mu\text{m}$  (green), (3)  $\sigma_x = 200\mu\text{m}$  (cyan) and (4)  $\sigma_x = 300\mu\text{m}$  (yellow)

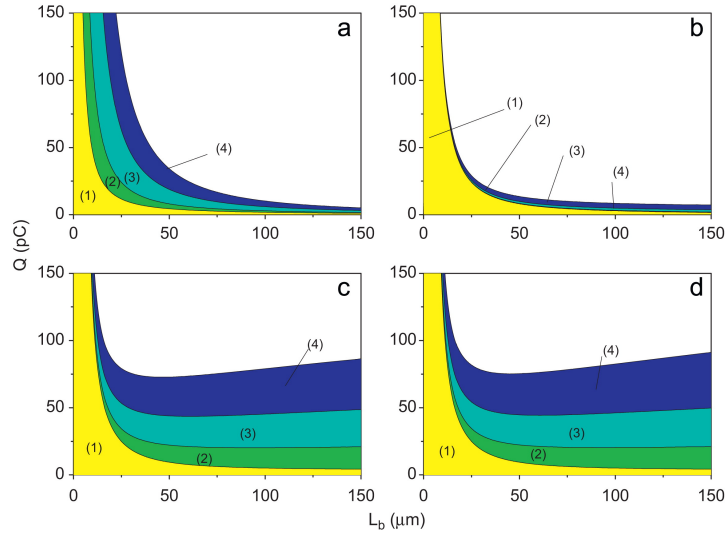


**Figure 3.2: Single Spike 3D charge scaling** -  $Q[\text{pC}]$  versus  $L_b[\mu\text{m}]$  for the parameters of Table 3.1 and (a) effect of the radiation diffraction, (b) effect of emittance, (c) effect of the energy spread and (d) combined effect of energy spread and emittance

### 3. CHARGE SCALING LAW FOR SINGLE SPIKE OPERATION

Number	Colour	(a) $\sigma_x, \epsilon_{nx}, \sigma_\gamma$	(b) $\sigma_x, \epsilon_{nx}, \sigma_\gamma$	(c) $\sigma_x, \epsilon_{nx}, \sigma_\gamma$	(d) $\sigma_x, \epsilon_{nx}, \sigma_\gamma$
1	Yellow	50,0,0	50,0.5,0	50,0,0.0005	50,0.5,0.0005
2	Green	100,0,0	50,1.5,0	50,0,0.0015	50,1.5,0.0015
3	Cyan	200,0,0	50,2.5,0	50,0,0.0025	50,2.5,0.0025
4	Blue	300,0,0	50,3.5,0	50,0,0.0035	50,3.5,0.0035

**Table 3.1:** Correspondence between regions and parameters in Fig.3.2

In addition we can say that these curves in this range are very similar to the corresponding 1D ones, shown in Fig.3.1. Fig.3.2(b) shows the effect of the emittance  $\epsilon_n$  at  $\sigma_x$  constant at the value  $\sigma_x = 50\mu\text{m}$  and with no energy spread. As can be seen, in the  $\epsilon_n$  range between (0.5-3.5[mm-mrad]), the change in the single spike operation region is not very strong. Much more considerable is the effect of the energy spread, alone or combined with emittance. Fig.3.2(c) shows the effect of the energy spread for negligible emittance and for  $\sigma_x = 50\mu\text{m}$ , and Fig.3.2(d) the combined effect of increasing emittance and energy spread.

As a general comment on the three-dimensional single spike scaling law, we can say that all those effects, accounted by the factor  $\eta$ , that produce an increase in the co-operation length, drive the occurrence of the single spike shape, while, at the same time, contribute to a decrease of the radiation power. The most important differences between the one-dimensional and the three-dimensional cases are: first, an increase in the single spike operation area due to the presence of emittance and energy spread. Secondly, in the 3D cases, the value of  $Q$  corresponding to the single spike condition does not tend to zero when  $L_B$  is going to infinity like  $L_B^{-2}$ , but, after a minimum  $Q_{min}$ , increases again. Third, the occurrence of a regime of single spike emission at low current with small radiation power. In the 1D model, keeping a fixed value for the charge and increasing the beam length, one passes from single to multiple spikes condition, and the regime of single spike is limited to very short bunches or very low charges. In the 3D model, instead, if  $Q$  is fixed to a value  $Q < Q_{min}$ , two values of charge satisfy condition 3.8, one at small values of  $L_B$ , large current, and high gain and one at large  $L_B$ , low current, and small radiation power. If  $Q$  is fixed instead at values  $Q > Q_{min}$ , the radiation occurs always in single spike condition. The theoretical charge scaling law is tested with 3D simulation, all the simulations have been made with GENESIS1.3[7]. The undulator polarization is linear, with an undulator parameter  $K=1.47$  and a period  $\lambda_u=2.8$  cm and the radiation wavelength is  $\lambda_r=474$  nm.

### 3.1 Charge Scaling Law and Slippage Effect in Short Electron Bunch

Fig.3.3 gives snapshots of the power  $P$  versus the bunch coordinate  $s$ , taken at various

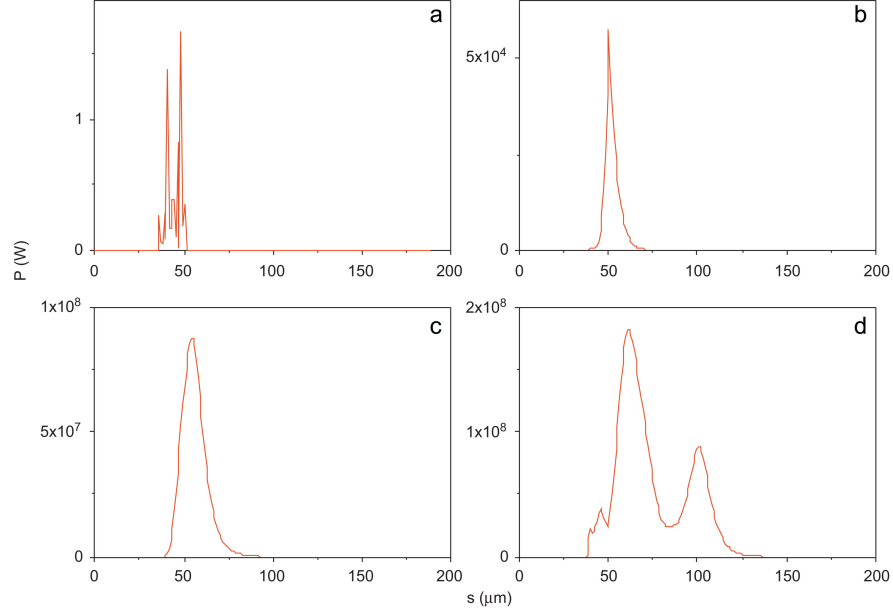


**Figure 3.3: Power profile evolution of a short electron bunch** - (a) Power[W] versus the coordinate along the bunch [ $\mu\text{m}$ ] at the beginning of the process, (b) at  $z=2$  m, (c) at  $z=4.75$  m and (d) at  $z=7.5$  m. Other data are:  $I=1500$  A,  $L_B = 9\mu\text{m}$ ,  $\sigma_x = 50\mu\text{m}$ ,  $K=1.511$ ,  $\lambda_u=2.8$  cm,  $\lambda_r=474$  nm.

positions  $z$  along the undulator. It shows the cleaning up of the power signal from the initial spiky shape (window(a)) to the attainment of one neat peak(window(c)) at saturation, as predicted by the single spike scaling law. The subsequent insurgence of non-linear effects with the development of a structure of multiple peaks is shown in Fig.3.3(d).

In Figs.3.4 and 3.5 the second reference case is shown. This case is more realistic, at least with respect to the values of current and beam length. In Fig.3.4, snapshots of the  $P$  versus  $s$  are presented at different times. In this case we are not properly in the single spike regime, but in a transition regime between the single spike occurrence and the long bunch case, characterized by few peaks. Fig.3.5 presents the total energy  $E$  versus the coordinate  $z$ . The saturation process occurs in two steps. First, at  $z=5$  m, the power reaches the maximum value inside the bunch at about 1.2 GW, and this point corresponds to a change of slope in the  $E$  versus  $z$  graph (point(a) in Fig.3.5). Afterwards, due to the slippage, the radiation exits from the leading edge of the beam.

### 3. CHARGE SCALING LAW FOR SINGLE SPIKE OPERATION

---

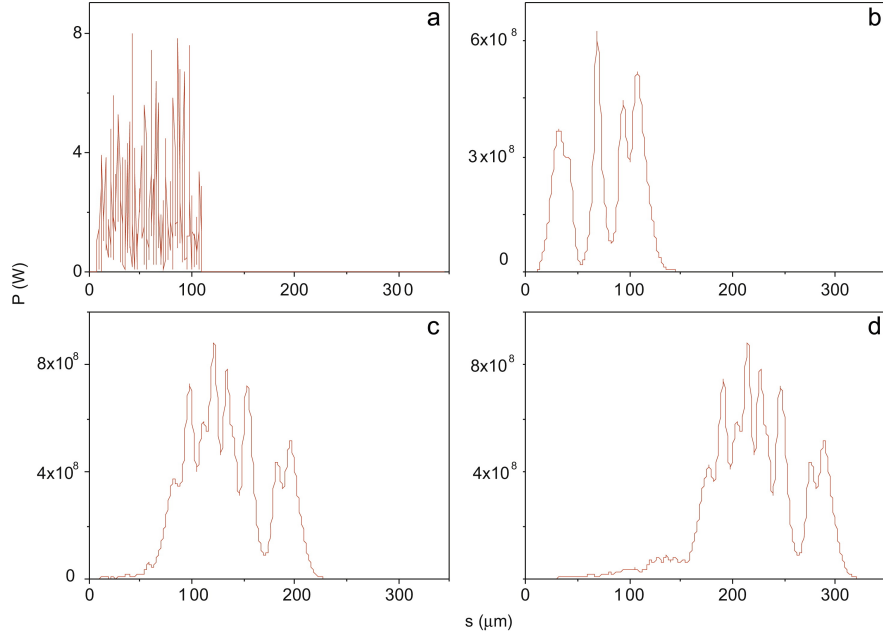


**Figure 3.4: Power profile evolution of a long electron bunch** - (a) Power[W] versus the coordinate along the bunch[ $\mu\text{m}$ ] at the beginning of the process, (b) at  $z=5$  m, (c) at  $z=10$  m and (d) at  $z=15$  m. Other data are:  $I=375$  A,  $L_B = 100\mu\text{m}$ ,  $\sigma_x = 50\mu\text{m}$ ,  $K=1.511$ ,  $\lambda_u=2.8$  cm,  $\lambda_r=474$  nm.



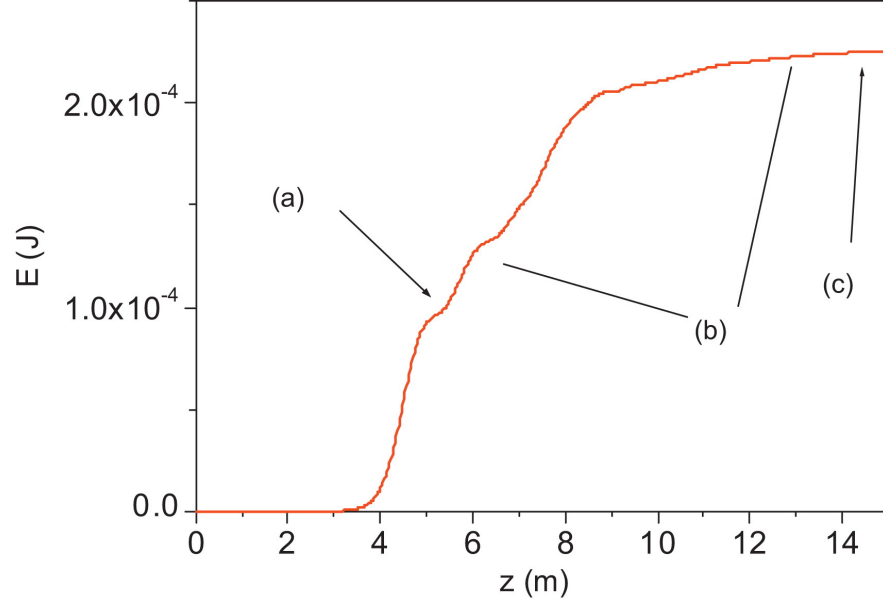


**Figure 3.5: Single Spike average energy growth along the undulator** - Average value of energy  $E(J)$  versus  $z$ , for the same values of Fig.3.4. Point (a): the power reaches the maximum value inside the bunch. Region (b): emission of secondary peaks. (c) Saturation of the energy.

As the bunch continues to radiate, even if it is much less intense, the average power increases further, but with a slower rate (region (b) in Fig.3.5). As the secondary radiation stops, the average power saturates (point (c) in Fig. 3.5). All these characteristics are in agreement with the provisions of the 1D model [19; 41]. A synthetic view of the power emission is given in Fig.3.6 where the normalized power level curves are presented in the  $(s, z)$  plane. The effective phase velocity differs from  $c$ , the speed of light. In addition, the solution of the dispersive equation  $\Lambda$  (Eq.2.46) depends on the deviation of the radiation frequency from the frequency that fulfills the synchronism condition in Eq.2.11. This dispersion reduces the group velocity below the speed of light and spikes advance less than one radiation wavelength per undulator period. Amplification stops at saturation and the 'dielectric' electron beam becomes nondispersive. After the cleaning up of the chaotic ensemble of spikes, characterizing the very early radiation, as seen also in Fig.3.4(a), the radiation organizes in few clean packets that propagate independently one from each other with a velocity given in the linear approximation

### 3. CHARGE SCALING LAW FOR SINGLE SPIKE OPERATION

---

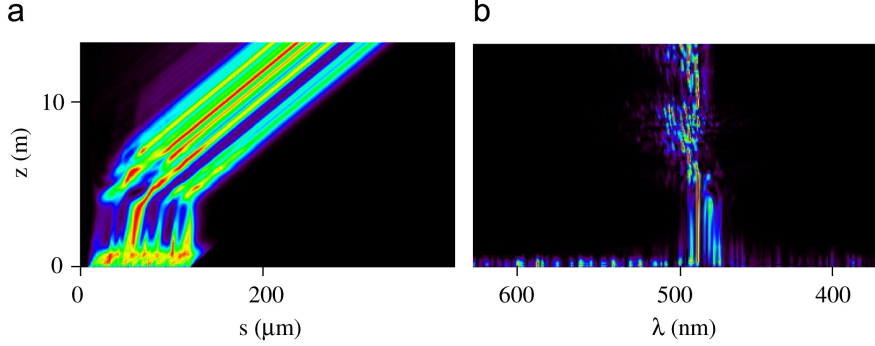


**Figure 3.6: Normalized level curves of the power and spectrum for long bunch simulation** - Level curves of the normalized power in the plane( $s, z$ ) and of the spectrum in the plane( $\lambda, z$ ) for the same values of Fig.3.4.

by

$$v_s = \frac{3v_{\parallel}}{2 + v_{\parallel}/c},$$

$v_s$  being the group velocity of the signal and  $v_{\parallel}$  the speed of the electrons in the  $z$  direction [41]. In few gain lengths, the peak saturates (point a in Fig.3.5).

At the same time, the first spike of radiation slips forward from the head of the beam. The spikes behind propagate over the beam with speed  $c$ , showing a change in the slope of the radiation patterns in the plane( $s, z$ ). The beam continues to produce a tail of secondary emission. An image of the spectrum in the plane( $\lambda, z$ ) is shown in Fig.3.6(b). The peak power  $P_{peak}$  in units of  $10^9 W$  has been recorded as function of the beam current  $I$  [A] with fixed beam length  $L_B$  in a bi-logarithmic graph presented in Fig.3.7. The red line (i) is the straight line with angular coefficient  $\log(P_{peak}/\log(I)^2)$ , corresponding to a dependence  $P_{peak} \sim I^2$ , while the blue one (ii) is the straight line corresponding to the dependence  $P_{peak} \sim I^{4/3}$ . As can be seen, the bottom curves(a) and (b), characterized by shorter bunch lengths((a)with  $15\mu m$  and (b)  $25\mu m$ ), fit better the first dependence, where as the upper curves (obtained with (c)  $50\mu m$  and (d)  $100\mu m$ ) respect the  $4/3$  dependence. The number of spikes given by the FEL simulations corresponds well to that indicated by the scaling law.

In Fig.3.7, different colours of the symbols refer to different number of spikes. In particular dark blue means one single spike, cyan two spikes, magenta three, red four, yellow five and green six or more. In the region of single spike occurrence, corresponding to the dark blue symbols, the peak power should be dependent only on the square power of

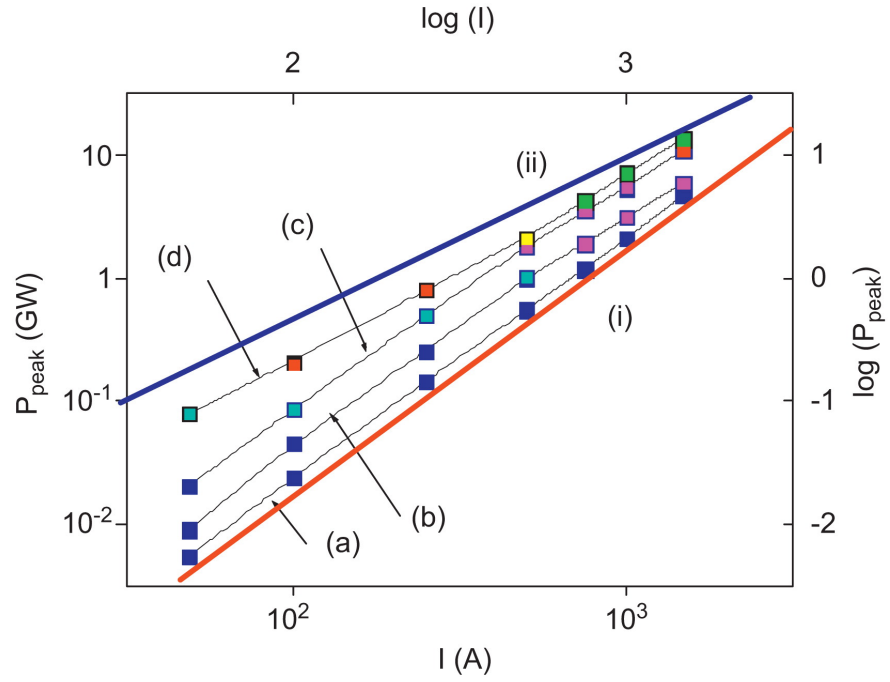


**Figure 3.7: Scaling of the peak power vs. the beam current** -  $L_b=15 \mu\text{m}$ , (b)  $L_b=25 \mu\text{m}$ , (c)  $L_b=50 \mu\text{m}$ , (d)  $L_b=100 \mu\text{m}$ , (i)  $\log(P) \approx 2\log(I)$ , (ii)  $\log(P) \approx 4/3 \log(I)$ . Dark blue means one single spike, cyan two spikes, magenta three, red four, yellow five and green six or more.

### 3. CHARGE SCALING LAW FOR SINGLE SPIKE OPERATION

---

the charge  $Q^2$ . Instead, as can be seen from Fig.3.7, the dependence on  $Q^2$  is confirmed for fixed  $L_B$ , but a further dependence on  $L_B$  comes out. Decreasing furthermore the dimension of the beam leads to go towards region outside the SVE-Approximation and where the gradients of the current profile play a role in the emission. The huge statistical fluctuations are also important at small beam length. A dependence on  $L_B$  is justified by the fact that the power stops the growth when the peaks slips out from the bunch. We can justify this result with a simple analogy: the radiation emitted by one slice scales as  $Q^2$  due to the fact that the process is super-radiant and adds to the power emitted by the next slices, giving a whole dependence by  $L_B Q^2$ . This simple model is valid as far as the effects of the current gradient do not become important. The points corresponding to the occurrence of multiple spikes are instead all fitted by straight lines with negative slopes, whose values passes from -1 to -4/3 from the bottom to the top of the figure.

#### 3.1.1 Single Spike start-to-end simulations at SPARC

In the previous part of this chapter, we have analysed the case of ideal beams, characterized by flat top current profile. This kind of beams is highly difficult to obtain in practice, in particular in the case of short bunches, that has to be compressed at large degree with velocity bunching. In this section, we want therefore to explore the possibility of producing single spike radiation with more realistic beams, based on start-to-end simulations from the photoinjector to the ending point of the undulator. Four different beams, generated and driven in the SPARC line [51] at 50 pC, have been analysed, characterized by different compression factors, and by different current profile. A description of velocity bunching and the experimental results at SPARC are described in the next chapter.

The longitudinal phase spaces ( $\Delta E/E$  versus  $z$ ) of all bunches(left axes), together with the current profile  $I$  (right axes), are presented in Fig.3.8 versus the coordinate  $z$  along the bunch. The main parameters of the beams are summarized in Table3.2. The simulations of the beams 1, 2 and 4 were done with the code PARMELA[52], while case 3 was simulated with ASTRA[53].

The first beam (beam 1, Table3.2 row 1 and Fig.3.8, window(1)) was compressed at  $\sigma_z = 45\mu\text{m}$  (the full width half maximum  $L_z^{FWHM}$  is  $110\mu\text{m}$ ), with a compression

### 3.1 Charge Scaling Law and Slippage Effect in Short Electron Bunch

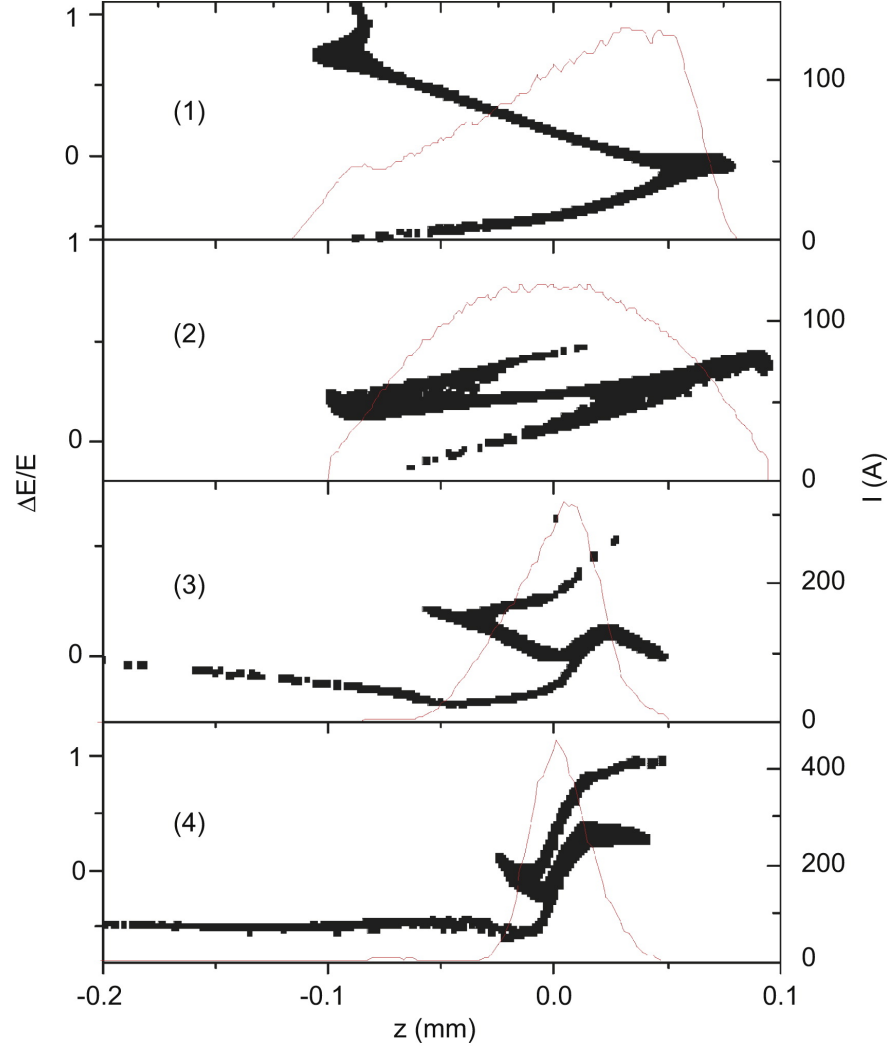


**Figure 3.8: Simulated electron longitudinal phase space: PARMELA output** - Left axis: phase space  $\Delta E/E$  in % versus  $z$  (mm). Right axis: current  $I[A]$  versus  $z$  (mm) for: (1)beam1, (2)beam2, (3)beam3 and (4)beam4

Beam	$\phi[degree]$	$\epsilon_n[\mu m]$	$\Delta E/E[\%]$	$\sigma_z[\mu m]$	$L_z^{FWHM}[\mu m]$	$I_P[A]$
1	-84.5	0.47	0.235	45	110	120
2	-95	0.45	0.069	45	142	120
3	-89.9	0.63	0.097	20	38	300
4	-91.4	2	0.21	22.8	32	430

**Table 3.2:** Main bunch properties

### 3. CHARGE SCALING LAW FOR SINGLE SPIKE OPERATION

---

factor of 6.66, achieving a peak current of 120A. In this operation, the control of the emittance is made by means of 12 magnetic coils around the first linac cavity. The current in all the coils is the same, the total magnetic field being constant along  $z$ . The second case analysed (beam2, Table3.2 row 2 and Fig.3.8), window (2) was obtained in the BLOW-OUT regime (See Chapter 6), with a laser pulse of 0.2 ps and an injection phase of  $-95^\circ$  in the over-compression condition. The final beam length  $\sigma_z$  is again  $45 \mu\text{m}$ ,  $L_z^{FWHM} = 142 \mu\text{m}$ , with peak current 120 A. The final energy spread is smaller respect to the standard operation case, and the current presents the typical parabolic shape of this regime. The last two beams (beam 3, Table3.2 row 3 and shown in Fig.3.8, window(3) and beam 4, Table3.2 row 4 and Fig.3.8, window (4)) have been injected in the first structure around the maximum compression phase (respectively,  $-89.9^\circ$  and  $-91.4^\circ$ ), obtaining currents characterized by strongly peaked profiles, with compression factors larger than 10. The difference between them is that beam 3 has been optimized with the genetic algorithm [54], leaving free the intensities of the 12 magnetic coils in the first structure and the injection phases in the last two structures (respectively,  $-34.9^\circ$  and  $-2.8^\circ$ ). These additional degrees of freedom have permitted to obtain a current very much larger than the first two cases and only a bit smaller than case 4, but with a much better control of emittance and energy spread, as can be seen in Table3.2. The third beam has a r.m.s. longitudinal dimension  $\sigma_z = 20 \mu\text{m}$ , with a FWHM value of  $38 \mu\text{m}$ , while the fourth beam presents  $\sigma_z = 22.8 \mu\text{m}$  for a FWHM value of  $32 \mu\text{m}$ . The slight increase in the r.m.s. value depends on the presence of the tail on the left that can be seen in Fig3.8(4). This last beam belongs to the high compression regime, explained in Ref.[49]. The four beams have been injected into the SPARC undulator. The undulator and lattice characteristics are: 6 undulator sections of 2.15 m,  $\lambda_u = 2.8 \text{ cm}$ ,  $K=1.51$ ,  $\text{dB/dz}=8 \text{ T/m}$ . Radiation with a wavelength of about 500 nm is produced. The matching at the undulator is done with the SPARC transfer line, constituted by two triplets. Various r.m.s. values of  $\sigma_x$  have been simulated trying to reach the single spike operation with maximum focalization and maximum energy extraction. In Table3.3 the most significant radiation characteristics are presented for the four beams simulated with some different r.m.s. values of  $\sigma_x$  at the entrance of the undulator. In particular, in the second column of the table we show the saturation length  $L_{sat}$ , defined as the position where the energy reaches  $1/e$  of the maximum value

### 3.1 Charge Scaling Law and Slippage Effect in Short Electron Bunch

$\langle E_{max} \rangle$  attained along the undulator, plus one gain length evaluated numerically

$$L_{sat} = L \left( \frac{\langle E \rangle_{max}}{e} \right) + L_g \quad (3.10)$$

Beam	$\sigma_x[\mu m]$	$L_{sat}[m]$	M	$P_{max}[GW]$	$E_{PEAK}[\mu J]$	$i_{div}[\text{mrad}]$	$\langle \sigma_{rad} \rangle[\text{mm}]$	$L_z^{FWHM}[\mu m]$	$b_w[\%]$
1	100	9.88	1-2	0.13	20	0.52	0.63	22	1
	50	9.23	4-5	0.095	30	0.805	1	15 $^\alpha$	1
2	104	9.94	1-2	0.037	9.7	0.49	0.53	30	0.8
	50	9.22	2-3	0.09	30	0.53	0.53	121.5	1
3	104	7.45	1	0.16	17.7	0.658	0.494	16.5	1
	79	6.5	1-2	0.42	47.3	0.652	0.45	17.7	1
	50	7	2	0.35	55.2	0.52	0.43	16.3 $^\alpha$	0.8
4	125	7.28	1	0.41	35.2	0.7	0.5	13	1.5
	100	4.3	1	0.7	67	0.78	0.26	11	1.2
	70	4.3	1	0.75	66.8	0.87	0.33	19	1.3

**Table 3.3:** Table with the principal results.  $\alpha$ : Cases where the secondary peaks are lower than half maximum value,  $b_w$  is the normalized bandwidth

Furthermore we have listed the number of spikes  $M$  at saturation as given by the simulation, the maximum value of the power  $P_{max}$  along the undulator, the maximum energy  $\langle E_{max} \rangle$  along the undulator, the divergence  $\theta$  and the transverse size of the radiation pulse at saturation averaged on the radiation pulse,

$$\langle \theta \rangle = \frac{\int ds P(L_{sat} div(L_{sat}))}{\int ds P_{sat}} \quad (3.11)$$

$$\langle \sigma_{rad} \rangle = \frac{\int ds P(L_{sat} \sigma_{rad}(L_{sat}))}{\int ds P_{sat}} \quad (3.12)$$

the longitudinal FWHM dimension of the radiation  $L_z^{FWHM}$ , and the bandwidth at saturation. The values marked with  $\alpha$  in the longitudinal FWHM dimension column refer to cases where the secondary peaks are lower than the half maximum value, so the longitudinal dimension is under estimated. In Fig.3.9, the growth of the peak power  $P$ (left axis) and of the average value of the energy  $\langle E \rangle$ (right axis) of the radiation is shown versus  $z$ , in one particularly favourable case for each beam. The green lines indicate the saturation coordinate. In Fig.3.10, the shape of the radiation at saturation and the current are plotted. In case(1), the beam exits from the linac at 12m with a r.m.s. value of  $\sigma_x = 126\mu m$  and has been transversally matched to the undulator entrance by means of the transfer line, reaching the r.m.s. value  $\sigma_x = 100\mu m$ . A

### 3. CHARGE SCALING LAW FOR SINGLE SPIKE OPERATION

---

stronger focussing at  $\sigma_x = 50\mu\text{m}$  produces a larger energy, but the pulse profile is less clean. For the  $\sigma_x = 1200\mu\text{m}$  case, shown in Fig.3.9(1) and Fig.3.9(1), the saturation of the power coincides with the exit of the pulse peak from the bunch. After this exit, the radiation propagates behind the beam with velocity equal  $c$ . The radiation process does not saturate until the end of the undulator, due to the formation on the beam of low secondary peaks of emission. The energy continues to increase due to these secondary maxima. The profile of the beam and the spectrum gets worse. The average gain length estimated by the simulation is  $L_g=0.64$  m, while the Ming-Xie evaluation gives  $L_g=0.66$  m. The second beam exits from the linac with  $\sigma_x = 104\mu\text{m}$ . The beam emits a peak power lower by a factor 3 respect to the first one. The saturation of the peak occurs at 10 m, but the energy continues to increase more slowly till the end of the undulator. The gain length estimated by the numerical simulation is  $L_g=0.56$  m, while the theoretical value is 0.38 m. This beam is particularly suitable for testing the single spike scaling law because the profile of current, differently from beam 1, is very regular and follow the law  $I = I_0(1 - \alpha(s - s_0)^2/I_0)$ , with  $I_0=120$  A,  $s_0 = 100\mu\text{m}$  and  $\alpha=0.01065$  A/ $\mu\text{m}^2$ . The shape of the current permits to write a simple relation between the total charge and the peak current  $I_0 = cQ/L_B$  with  $L_B = 2s_0(1 - \alpha(s - s_0)^2/I_0)$ . In this case  $L_B$  turns out to be  $L_B = 136.6\mu\text{m}$ . To check the single spike scaling law, we have varied the value of  $\sigma_x$ , matching the beam to the undulator with different values of  $\beta$ , by means of the transfer line. As the values of  $\sigma_x$  and  $\sigma_y$  vary along the undulator, we have plotted the number of spikes versus the value of  $\langle \sigma_r \rangle = \sqrt{\sigma_x^2 + \sigma_y^2}$  averaged along all the undulator line. The number  $M$  of spikes has been calculated by 3.8 using the average emittance and energy spread of the beam and with the value  $L_B$  defined above. This value of  $M$  has been plotted in Fig.3.11(beam(2))(solid line), while the number of spikes evaluated by the numerical evidence is marked by pink stars. Deviation from integer accounts for situations where one of the spikes is not completely developed, the error bars take into account of the uncertainty in the visual determination of the number of spikes. The agreement between the numerical and the foreseen result is good. Beam 3 exits from the linac at 12 m with  $\sigma_x = 79\mu\text{m}$ . The case presented in Fig.3.9(3) and Fig.3.10(3)is relevant to the value  $\sigma_x = 104\mu\text{m}$ . The production of secondary peaks is, in this case, almost inexistent. The gain length obtained analysing the simulations is 0.42 m, the estimate by the M.Xie formulas is 0.28 m. In this case, the current has a peaked shape that can be assimilated to a



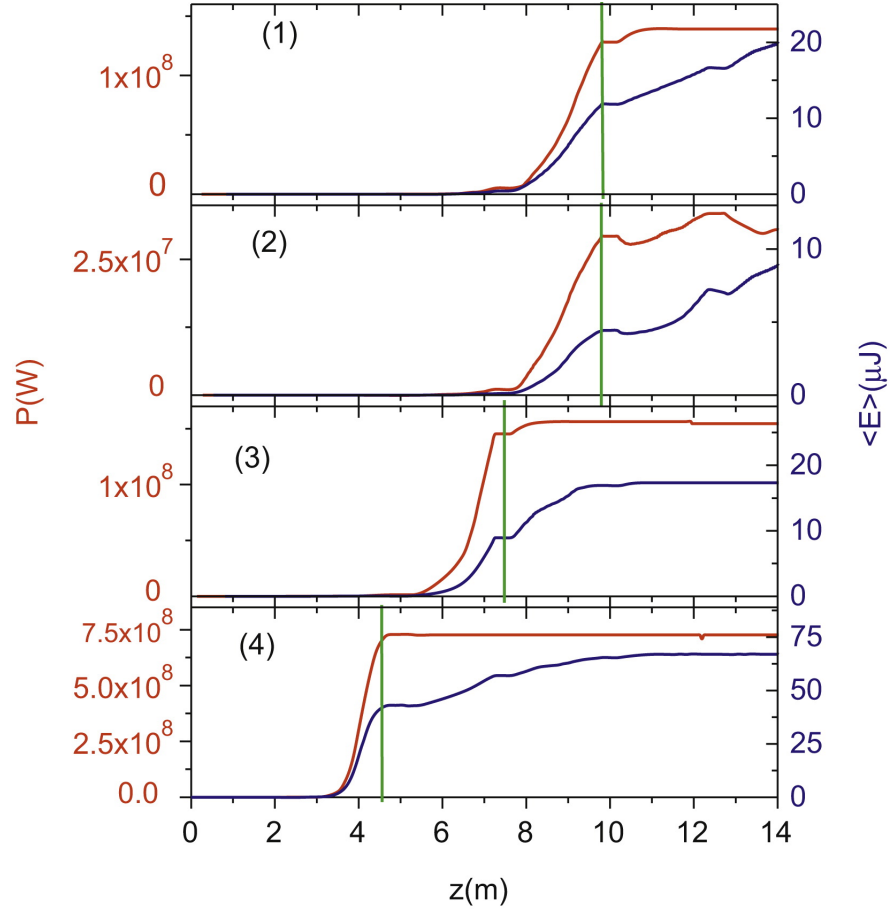


**Figure 3.9: Power and energy evolution along  $z$  for 4 different electron bunches**  
 - Growth of the peak power  $P_{peak}[\text{W}]$  (red curve, left axis) and energy  $\langle E \rangle [\mu\text{J}]$  (blue curve, right axis) versus  $z[\text{m}]$  for: window(1) : beam 1,  $\sigma_x = 100\mu\text{m}$ . Window (2): beam 2,  $\sigma_x = 104\mu\text{m}$ . Window(3): beam 3,  $\sigma_x = 100\mu\text{m}$ . Window(4): beam 4,  $\sigma_x = 125\mu\text{m}$ . The green lines indicates the saturation of the peak

### 3. CHARGE SCALING LAW FOR SINGLE SPIKE OPERATION

---

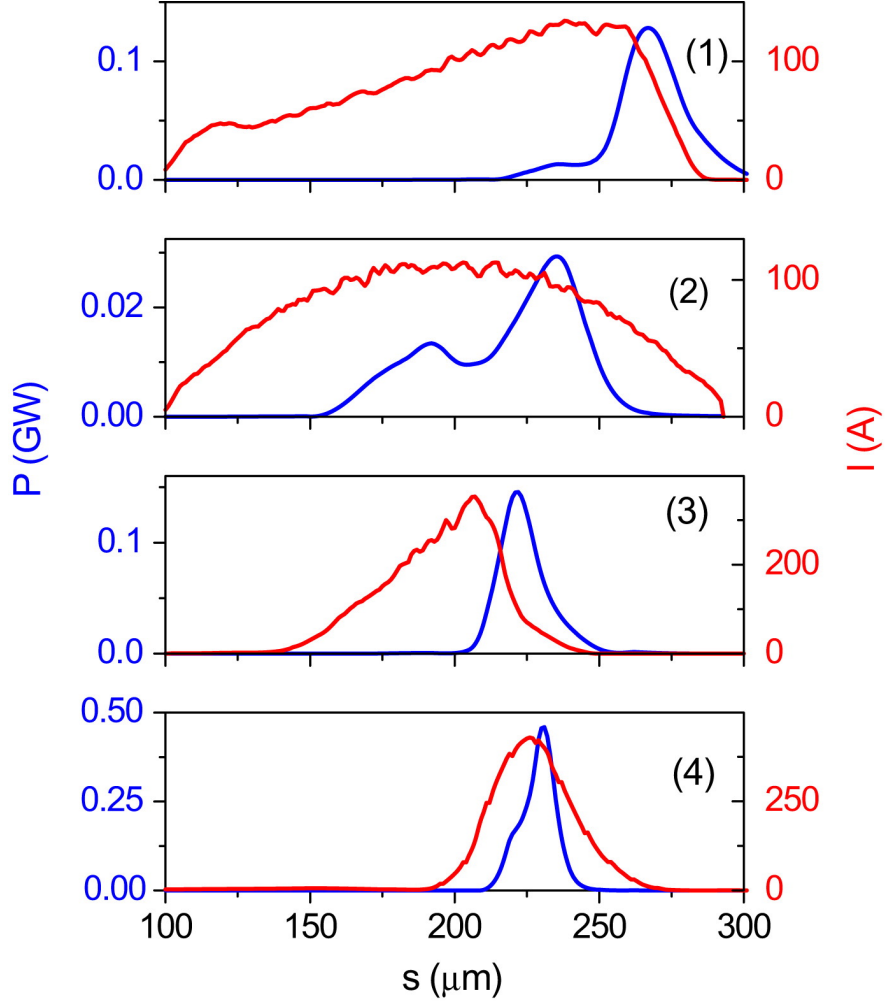


**Figure 3.10: Power profile for 4 different electron bunches** - Shape of the power  $P$ [GW] (blue curve, left axis) and current  $I$  (A) (red curve, right axis) versus  $s$  ( $\mu\text{m}$ ) for: window(1): beam 1,  $\sigma_x = 100\mu\text{m}$ . Window (2): beam 2,  $\sigma_x = 104\mu\text{m}$ . Window(3): beam 3,  $\sigma_x = 100\mu\text{m}$ . Window(4): beam 4,  $\sigma_x = 125\mu\text{m}$ .

### 3.1 Charge Scaling Law and Slippage Effect in Short Electron Bunch

---

Gaussian one. The relation  $L_B = (2\pi)^{1/2}\sigma_z$  has been used to evaluate the length of the beam. In Fig.3.11(beam(3)), an analysis similar to that done previously for beam 2 is presented. Also in this case, the results obtained by using the scaling law with the average values of emittance and energy spread are in good agreement with the numerical evidences. Beam 4 exits from the linac with  $\sigma_x = 208\mu\text{m}$ , a value too large for producing a considerable amount of energy, therefore it has to be matched. The transverse dimension used for the simulation presented in Fig.3.6(4) and Fig.3.5(4) is  $\sigma_x = 100\mu\text{m}$ . Also in this case, the saturation occurs in two stages: during the exponential growth, the radiation propagates slowly on the beam, slipping toward the leading edge of the bunch. When the peak exits from the beam, secondary peaks are generated. The total energy continues to increase, but more slowly. The gain length from the simulation is 0.21m, the estimated one being 0.33m. The total energy yield is 67  $\mu\text{J}$ . The divergence of the pulse is 0.799 mrad, the normalized bandwidth 0.012, the FWHM pulse duration 11  $\mu\text{m}$ , corresponding to 37 fs. The analysis in terms of the scaling law is given in Fig.3.11(beam(4)), showing a good agreement. The whole analysis shows that there is large margin of choice in single spike operation. As can be seen by the data in Table 3.3, situations characterized by a single spiked power profile can be obtained with every beam. However, the energy extracted is larger in cases 3 and 4 respect to 1 and 2. The difference that makes bunch 3 and 4 more efficient respect to the other two is that the peak current value is larger by a factor 34 respect to the first two ones. The reduction in the FEL efficiency due to larger values in emittance and energy spread is balanced by the increase due to the current peak value. The maximum compression regime leads to minima pulse lengths, large peak power and total energy. However, the operation in this regime requires a tight control of the beam line elements(as for instance the magnetic field intensity in the coils of the first structure) and of the injection phases for avoiding the formation of tails that degrade the beam quality and for controlling emittance and energy spread. Beam emittance and energy spread are not demanding for the single spike occurrence, as regards the aspect of shape and width of radiation and spectrum; on the contrary, they are fundamental to determine the power and the energy yield. As regards the comparison between the simulation results with the Ming Xie predictions, the difference between them is particularly significant when the beam is rather irregular and has tails on the edges or halos. In these cases the average values are substantially different from the slices

### 3. CHARGE SCALING LAW FOR SINGLE SPIKE OPERATION

---

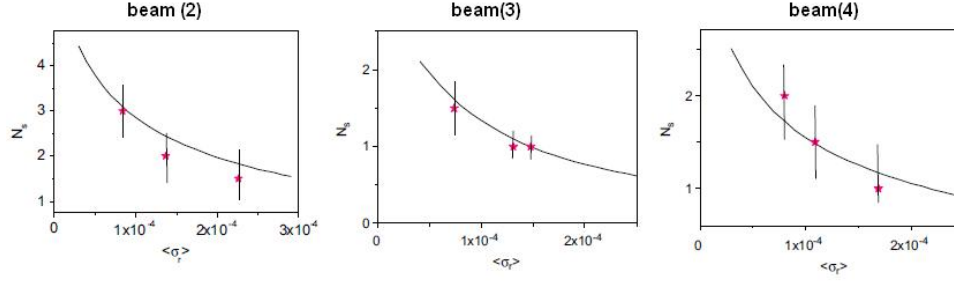


**Figure 3.11: Scaling results of the 3D-number of spikes  $M$  - Number spike in the case of beam 2,3,4 versus the average transverse dimension of the beam  $\langle \sigma_r \rangle$ : solid line: result given by 3D equation of single spike number 3.8 . Pinkstars: numerical evidence.**

ones, so simulations and analytical formulas give different results and the comparison is difficult to manage.

## 4

# Layout of the Free Electron Laser (FEL) SPARC

In this chapter a brief description of the SPARC machine and diagnostic devices is given.

## 4.1 SPARC Layout

The SPARC FEL is composed by a high brightness photo-injector providing a high-quality beam at energies up to 150 and 200 MeV (12 m), a transfer line for beam matching and diagnostic (6.8 m) and an undulator beam line (15 m) composed by six undulator sections with variable gap (See Fig.4.1). The laser system that has been chosen to drive the high brilliance photoinjector, is based upon the active medium Ti:Sapphire (Ti:Sa) laser (Ti :  $Al_2O_3$ ) technology which is suitable for the generation of broadband ( $\sim 10$ nm and even more) laser pulses, extremely important for the generation of short pulses. In Fig.4.2 the laser layout is shown. It consists of Ti:Sa laser oscillator pumped by diode laser and amplified with CPA technique in a regenerative and a multipass amplifiers pumped by Nd-Yag laser and another diode laser. The laser system is capable of producing pulses from few tenth of fs to ps scale. The oscillator is set to work in a mode locking regime at 800 nm, with 100 fs transform-limited pulses and therefore a bandwidth of about 10 nm. The oscillator imposes the temporal frequency of the system and thus it is the component of the laser system to synchronize with the accelerating field in the photo-injector at a stable RF phase. The problem

#### 4. LAYOUT OF THE FREE ELECTRON LASER (FEL) SPARC

---

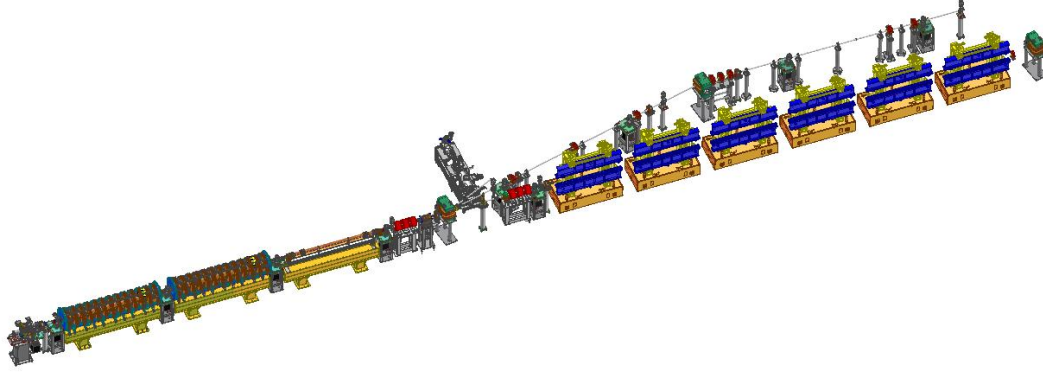


**Figure 4.1: SPARC layout** - The figure shows the photo-injector composed by a gun and three accelerating cavities, the transfer line and the six undulator sections, it's also shown on the side of beamline the system for harmonic generation in gas.

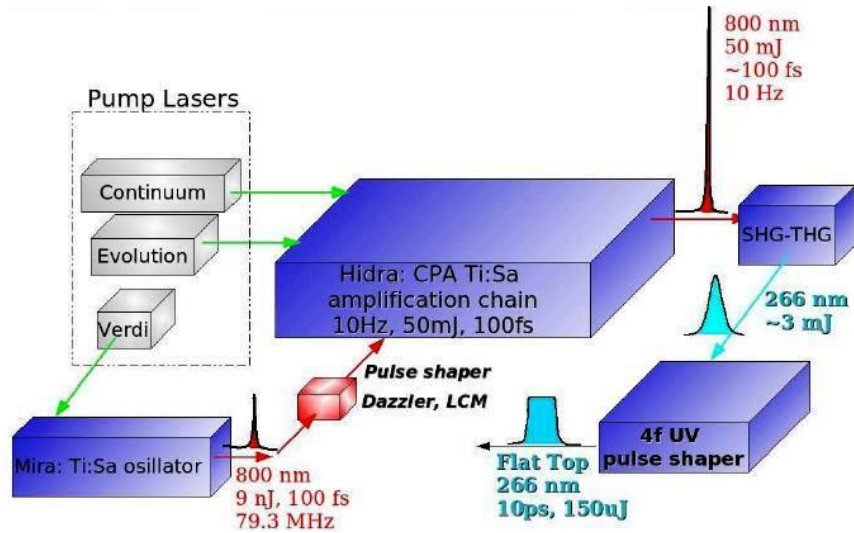


**Figure 4.2: SPARC laser system layout** - Ti:Sa laser oscillator pumped by diode laser and amplified with CPA technique

of keeping laser systems, RF systems and accelerator diagnostics extremely well synchronized is a crucial issue for the successful operation of the various FEL radiation sources presently operating and in construction or design phase [55]. Details on the architecture of the SPARC synchronization system and on the hardware used for this task are described in Ref.[56].

The gun is a SLAC/BNL/UCLA 1.6 cell S-band RF photo-injector (See Fig.4.3), the electron bunches are generated, via photoelectric effect, by the laser pulse on a copper photo-cathode. The RF wave in the gun cavities accelerates the beam at 5 MeV and a focusing is provided by a magnetic solenoid surrounding the gun. During these processes the electron beam emittance and the energy spread, due to the combined action of the space charge and RF accelerating field effects, must be minimized.

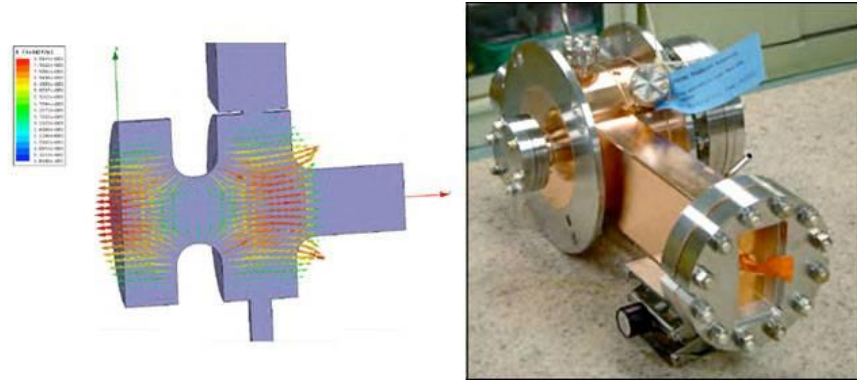


**Figure 4.3: GUN Photo-cathode cartoon** - Electron Beam-Laser interaction near the cathode in high brightness photo-injection

In fact the emittance grow into the r.f. gun is due to the defocusing generated by the powerful space charge strength in the close proximity of the cathode where the electron beam is not relativistic yet. The performances of the gun have been studied in a first phase of commissioning during 2006-07, with a movable emittance meter. This instrument allowed the investigation of the beam parameters dynamic in the first meters after the gun, allowing to optimize the working point in order to minimize the emittance (Ferrario working point) [4].

The final energy is reached with three SLAC-type linac sections at 2.856 GHz. The first two sections are surrounded by solenoids providing additional focusing during acceleration (See Fig.4.4). This solution allows to work in velocity bunching regime that

#### 4. LAYOUT OF THE FREE ELECTRON LASER (FEL) SPARC

---

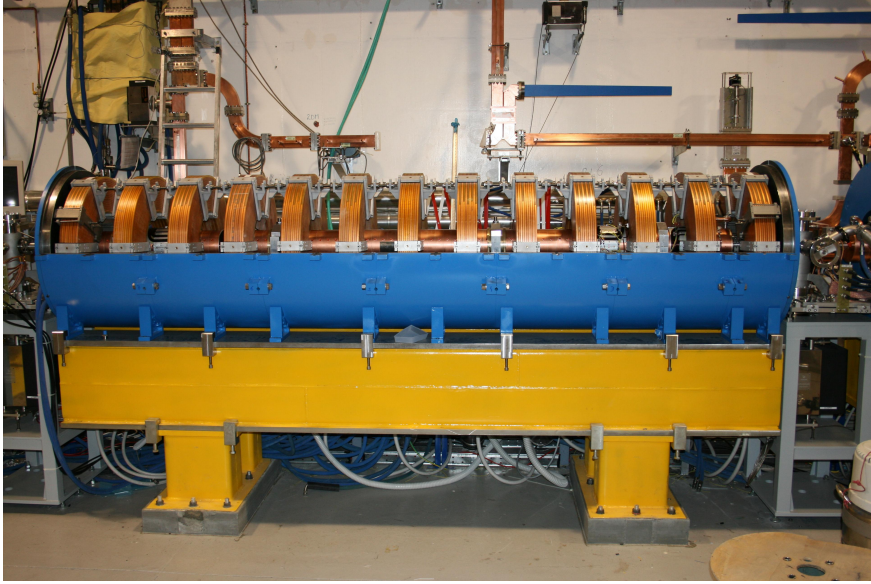


**Figure 4.4: S-band SLAC-type accelerating section -**

consists in exploiting a correlated velocity dispersion of the electron beam for longitudinal compression during the acceleration. The magnetic axial field properly tuned ensures the desired emittance preservation, i.e. high brightness electron source with short bunch length without the implementation of a magnetic chicane. The electrons longitudinal distribution is correlated to the laser pulse shape on the cathode, there are two main way actually used at SPARC to produce the electron beam. The first consists in a 7-10 ps UV pulse with gaussian or flat-top time profile generated by nonlinear interaction in a crystal by the IR Ti:Sa laser pulse. The electron beam generated has the same profile of the laser pulse, very low emittance and energy spread and about 1 nC of charge. The second is called BLOW-OUT regime (See Chapter 5) and consists in a short UV laser pulse ( $\sim 200$  fs), the beam produced have less charge 10-400 pC and the beam length is few ps. The velocity bunching technique is used for the beam compression, i.e. shorter beam length with higher peak current, for SASE-SEED experiments. So the SPARC photo-injector is able to control the key parameter of the Single Spike regime: bunch charge, length and current.

The beam transport is obtained with a FODO lattice where quadrupoles in the undulator intersections provides the horizontal focusing and the undulator field provide the vertical focusing. In this condition the matching Twiss parameter depends on the



resonant frequency which sets the undulator field strength. A RF deflector cavity installed on the transfer line before the magnetic spectrometer allows the measure of the beam parameters as a function of the longitudinal coordinate [57](See Fig.4.5). The

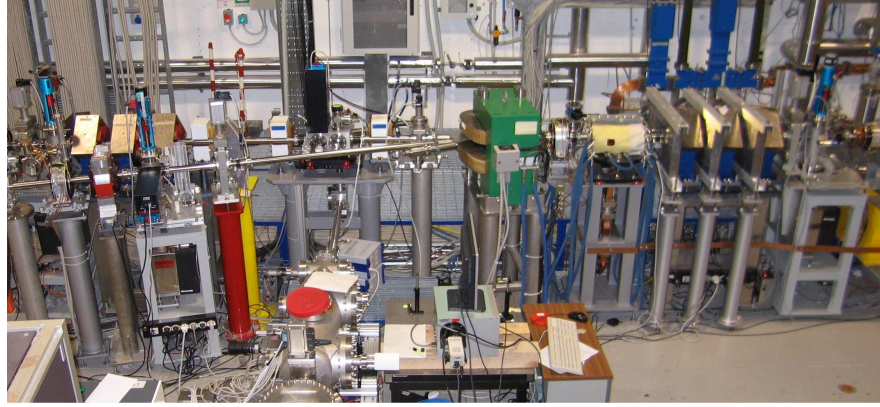


**Figure 4.5: Magnetic elements of transfer line** - The magnetic elements are used for e-beam diagnostic and matching to the undulator beamline

analysis of the images acquired with the combined use of the deflector cavity and the spectrometer magnet allows the determination of mean energy, energy spread (slice and projected), energy chirp, bunch length and, knowing the bunch charge, measured independently, the longitudinal profile of the bunch current. The experimental beam parameters for max-compressed and uncompressed beam cases are listed in Tab.4.1, obviously all the intermediate compression can be achieved.

Parameter	Max-Compressed	Uncompressed
Energy [MeV]	$\sim 110$	$\sim 180$
Energy Spread [%]	0.1	0.03
Energy Chirp [%]	2	0
Norm. Emittance [mm-mrad]	2-4	1-2
Transv.RMS [ $\mu\text{m}$ ]	100-300	100-300
Beam length [ps]	0.2-1	2-8
Beam Charge [pC]	10-400	1000
Beam Current [A]	100-1000	30-100

**Table 4.1: Electron beam parameters** The star case (\*) refers to to blow-out regime for the lower value (gaussian beam) and the higher value for the normal operation with gaussian or flat top beam

## 4. LAYOUT OF THE FREE ELECTRON LASER (FEL) SPARC

---

### 4.1.1 SPARC undulator system and FEL laser diagnostic

The SPARC undulators are six variable gap sections of 75 periods each, with a period length of 2.8 cm and a maximum normalized undulator amplitude:  $K=2.2$ . Magnetic maps and  $K$  vs. undulator gap were measured before the undulator installation on beamline with a Hall probe mounted on a translation stage (See Fig.4.6). These values were cross checked with the spontaneous emission spectra measured with a test electron beam, showing a good agreement[58]. If  $K$  is smaller than 1, the emitted



**Figure 4.6:** Undulator picture - 2.156 m PPM Halbach configuration undulator section

radiation is contained within the synchrotron radiation cone, and the emission is predominantly in a single line. If  $K$  is larger than 1, the synchrotron radiation cone sweeps an angle larger than the synchrotron radiation opening angle. In this case, the spectrum is rich in harmonics and approaches the synchrotron radiation spectrum when  $K$  is very large. When  $K \geq 1$ , the magnet is usually referred to as a wiggler, reserving the name undulator for the case  $K$  less than or on the order of one. The main component of the seed laser system is a regenerative amplifier (LEGEND HFE by Coherent), seeded by

the same oscillator driving the photocathode amplifier. It delivers 2.5 mJ at 800 nm with a pulse duration shorter than 120 fs. The laser is focused by a 2 m focal length lens to an in vacuum cell, where a valve synchronized to the 10 Hz timing system of SPARC injects gas. In Fig.4.7, the gas interaction chamber, developed at CEA and installed to inject radiation in the transfer line between the linac and the undulator beamline, is shown.

An in-vacuum optical system is used to match the transverse optical mode of the har-

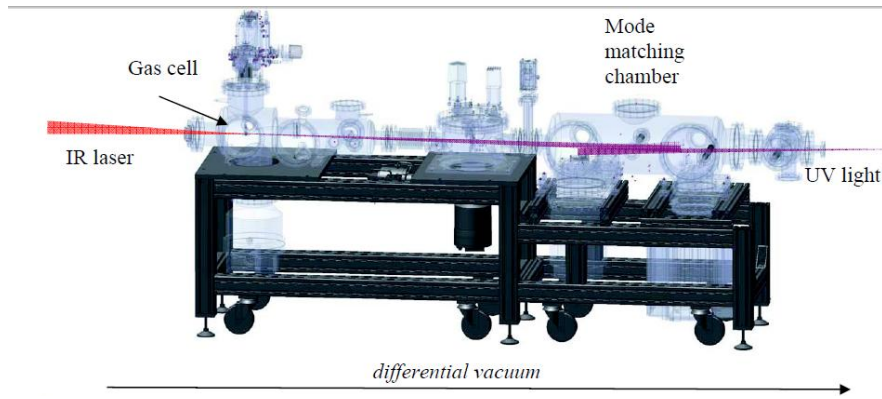


**Figure 4.7: Harmonic generation chamber realized at CEA** - The laser enters from the left side and is optically matched to the undulator by two spherical mirrors located in the chamber on the right. The differential pumping ensures vacuum at  $10^{-7}$  mbar in the electron beamline.

monic to that of the e-beam in the first undulator section [59]. The UV pulse is injected into the SPARC undulator by means of a periscope and a magnetic chicane deflecting the e-beam from the straight path (see Fig.4.8). High-order odd harmonics of the Ti:Sa laser may be generated at the wavelengths 266nm, 160nm, and 114nm.

The FEL radiation is analyzed by a spectrometer, a Joulemeter and a **F**requency **R**esolved **O**ptical **G**ating **F**ROG for temporal profile diagnostic. The in vacuum spectrometer designed and built by the LUXOR laboratory in Padova is the main radiation diagnostic. The spectrometer gratings and the CCD detector have been calibrated in efficiency and it allows the simultaneous determination of spectral properties of the observed radiation and of the pulse energy[12](See Fig.4.9). The FROG technique involves using a nonlinear optical process to obtain an autocorrelation signal, which is then spectrally resolved to yield a FROG trace, that is a two-dimensional plot of the signal spectrum vs. time delay. The FROG technique implemented at SPARC is

#### 4. LAYOUT OF THE FREE ELECTRON LASER (FEL) SPARC

---

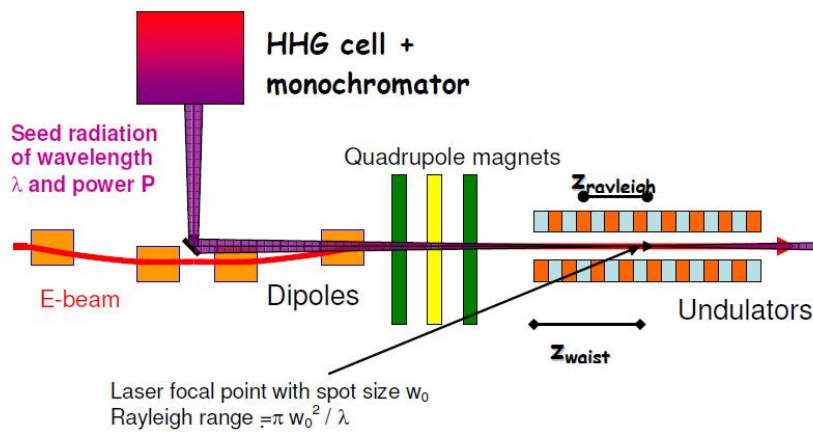


Figure 4.8: Seed and harmonics pulses generated in gas injection scheme -

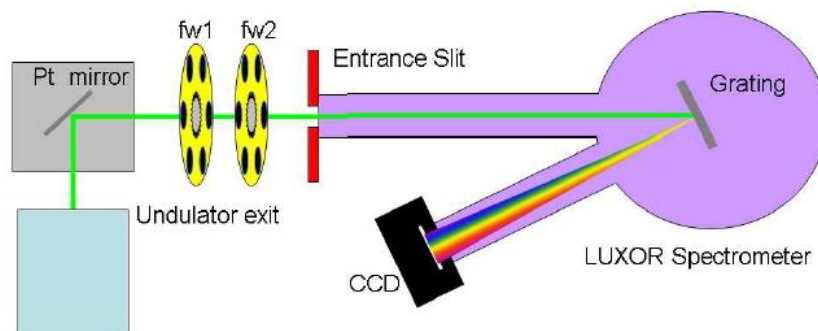
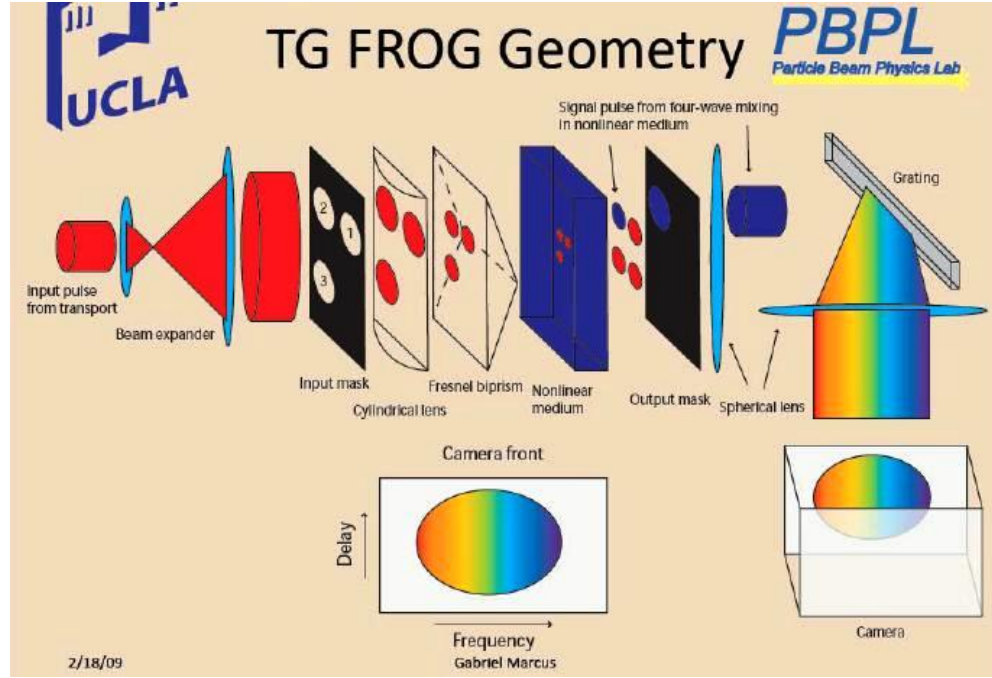


Figure 4.9: Spectrometer - The in vacuum spectrometer allow the determination of the spectral properties and energy of FEL radiation

developed in collaboration with G.Marcus from UCLA [60], it operates on a single shot basis. A cartoon of the optical elements configuration adopted at SPARC is shown in Fig.4.10. During summer 2010 the FROG system has been installed and the first preliminary tests with seed have been done.



**Figure 4.10: Frequency resolved optical gating** - Scheme of the diagnostic of short laser pulse at SPARC.credit figure[60]

#### **4. LAYOUT OF THE FREE ELECTRON LASER (FEL) SPARC**

---

## 5

# Production of Short Electron Bunches

In this chapter we introduce the technique for the short beam generation on cathode, the so called BLOW-OUT regime, and the beam compression schemes: Velocity Bunching (VB) and magnetic chicane. These compression techniques are fundamental to achieve the conditions for the single spike regime, but at the same time they introduce a beam degradation which has to be taken into account in order to have a FEL amplification. The experimental results of the VB technique with emittance compensation, used at SPARC, are shown in Ref.[10]. The characterization of the beams used in summer 2010 to obtain the SASE single spike regime and the superradiant seed pulses is also presented.

### 5.1 Electron Bunch from BLOW-OUT Regime

State-of-the-art high brightness electron source are based on use of a high gradient RF photoinjector, driven by a approximately uniformly filled, temporally flat, cylindrical distributions laser pulses in order to minimize the space-charge induced emittance growth[4]. Obtaining such laser pulse shapes introduces a high degree of complexity in the photocathode drive laser, and beam distribution presents large nonlinearities in the space charge field profiles at the beam longitudinal head and tail. These nonlinearities eventually give rise to irreversible emittance growth. The ideal beam distribution requires that the space-charge fields in each Cartesian dimension have linear dependence on the bunch coordinates. Such a condition is achieved for uniformly filled ellipsoidal distributions. One possibility for obtaining the uniform ellipsoidal density distribution is to similarly shape the laser pulse illuminating the cathode[61]; however, this solution further increases the complexity of the laser system. Another attractive option takes advantage of the ultrafast rearrangement of the beam as it expands longitudinally under the influence of strong space-charge forces. Luiten et al. [62], reconsidering an idea proposed by Serafini [63], have shown that to obtain a final ellipsoidal distribution there is essentially no requirement on the initial laser pulse shape other than it be much shorter than the final bunch length after expansion. This mode of operation, where the optimized distribution is obtained by dynamical evolution from an initial ultrashort beam, has been termed the BLOW-OUT regime of photoinjector operation, to emphasize the strong longitudinal space-charge expansion. The experimental demonstration has been obtained at UCLA [64] by illuminating the cathode in a rf photogun with an ultrashort laser pulse with an appropriate transverse profile. At SPARC the initial project developed a laser system to obtain an uniformly filled, temporally flat, cylindrical distributions of the e-beam to study the emittance growth and compensation in the linac respect to the gaussian shape e-beam. The e-bunch length, as long as the UV laser pulse illuminating the cathode, is about 8 ps. So to obtain a very short e-beam (fs scale) a strong compression is needed. The use of BLOW-OUT regime allows to reach a shorter beam length directly on the cathode.

At SPARC the ultra-short laser pulse used for BLOW-OUT regime is a gaussian pulse with 150 fs RMS length. The expansion due to the space charge combined with the RF accelerating field creates a ellipsoidal e-beam with a rms length of about 2 ps.



## 5.1 Electron Bunch from BLOW-OUT Regime

Fig.5.1 shows the longitudinal phase space and the parameters measured by means of

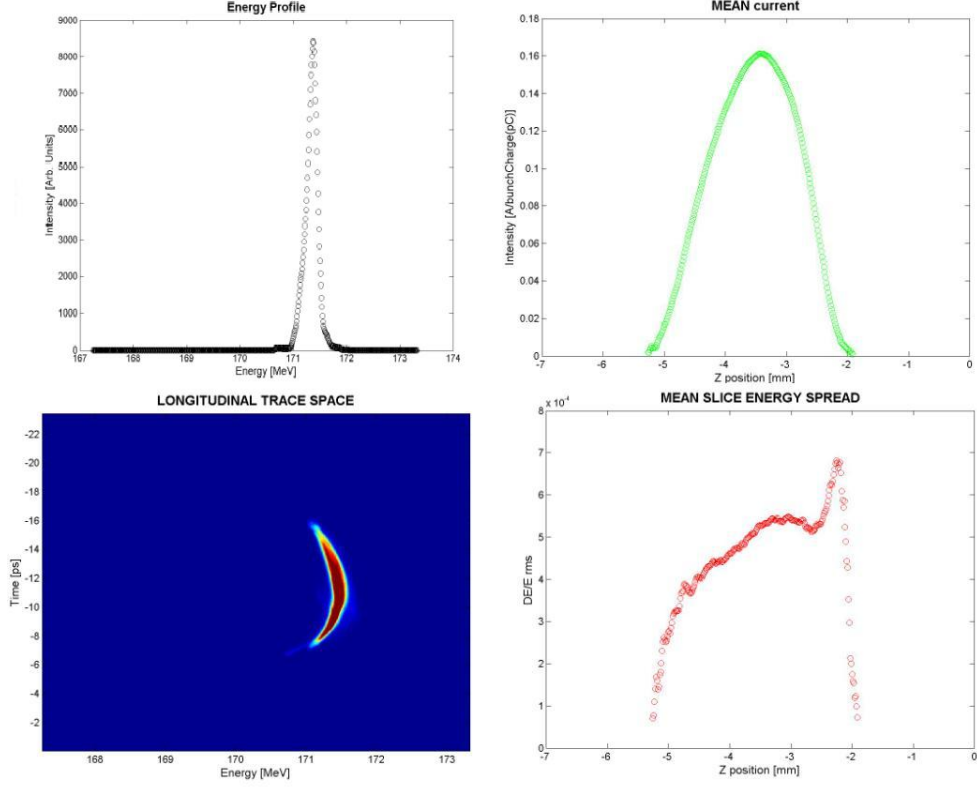


**Figure 5.1: Main BLOW-OUT beam measurement at the end of the linac without VB compression** - Pictures of the electron beam longitudinal phase space and related parameters measured by means of dipole and the RF deflector

dipole and the RF deflector. The beam parameters are almost constant along the beam while the figure at left on bottom shows the longitudinal phase space ( $E, t$ ) where is evident the curvature due to the RF accelerating wave. The emittance measures are made with the quadrupole scan technique, the results depends by the solenoids around the gun and the first two cavities; combined with the RF deflector is possible to measure the emittance slice.

### 5.2 Bunch Compression: Magnetic Chicane vs Velocity Bunching (VB)

To obtain the high peak current, electron bunches must be compressed longitudinally. As shown above, space charge effects at low energy prevent the generation of short electron bunches ( $<1$  ps) with a significant amount of charge ( $>10$  pC) directly from the electron source, leading to emittance degradation and bunch elongation within a few centimeters downstream the cathode. As such, bunch compression is always necessary to shorten the electron pulse to the required length thus achieving a high peak current. The most popular device used thus far is the magnetic compressor in which a bunch with a time-energy correlation (or chirp) is driven along an energy-dependent path length by a dispersive, nonisochronous beam transport section, consisting, in its simplest form, of four dipoles placed in a chicane configuration. Radiation is emitted when electrons bend in the magnetic fields of the chicane; the radiation is coherent for wavelengths longer than the bunch length. The coherent radiation is beneficial, in that it can be used as a longitudinal bunch diagnostic or as a dedicated terahertz radiation source. But the radiation is also destructive: the emission of coherent radiation by the beam leads to self-interactions which distort the longitudinal phase space, which can limit compression and cause an increase in the transverse emittance [65]. The layout of a magnetic chicane and the evolution of the phase space are shown in Fig.5.2. Longitudinal bunch compression is achieved in two steps. First an energy slope is imprinted on the bunch by acceleration on the falling slope of the RF wave. Consequently the particles at the head of the bunch receive a smaller energy gain than those at the tail. Afterwards the particles pass through a magnetic chicane where the trailing electrons of larger energy travel a shorter distance than the leading ones of smaller energy and thus are enabled to catch up. To realize the energy slope, the RF phase in the first accelerator module is adjusted in such a way that the particles are accelerated on the slope of the RF wave. Due to the cosine shape of the RF wave, adding a nonlinear term to the position energy relationship inside the bunch, and due to coherent synchrotron radiation effects in the magnetic chicanes, the final bunches do not possess the ideal narrow shape but consist of a leading spike and a long tail.

The velocity bunching technique is able to compress the bunch using rectilinear trajectories at relatively low energy, which must thus be integrated into the emittance

## 5.2 Bunch Compression: Magnetic Chicane vs Velocity Bunching (VB)

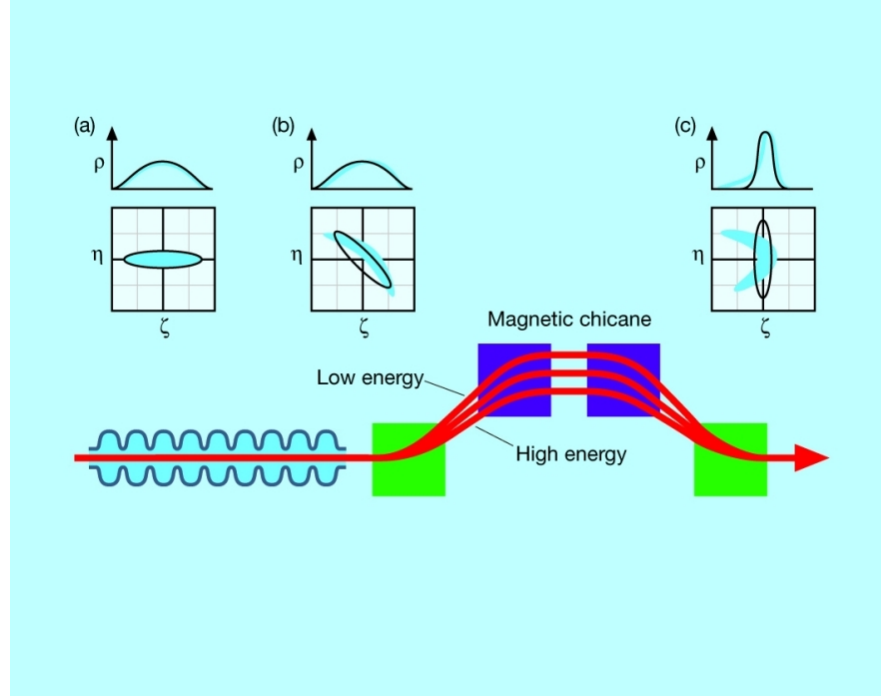


**Figure 5.2: Principle of longitudinal electron bunch compression in magnetic chicane** - (credit figure) The bottom row shows an accelerating cavity and the four dipole magnets of the magnetic chicane. The top figures show the bunch shape at various stages and the correlation between the internal position  $\zeta$  of an electron inside the bunch (and the charge density  $\rho$ , respectively) and its relative energy deviation  $\eta = (\gamma - \gamma_r)/\gamma_r$  where  $\gamma_r$  is the energy of a reference particle at the centre of the bunch: (a) before the cavity, (b) behind the cavity, (c) behind the magnetic chicane. In the RF cavity the particles are accelerated on the falling slope of the RF wave. Thereby the trailing electrons receive a larger energy gain than the leading ones. In the magnetic chicane the electrons at the tail move on a shorter orbit than those at the head and catch up. The ideal linear energy position correlation (chirp) is indicated by the black curves, the real nonlinear chirp results in the blue curves and the blue-shaded areas.

## 5. PRODUCTION OF SHORT ELECTRON BUNCHES

compensation process [66], has been proposed in [67]. The longitudinal phase space rotation in the velocity bunching process is based on a correlated time-velocity chirp in the electron bunch, in such a way that electrons on the tail of the bunch are faster than electrons in the bunch head. If the beam is injected in a long accelerating structure at the crossing field phase and it is slightly slower than the phase velocity of the RF wave, it will slip back to phases where the field is accelerating, but at the same time it will be chirped and compressed (See Fig.5.3). The key point is that compression and acceleration take place at the same time within the same linac section, actually the first section following the gun, that typically accelerates the beam, under these conditions, from a few MeV ( $> 4$ ) up to 25-35 MeV. In order to prevent irreversible

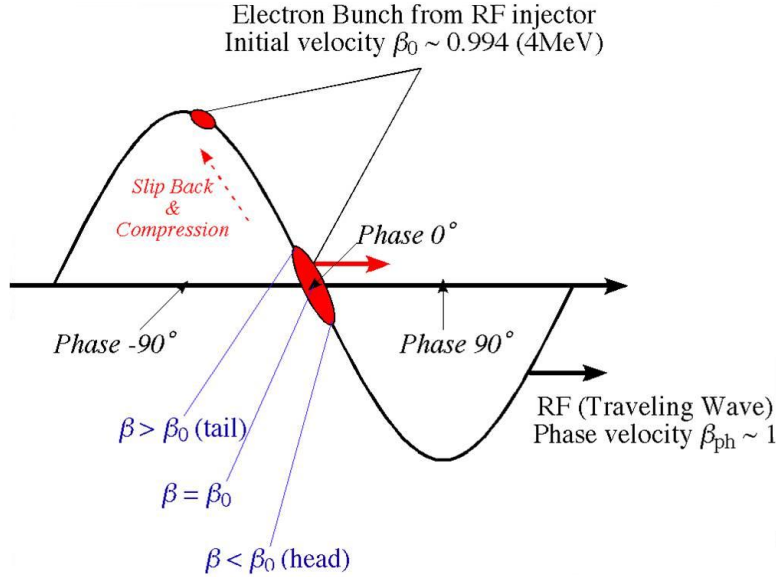


**Figure 5.3: Velocity Bunching cartoon** - The key point of Velocity bunching is that compression and acceleration take place at the same time within the same linac section

emittance growth during bunch compression the key issue is to preserve the laminarity of the beam. Mismatches between the space charge correlated forces and the external focusing gradient produce slice envelope oscillations that cause normalized emittance oscillations. It has been shown that to keep such oscillations under control during the velocity bunching, the beam has to be injected into the rf structure with a laminar envelope waist ( $\sigma' = 0$ ) and the envelope has to be matched to the accelerating and focusing gradients in such a way to stay close to an equilibrium mode.

## 5.2 Bunch Compression: Magnetic Chicane vs Velocity Bunching (VB)

The RF focusing force are actually too weak in a travelling wave structure [63] to provide sufficient beam focusing. A long solenoid around the accelerating structure is a convenient replacement to provide the necessary focusing. In this configuration the matching condition for the transverse rms envelope  $\sigma$  is given by

$$\sigma = \frac{1}{k} \sqrt{\frac{I}{4\gamma_0}} I_A \left( 1 + \sqrt{1 + \left( 4 \frac{\epsilon_n \gamma_0 k I_A}{I} \right)^2} \right) \quad (5.1)$$

where  $k = \frac{eB_{sol}}{mc^2}$ ,  $B_{sol}$  is the solenoid field,  $I_A = 17$  kA the Alfvén current,  $\epsilon_n$  the normalized emittance,  $\gamma_0$  and  $I$  are the values of the energy and the current at injection into the compressor. The main approximation leading to solution 5.1 consists on the assumption that the beam current grows linearly in the compressor as  $I = I_0 \gamma / \gamma_0$ . Nevertheless this result is confirmed by observations performed in several simulations of the rf compressor, indicating that best performances in terms of final beam brightness are achieved near the condition of beam flow at constant envelope (See Fig.5.4).

### 5.2.1 Experimental results of VB compression with emittance compensation at SPARC

During the experiments the drive laser was 7.3 ps FWHM long pulse, having a rms spot radius of 350  $\mu\text{m}$ . The bunch charge was 280 pC giving a maximum slice current of about 30 A without compression (See Fig.5.5). At the gun exit the beam energy was 4.4 MeV corresponding to a peak field on the cathode of about 100 MV/m, limited by rf breakdown. When the beam was accelerated on crest, using an accelerating field amplitude of 20 MV/m in the first two sections and 10 MV/m in the final section, the final energy was 148 MeV with an energy spread of 0.1% and an rms energy stability better than 0.1%. In Fig.5.5 is shown the rms bunch length measured at the linac exit ( $L_B \approx 3$  ps), with a measured minimum rms projected emittance of 1.5  $\mu\text{m}$  in both planes with the gun solenoid set to 2.46 kG (long solenoids off).

Figure 5.6 shows the measured rms bunch length  $\sigma_t$  versus the injection phase  $\phi$  of the first traveling wave structure. The corresponding measured rms compression factor  $C = \sigma_t(0)/\sigma_t(\phi)$ , the bunch length after on crest acceleration divided by the bunch length after compression, is also shown. The strong compression regime occurs when the phase shifts from  $-85^\circ$  to  $-95^\circ$ , as expected, with almost constant final energy and energy spread observed.

## 5. PRODUCTION OF SHORT ELECTRON BUNCHES

---

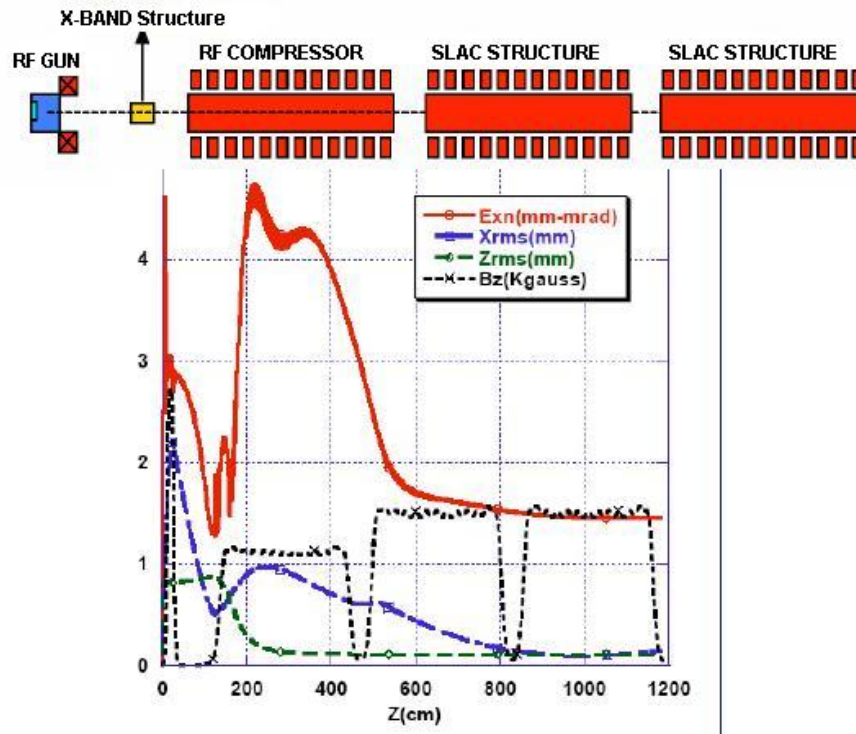


**Figure 5.4: Simulated evolution of the main beam parameters** - The simulation shows the process of the emittance compensation during the acceleration-compression in the first section of the SLAC linac. The figure also shows the solenoid magnetic fields that ensures a constant envelope during the process

## 5.2 Bunch Compression: Magnetic Chicane vs Velocity Bunching (VB)

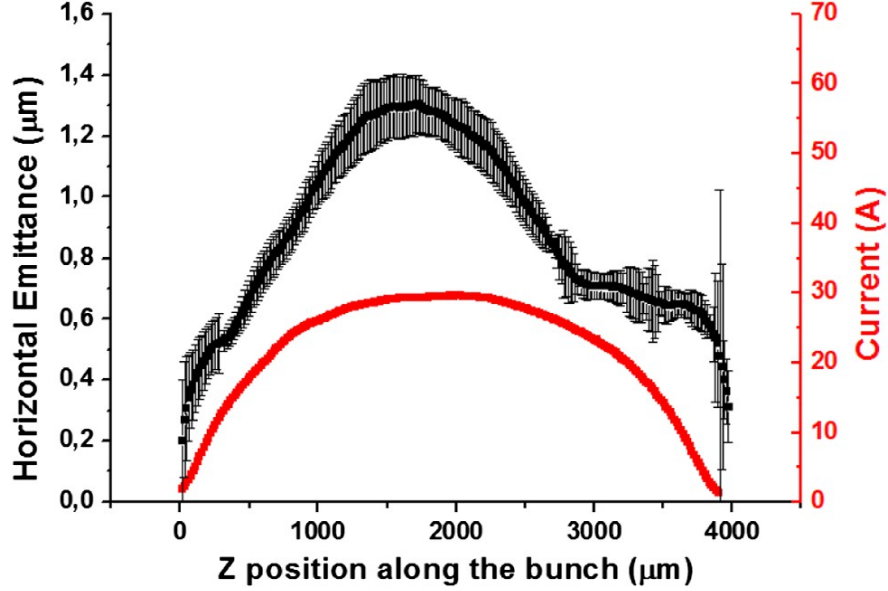


**Figure 5.5: Slice current and emittance for uncompressed beam** - Horizontal slice emittance and corresponding current profile (continuous lines), for the uncompressed beam. Gun solenoid set to 2.46 kG, long solenoids off. (The slice length is choice at 250  $\mu\text{m}$ )

The shortest measured rms bunch length is 210 fs (63  $\mu\text{m}$ ), limited by the longitudinal beam emittance. The final two measurements also illustrate the effect of overcompression when the phase setting exceeds  $-95^\circ$ . In Fig. 5.6 the results of PARMELA [52] simulations are also shown (dashed line). The agreement is quite satisfactory even in the over-compression regime. In Fig. 5.7 (left plot) the measured envelopes are shown in comparison with simulations for three different conditions: no compression (beam on crest), compression factor 3 with long solenoids off, same compression with long solenoids set to 450 G. The corresponding evolution of the emittances as simulated by PARMELA are shown in Fig. 5.7 (right plot). The effect on emittance compensation produced by the solenoids is clearly visible in the simulation and it is in good agreement with our measurements.

### 5.2.2 Results for VB compression of BLOW-OUT beam for Single Spike application at SPARC

To increase the beam current and obtain a shorter beam, the BLOW-OUT technique combined with the velocity bunching is used at SPARC. The beam is produced by

## 5. PRODUCTION OF SHORT ELECTRON BUNCHES

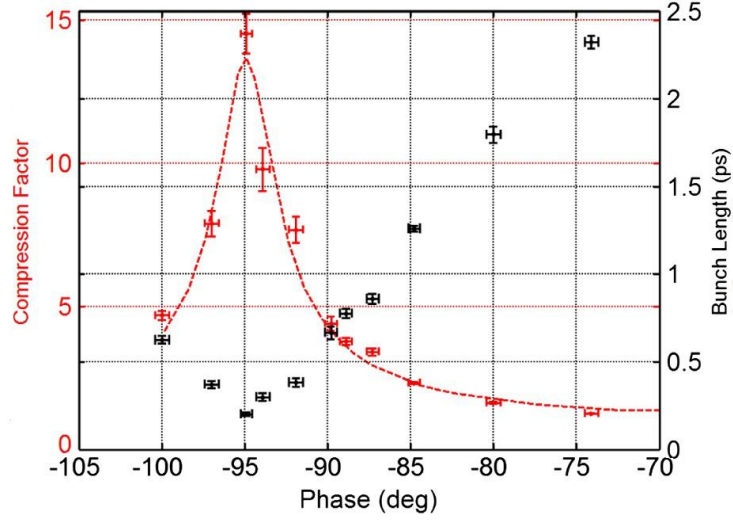


**Figure 5.6: Velocity Bunching compression results** - Measured rms bunch length (black) and corresponding compression factor (red) of a 280 pC beam versus the phase of the first traveling wave structure. PARMELA simulations are also shown with dashed red line.

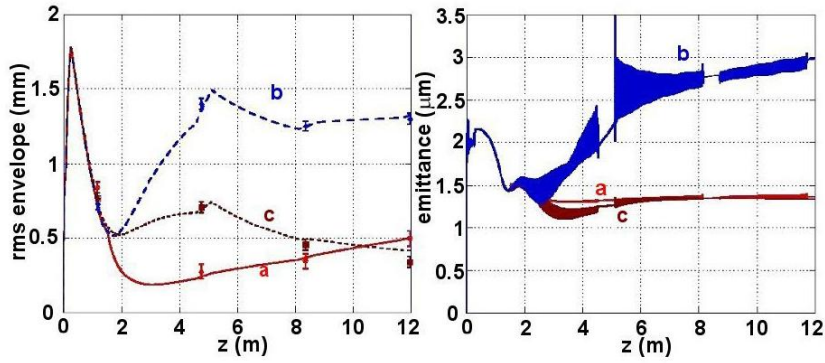


**Figure 5.7: Beam parameter evolution: experimental results and PARMELA simulation** - Measured envelopes and PARMELA simulations (left plot). Emittance evolution along the linac, PARMELA simulations (right plot). No compression (curves a), compression with long solenoids off (curves b), same compression with long solenoids set to 450 G (curves c).



## 5.2 Bunch Compression: Magnetic Chicane vs Velocity Bunching (VB)

an ultra-short UV laser pulse ( $\sigma_z \sim 200$  fs ) illuminating the cathode, the expansion of the beam due to the intense space charge in the first cm after the gun produced a low-charge beam (30-400pC) of about 5 MeV of energy with a duration of about 2 ps. An acceleration on crest of this beam lead to a beam with about 180 MeV, 1.5 mm-mrad of emittance and an energy spread lower than  $10^{-3}$  (See Fig.5.1). The beam is compressed in velocity bunching to obtain short bunch with high current. The phase space and the main parameters for single spike regime are shown in Fig.5.8. The compression introduces a strong chirp in the energy, the mean value is about 7 keV/ $\mu$ m. The compression factor is chosen in order to reach the maximum brilliance. The final length is 400 fs RMS with an energy of about 120 MeV, a table with a complete list of the measured parameter for FEL application will present in the Chapter (6). The

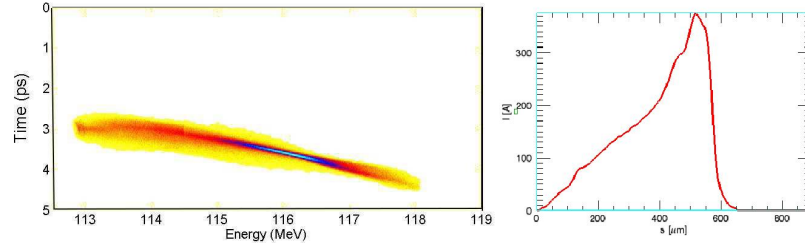


**Figure 5.8: Longitudinal phase-space and current profile of compressed bunch at SPARC** - (Left) The phase space of strong chirped beam. (Rigth) Measured current along the bunch

projected emittance is about 2 mm-mrad in both the plane and a mean energy spread slice of about  $5 \cdot 10^{-3}$ . The measured values are affected by the nonlinearities in the tail and head of the beam, in fact the slice parameters in the core of the beam where the current is highest are lower than the projected ones. The beam given by componing the BLOW-OUT regime with the velocity bunching is a good candidate for the single spike regime. The high current with a compensation of the emittance give us a set of parameter that allow to saturate in the six undulator sections of SPARC. On the other hand the beam has lower energy respect to the 'in crest' beam and a strong chirp in energy. The first lack limits us in the wavelength range ( $\lambda_r \sim 1/\gamma^2$ ), while the second imposes a taper configuration strategy to lasing. However this solution permits a single spike regime even if the bunch length is longer than the single spike length. This is due to the selection of the beam part in resonance with the taper undulator. Typical value

## 5. PRODUCTION OF SHORT ELECTRON BUNCHES

---

of the single spike length at SPARC is in the order of 200 fs FWHM and for a 400 fs RMS bunch length we expect almost four spike. This happens for a K-constant value of the undulator, where each part of the beam radiate independently and the FEL pulse is composed by few spikes with low energy and a broad band spectrum (See Chap.(6)).

## 6

# Experimental and Simulation Results of SASE Single Spike FEL at SPARC

In this chapter we present the experimental results for the SASE single spike regime with energy chirped electron bunch and a tapered undulator configuration.

The experimental results are compared with the simulation results of the extended version of Genesis 1.3[68], which includes the higher harmonics and the cascade configuration. The e-beam properties (emittance, energy mean-spread and current) are defined in the simulations with a look-up table where the main slice values, measured before the undulator entrance, are listed. The experimental results are in a good agreement with the single spike theory and the simulations show a similar behaviour observed in the experiments. The measured pulse quantities are the spectrum and the absolute energy value.

### 6.1 Single Spike SASE at SPARC

The single spike length refers to the distance along the electron bunch where there is a correlation between the phases of the radiation pulses emitted by the electrons. This distance is about an half of the slippage length therefore the maximum single spike length for the whole SPARC undulator lasing at 540 nm is  $\sim 120 \mu\text{m}$ . This length is the FWHM of the electron beam that allows to work in single spike regime.

## 6. EXPERIMENTAL AND SIMULATION RESULTS OF SASE SINGLE SPIKE FEL AT SPARC

---

The emitted radiation is a single coherent spike with a width shorter than the single spike length. However to obtain such short beam, as shown in the last chapter, a compression scheme must be involved. The velocity bunching compression produces beams with higher current than the uncompressed ones, but the resulting longitudinal phase space is characterized by a linear chirp in the energy and the beam is often longer than the single spike length. In fact the beam compression has to be chosen in order that the beam properties satisfied the FEL requirements.

Therefore the strategy is to achieve the minimum beam length with the best parameters. At SPARC this is accomplished by combining the blow-out regime on the cathode, which generates a 2 ps (RMS) beam after the gun and the VB technique with a compression factor of about 5. To investigate the behaviour of such beam we start with the ideal case of Gaussian unchirped beam with the parameters listed in Tab.6.1:

Energy [MeV]	115.2
Energy Spread [%]	0.3
Energy Chirp [keV/ $\mu\text{m}$ ]	0
Norm. Emittance [mm-mrad]	1.5
Beam length(RMS) [ps]	0.4
Transverse dim. [ $\mu\text{m}$ ]	120
Peak Current [A]	400

**Table 6.1: Ideal beam parameters**

The theoretical prediction (1D-3D) and the simulation results are listed in Tab.6.2: The agreement between theory and simulation, taking into account the 3D effects, is quite satisfactory. In Fig.6.1 the power and bandwidth evolution along the undulator are shown vs  $z$ . The power amplification on left shows an exponential amplification of the field until the fourth undulator sections. Taking into account the undulator interruptions, the saturation length is about 8.8 m, i.e. a gain length of  $0.7 \text{ m}$  ( $L_{sat} = 4\pi L_g$ ), while the saturation power is about 100 MW. After the saturation the peak power does not show the oscillatory behaviour, but continues to grow weakly due to the fresh electron in the head of the beam and it reaches a final power of about 300 MW. The bandwidth shows the typical scaling ( $b_w \sim 1/\sqrt{z}$ ) and reaches its minimum of about  $5 \cdot 10^{-3}$  at saturation.

The evolution of the temporal FEL pulse profile and spectrum are shown in Fig.6.2.

Parameter	1D theory	3D theory	Simulation
$\rho[10^{-3}]$	7	3.4	3.2
$L_c[\mu\text{m}]$	6.2	12.5	13.5
$L_g[\text{m}]$	0.32	0.65	0.7
$L_{SS}[\mu\text{m}]$	39	78.5	85
$P_{sat}[\text{MW}]$	330	118	100
$b_w[\%](\text{min})$	0.7	0.34	0.5
spike number	4	3	3

**Table 6.2: Ideal beam results:** The gain length in the simulation is the inverse of the mean increment during the exponential amplification, from its value is possible to calculate the cooperation length and the effective  $\rho$

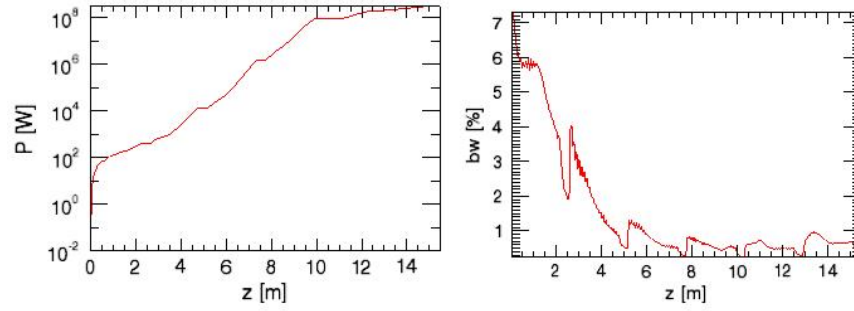


**Figure 6.1: Simulation results for an ideal Gaussian beam ( $L_b^{RMS} = 400\text{fs}$ ) lasing at 540 nm** - Power and bandwidth evolution along the undulator of the ideal Gaussian beam

## 6. EXPERIMENTAL AND SIMULATION RESULTS OF SASE SINGLE SPIKE FEL AT SPARC

---

In the first row, the beam profile and the spectrum after the first undulator section at the end of the lethargy stage are shown. In the second row there are the same quantities during the exponential gain where are evident the multispike structure of the beam in both time and frequency space. At the end of the fourth section (third row) the pulse is composed by a overlap of the spikes due to slippage. At the end of the undulator (fourth row) the spike continues to grow with a multispike structure, the effective number of spikes with high power is about three-four.

Other simulations with higher emittance and energy spread show a similar behaviour with a small change in the principal results and in agreement with the theory. In particular the simulations for this ideal beam without the energy chirp show that with this kind of beam single spike pulse cannot be achieved. In reality the compression mechanism introduces a linear energy chirp along the beam and it generates a peaked current distribution. The gain curve along the beam is strongly affected by the slice parameters. The FEL pulse generated by means of the previous bunch in K-constant undulator is a chirped multispike low-power pulse. The 'pulse slicing' of this kind of radiation using a monochromator for X-ray is discussed in ref.[69].

### 6.2 Single Spike SASE with Energy Chirped Electron Beam

The effect of the chirp on the gain can be compensated by tapering the undulator[5]. The compensation mechanism can be explained analysing the diagrams shown in Fig.6.3. The pictures represent the propagation of a field spike (green) developing on the rear part of a chirped e-beam (light blue). The vertical axis represents the resonant condition which depends on the relative position between the beam and the radiation. The upper diagram is relative to the un-tapered case. When the beam propagates through the undulator, the slippage process leads the spike out of resonance. When the chirp is combined with an appropriate undulator taper (lower diagram), the resonance condition can be preserved.

The resonant wavelength for an energy chirped electron beam is a function of the position along the undulator. For a linear chirp along the bunch we may define the local mean energy as

$$m_e c^2 \gamma(s) = m_e c^2 \gamma_0 + \alpha(s - s_0) \quad (6.1)$$

## 6.2 Single Spike SASE with Energy Chirped Electron Beam

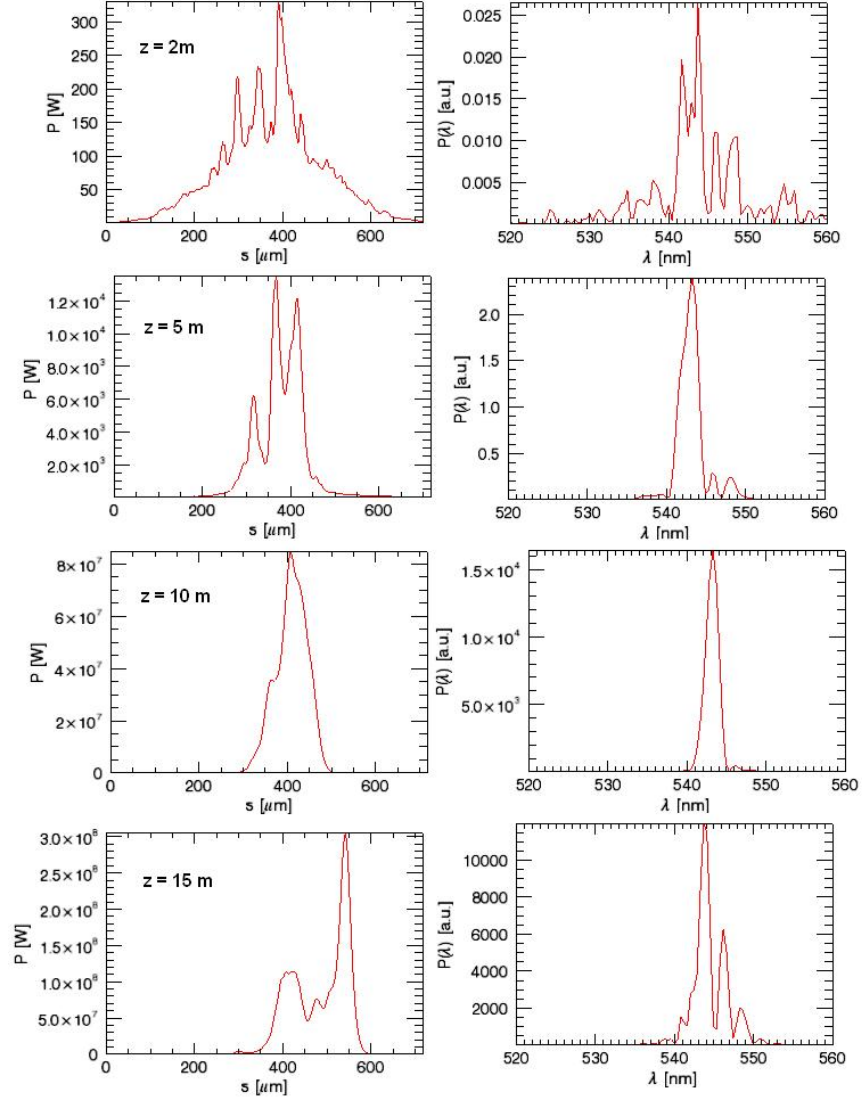
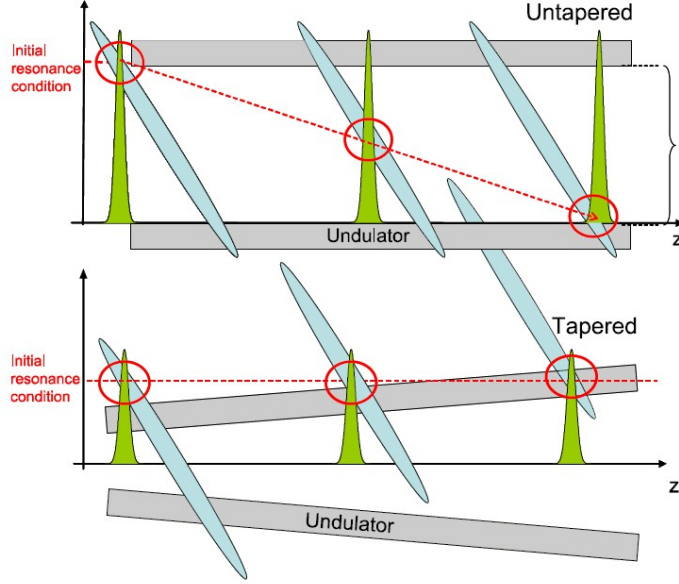


Figure 6.2: Simulation results for an ideal Gaussian beam ( $L_b^{RMS} = 400\text{fs}$ ) - Power and bandwidth shape at different locations  $z$  along the undulator

## 6. EXPERIMENTAL AND SIMULATION RESULTS OF SASE SINGLE SPIKE FEL AT SPARC



**Figure 6.3: Chirp-taper cartoon scheme** - The pictures represent the propagation of a field spike (green) developing on the rear part of a chirped e-beam (light blue). The upper diagram is relevant to the un-tapered case, the lower one to the tapered case.

where  $s$  corresponds to the longitudinal coordinate along the electron bunch centred in  $s_0$  in a reference frame drifting at the velocity  $\beta_{\parallel}$ . The parameter  $\alpha$  defines the slope of the average slice energy vs. the coordinate  $s$ . The different velocity of the light with respect to the electrons brings a radiation spike building up in a given position, out of resonance when it slips of a distance of the order of  $\delta s \approx m_e c^2 \rho \gamma / (2\alpha)$ . For this reason an inhomogeneous gain broadening, associated to energy spread, is expected even with a negligible local energy spread because of slippage. The field in presence of gain propagates at a velocity lower than  $c$ , the peak of a spike in the exponential gain regime is expected to move at a velocity given by Eq.2.83. Above saturation the front side of the pulse drifts at the velocity of light  $c$ . Approaching saturation the radiation peak shifts at a different velocity than  $v_s$ , closer or even higher than  $c$  because of the pulse shortening associated to the electron synchrotron oscillation [70]. A taper of the undulator may be used to compensate the effect of energy dispersion associated to the pulse slippage on the chirped beam. The energy change caused by the chirp and observed at the peak of the radiation pulse may be expressed as

$$m_e c^2 \gamma(z) = m_e c^2 \gamma_0 + \chi \alpha z \frac{\lambda_r}{\lambda_u} \quad (6.2)$$



## 6.2 Single Spike SASE with Energy Chirped Electron Beam

where  $z$  is the coordinate along the undulator,  $\gamma_0$  is the Lorentz factor at the undulator entrance ( $z=0$ ), at the position along the bunch where the spike will grow, and where  $\chi$  is a coefficient accounting for an arbitrary propagation velocity of the radiation  $v_s$ . For  $v_s = c$  we have  $\chi = 1$ , for  $v_s$  given by Eq.6.1 we have  $\chi = 1/3$ . Inserting Eq.6.2 in the resonant condition 6.1 and solving for the undulator  $K$  we obtain a taper scaling which preserves the resonance condition during propagation

$$K(z) = \sqrt{2 \left[ \frac{\lambda_r}{\pi} \left( \gamma_0 + \alpha \chi z \frac{\lambda_r}{\lambda_u} \right)^2 - 1 \right]}. \quad (6.3)$$

We have tested the effect of the tapered undulator with the SPARC FEL operating in velocity bunching mode. The central wavelength used in the experiment is 540 nm and the corresponding  $\beta_T$  Twiss coefficient is about 1.5m. The longitudinal phase space measured with the RF deflector cavity used in combination with the dipole spectrometer is shown in Fig.6.4. A list of the beam parameters measured before the injection of

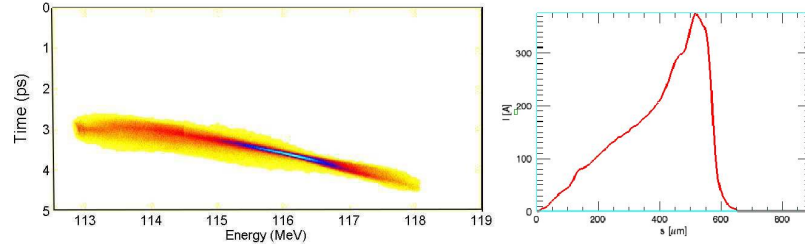


**Figure 6.4: Longitudinal phase-space and current profile of compressed bunch at SPARC** - (Left)The phase space of strong chirped beam.(Rigth)Measured current along the bunch

the beam in the undulator is presented in Tab.6.3 and is chosen as a reference case for the simulations. The operation in compression mode, i.e. with the first linac section at a phase close to zero crossing, is very sensitive to phase drift and jitter, and, as consequence, we use in the simulations a variable range of the emittance  $[1.5 \pm 0.75]$  mm-mrad, the energy spread slice  $[0.37 \pm 0.05]\%$  and, correlated by the compression, the current  $[380 \pm 28]\text{A}$  and the bunch length  $[0.42 \pm 28\%]$ . Varying this values and the random number generator of electrons distribution we compare the statistical fluctuation given by the simulations with the experimental ones.

The radiation diagnostic in the experiments is based on the in vacuum spectrometer. In Fig. 6.5 it is shown a typical spectrum collected with three undulator gaps set to

## 6. EXPERIMENTAL AND SIMULATION RESULTS OF SASE SINGLE SPIKE FEL AT SPARC

Energy [MeV]	115.2
Energy Spread projec.[%]	1.15
Energy Spread slice[%]	0.3
Energy Chirp [keV/ $\mu\text{m}$ ]	$6 \pm 1.5$
Norm. Emittance [mm-mrad]	2
Beam length [ps]	0.42
Beam Charge [pC]	300
Peak Current [A]	380

**Table 6.3: Compressed beam parameters**

the resonant wavelength of 540nm (at the mean beam energy).

The vertical structure in the spectrum image is due to the radiation diffraction caused

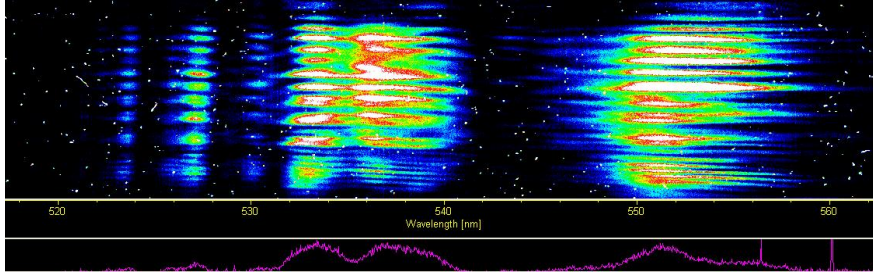


**Figure 6.5: Experimental spectrum with three undulator sections closed** - Single shot spectrum acquired with three undulator closed. The vertical axis represents the vertical position at the spectrometer entrance slit. The window is centred at 540nm and the window width is 45nm.

by the vacuum pipe. With the first three undulator set at resonance and the last three undulators opened, the radiation has to propagate through about 8 m of vacuum pipe without gain guiding.

The structure disappears in Fig.6.6, obtained with six sections tuned at the resonance of 540nm (un-tapered undulator).

The strong chirp in the electron bunch shows up as a broadband spectrum filling up the wavelength acceptance window of the spectrometer. A statistical analysis of the collection of 100 spectra acquired in this condition provided the histograms shown in Fig.6.7. The average pulse energy obtained in these conditions is  $7.8\mu\text{J}$ . The r.m.s. of the distribution is comparable to the mean value ( $8\mu\text{J}$ ). A beam file with the measured parameters of the compressed beam listed in Tab.6.3 is used to simulate in Genesis the

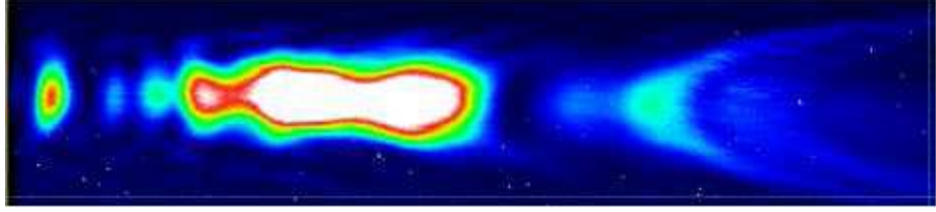


**Figure 6.6: Experimental spectrum at the exit of the untapered undulator** - As in Fig.6.5, single shot spectrum acquired with six undulators set at the resonance of 540nm

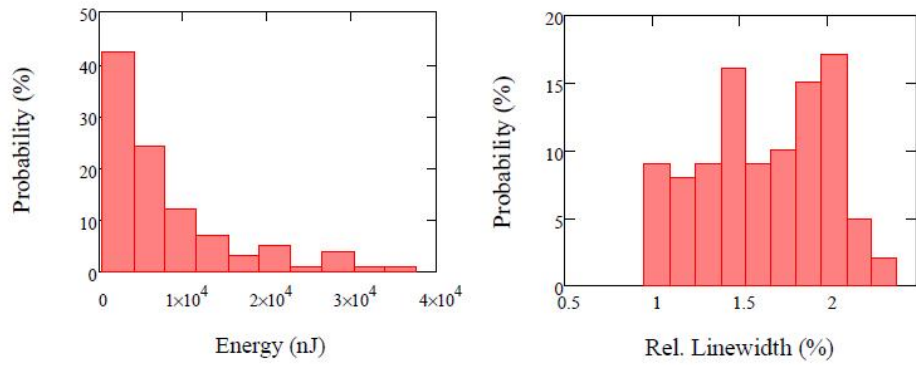


**Figure 6.7: Experimental histograms of the energy and the relative linewidth** - Histogram of the energy (left) and spectral width (right) obtained with the untapered undulator, with the resonance set at 540nm

## 6. EXPERIMENTAL AND SIMULATION RESULTS OF SASE SINGLE SPIKE FEL AT SPARC

behaviour of the bunch in a K-constant undulator. The current profile and the longitudinal phase space are the same shown in Fig.6.4. The parameters are those of reference in Tab.6.3 and the normalized strength of the undulator K is 1.

The main results are shown in Fig.6.8, the pulse at saturation is composed by two near temporal spike (right-bottom) due to the short region in which the current is high. The spectrum (right-top) shows a broadband signal and it is composed by many spikes similar to the experimental (See Fig.6.6) with a minimum bandwidth (left-bottom) that is comparable with the experimental one (1.5%). The exponential gain is reduced by the off resonance induced by the slippage, the peak power is about two order of magnitude lower than in the tapered configuration.

In order to compare the spectra with the simulations the field data generated by

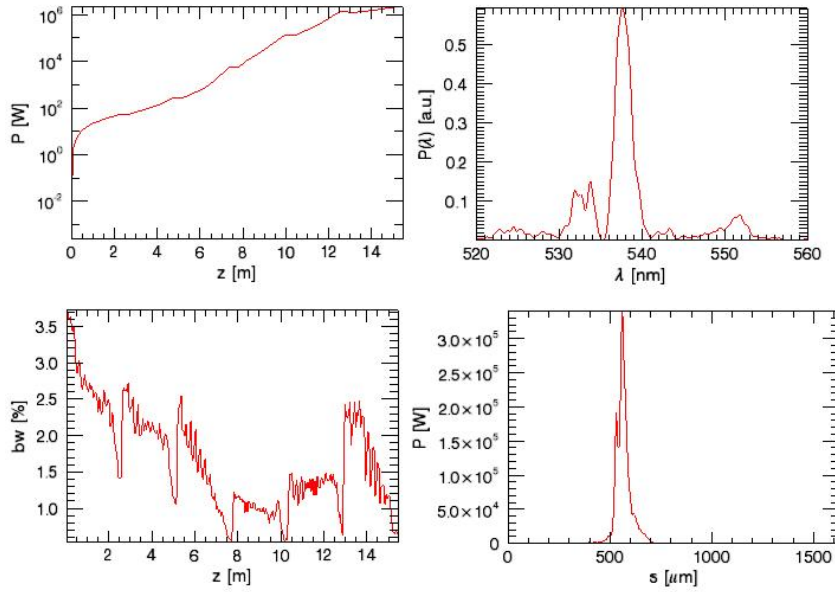


**Figure 6.8: Genesis simulation evolution of chirped beam in untapered undulator** - The amplification of the radiation (left-top) stops at the end of the fourth undulator section, after as shown in bandwidth evolution (bottom-left) the FEL goes out of resonance and a broadband spectrum is emitted by the e-beam (right-top). The pulse shape has about two spikes, this is due to the shortness within the beam where there are high current, low emittance and low energy spread

GENESIS have been post processed through a numerical procedure resembling the slit/grating/CCD of the spectra detection system. A reconstructed spectra for the un-

## 6.2 Single Spike SASE with Energy Chirped Electron Beam

taper simulation is shown in Fig.6.9, the behaviour is similar to the experimental one characterized by low power and a broadband spectrum.

The energy evolution is shown in Fig.6.10, the solid line is the genesis output while the

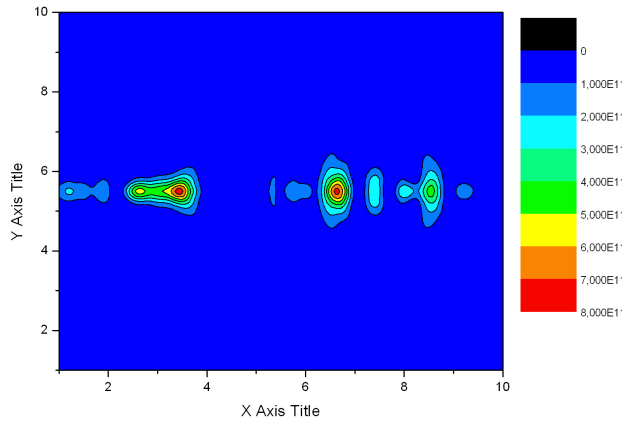


**Figure 6.9: Reconstructed spectrum by the simulated data for untapered undulator** - The field data generated by GENESIS have been post processed through a numerical procedure resembling the slit/grating/CCD of the spectra detection system, the figure shows the spectrum in untapered configuration the horizontal axis is centred at 540 nm and the width is 45 nm. The spectrum is quite similar to the experimental one plotted in Fig.6.6

asterisks are the experimental mean value over 100 shots (the fluctuation are 100%), the agreement is quite good. The simulation was been done with the reference parameters listed in Tab.6.3.

The technique used to compensate the chirp with the taper was that of progressively closing the gaps one module at the time, starting from the first one while observing the emitted spectrum. For each module we found the gap minimizing the spectral width. During this procedure we observed a blue-shift of the resonant frequency and in order to compensate it we opened more the first sections of the undulator. This procedure lead to the set of gaps corresponding to the resonance frequencies (at 116 MeV) shown in Fig.6.11, where the changes in the gaps is shown, i.e. the resonant wavelength, that allowed to minimize the bandwidth (Fig.6.11[Taper A]) and the taper shift that compensates the blue-shift (Fig.6.11[Taper B]). The theoretical scaling given by the Eq.6.3,

## 6. EXPERIMENTAL AND SIMULATION RESULTS OF SASE SINGLE SPIKE FEL AT SPARC

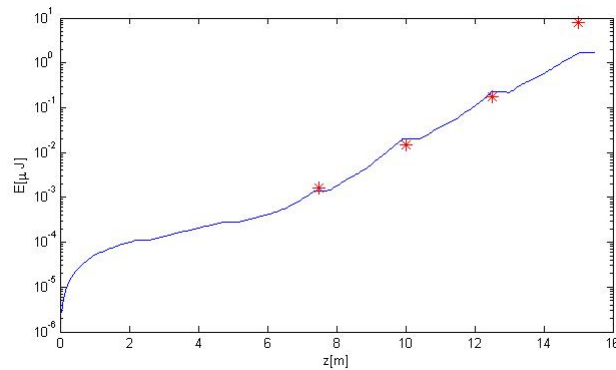


**Figure 6.10: Energy exponential gain: Genesis and experimental results** - The energy simulation results, obtained with reference parameters, are in quite good agreement with respect the experimental one (\*) taking into account the strong energy fluctuations.

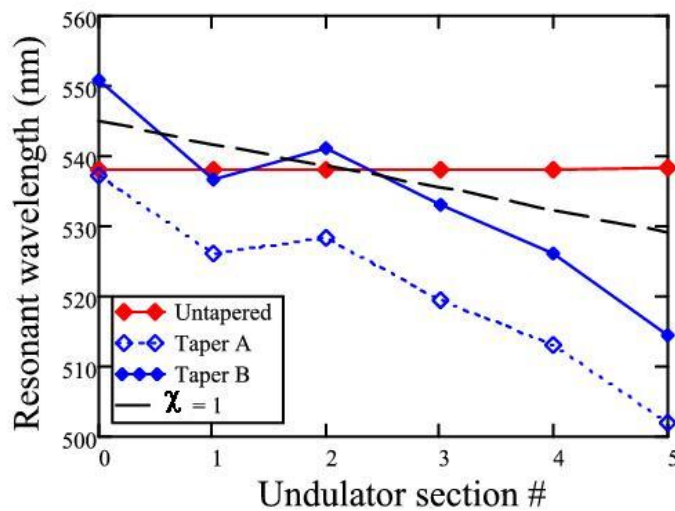


**Figure 6.11: Resonant wavelength for taper and untaper undulator** - The red line is the untapered K value to lase at 540 nm with the mean energy value. The black dashed line is the theoretical scaling taper given by Eq.6.3 with  $\chi = 1$ . The procedure to choice the undulator gaps are in order to minimize the bandwidth(blue dashed line). The shifted curve(blue full line) is to compensate the blue shift observed during the experiment and is the same used in the simulations.

## 6.2 Single Spike SASE with Energy Chirped Electron Beam

with  $\chi=1$ , is the dashed line in Fig.6.11. After the tapering procedure, with the resonant frequency per undulator as shown in Fig.6.11, we have obtained a substantial increase of the pulse energy which reached  $140\mu\text{J}$  with a standard deviation of about  $100\mu\text{J}$  and a reduction of the average linewidth which was  $8 \cdot 10^{-3}$  averaged over 100 pulses. In Fig. 6.12 the histograms relevant to the statistics of the pulse energy and relative linewidth for the 100 shots are shown.

Several spectra in the acquired set were characterized by a spectral pattern similar to

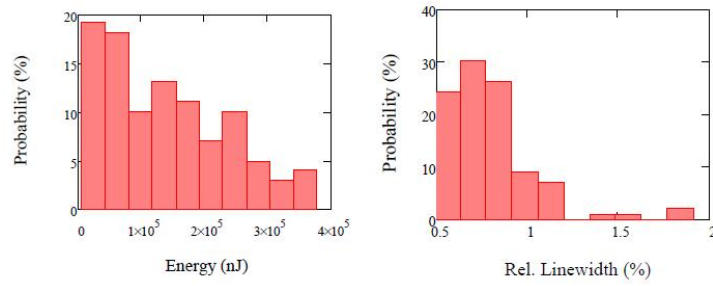


**Figure 6.12: Experimental histograms of the energy and the relative linewidth** - Histogram of the energy (left) and spectral width (right) obtained with the tapered undulator, with the resonance set at 540nm

the one shown in Fig.6.13, constituted by a single coherence region (no multiple SASE spikes). The pulse energy in the spectrum of Fig.6.13 is about  $260\mu\text{J}$ . The red dashed line corresponds to a Gaussian profile fitting the main structure in the spectrum with a spectral width of 1.65nm. A Fourier limited pulse would have an rms length of 46fs and a peak power of about 900MW.

The simulation results with the reference case beam (Tab.6.3) are shown in Fig.6.14 and then post processed. The reconstructed image shows a single spike spectrum in Fig.6.15. The right column of Fig.6.14 shows, respectively from the top, the pulse shape with current profile (dashed blue) and the spectrum at saturation, the single spike signature is evident. The simulated pulse for the reference case has an rms length of 50 fs, a peak power of 120 MW and an energy of  $45 \mu\text{J}$ .

The experimental results of the energy vs the bandwidth for untapered and tapered configuration are shown in Fig.6.16. In the tapered configuration the mean energy is about 20 times the untapered one, while the bandwidth is halved. The experimental and simulated histograms of the energy are presented in Fig.6.17, the results are compatible with the experimental in the mean energy region. The mean energy simulated

## 6. EXPERIMENTAL AND SIMULATION RESULTS OF SASE SINGLE SPIKE FEL AT SPARC

---

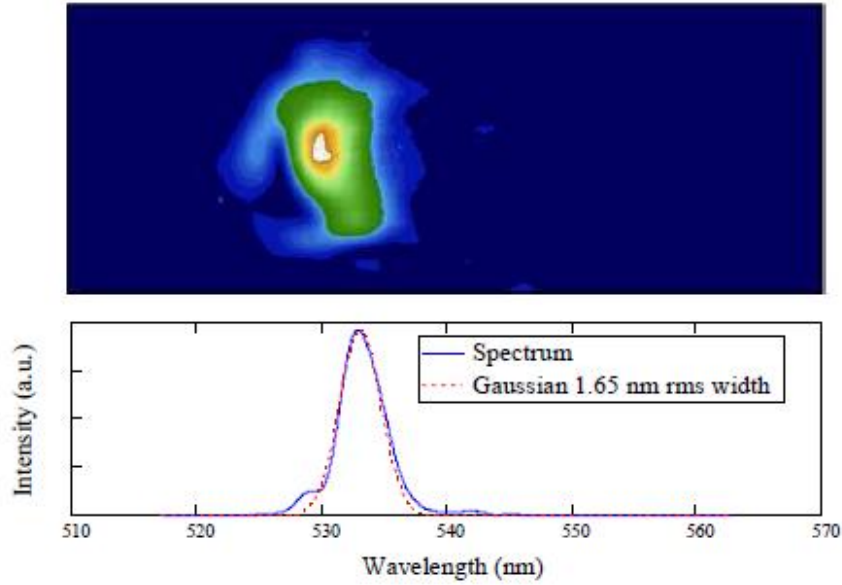


**Figure 6.13: Experimental Single Spike spectrum** - Typical spectrum showing a single coherence region (single spike)

is about  $130 \mu\text{J}$  which is comparable with the experimental ( $140 \mu\text{J}$ ), a spectral width of  $1.5 \text{ nm}$  and the RMS-length of about  $45 \text{ fs}$ . The agreement with the experimental results is quite good and the spectrum is composed by a single coherent region.



## 6.2 Single Spike SASE with Energy Chirped Electron Beam

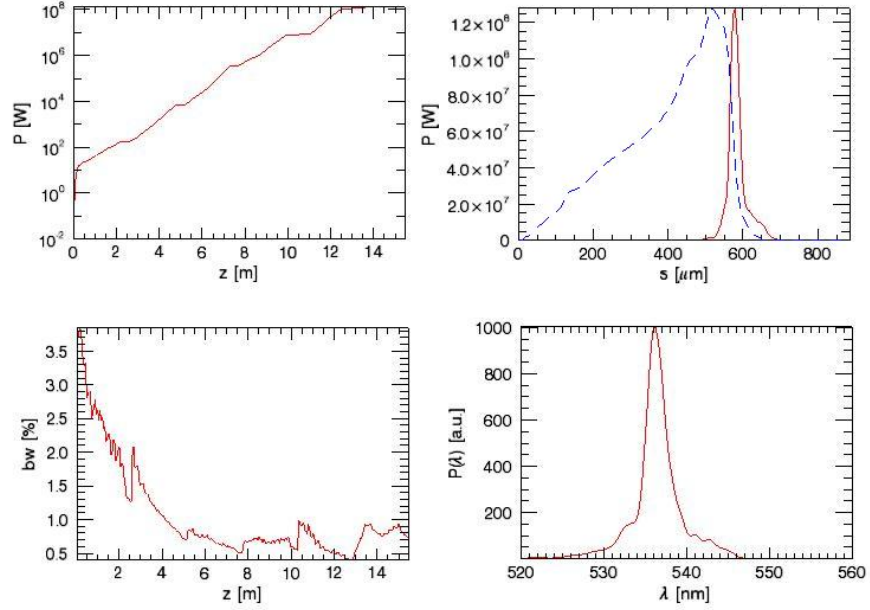


**Figure 6.14: Genesis simulation of chirped beam with tapered undulator** - The left column shows the exponential gain and the bandwidth evolution, the right column shows the pulse profile with the e-beam current profile (blue dashed line) and the spectra at saturation

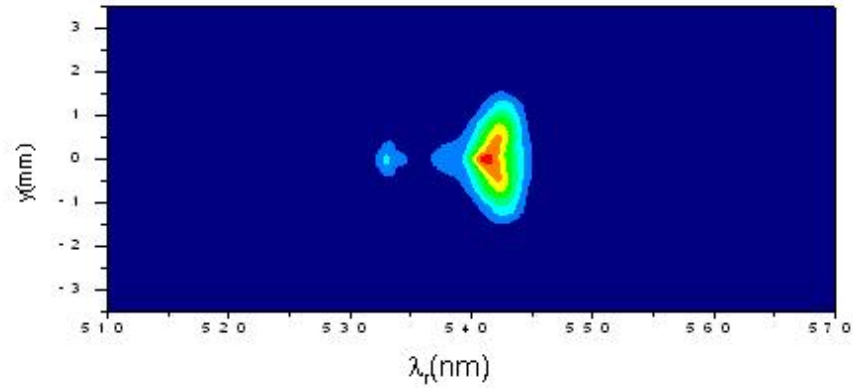


**Figure 6.15: Reconstructed spectrum by the simulated data for tapered undulator** - The field data generated by GENESIS have been post processed through a numerical procedure resembling the slit/grating/CCD of the spectra detection system, the figure shows the spectrum in tapered configuration the horizontal axis is centred at 540 nm and the width is 45 nm. The single spike spectrum is like the experimental one plotted in Fig.6.13

## 6. EXPERIMENTAL AND SIMULATION RESULTS OF SASE SINGLE SPIKE FEL AT SPARC

---

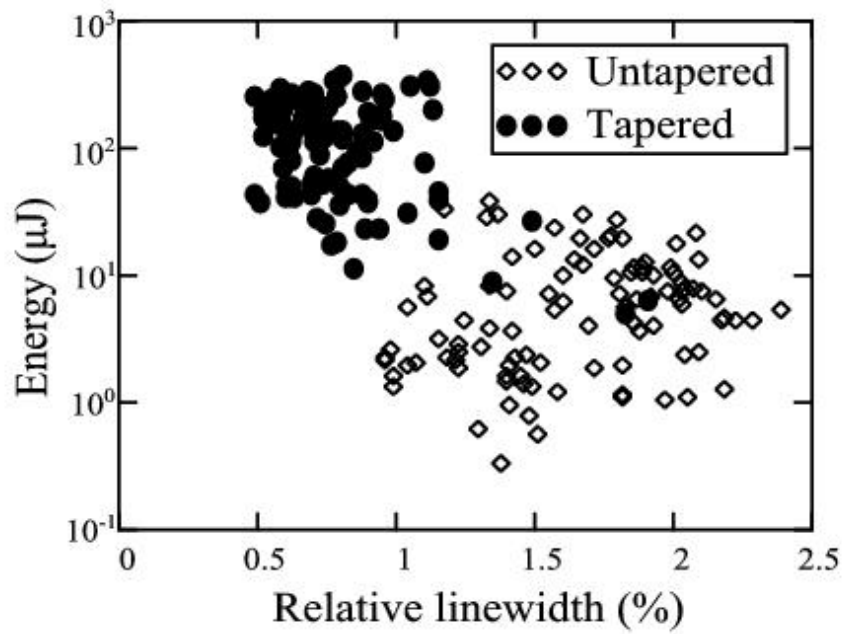


**Figure 6.16:** Energy vs bandwidth experimental results - The plot shows the experimental transition between untapered to tapered configuration

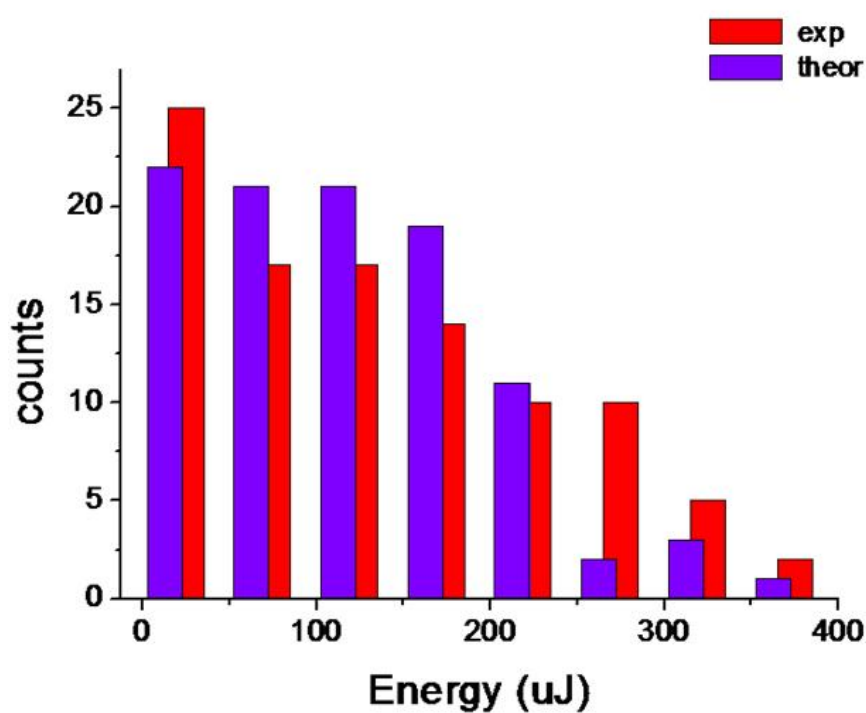


**Figure 6.17: Comparison between experimental and simulated statistic results**  
 - Results of Genesis with different beam parameters and random numerical seeds: experimental in red and simulations in blue

## 6. EXPERIMENTAL AND SIMULATION RESULTS OF SASE SINGLE SPIKE FEL AT SPARC

---

# Experimental and Simulation Results of Superradiant Single Spike in a HGHG-FEL

A major advantage of the HGHG FEL is that the output properties at the harmonic wavelength are a map of the characteristics of the high-quality fundamental seed laser. This results in a high degree of stability and control of the central wavelength, bandwidth, energy, and duration of the output pulse. As the duration of the HGHG radiation reflects the seed pulse characteristics, the output radiation pulse can be made shorter than the electron bunch length by simply using an appropriate duration seed laser pulse synchronized to the electron beam. In this section we analyse the FEL operation in seeded mode with the SPARC undulator arranged as a single long amplifier lasing at 400nm. In the first section we present the measured beam properties and the simulation of the SASE and SEED regime in order to emphasize the different between the two regime. In the second section the experimental results are presented for the first eleventh harmonics and the comparison with the Genesis [68] and Perseo [71] simulations results. The agreement between theory, simulations and experiments is good for the odds harmonics. For the even harmonics the simulation power output is lower than the experimental ones. Another interesting effect is a modulation in the spectrum of the fundamental wavelength with a periodicity of about 0.5 nm, observed both in the experiments and simulations.

## 7. EXPERIMENTAL AND SIMULATION RESULTS OF SUPERRADIANT SINGLE SPIKE IN A HGHG-FEL

---

### 7.1 Beam Characterization and SASE Simulation for SEED Experiments

The beam chosen to work in the seeded regime is obtained with the blow-out regime followed by the maximum acceleration in the linac. An experimental optimization of the beam quality is done with the right choice of the focusing solenoid of the gun and the beam charge. The beam parameters measured after the linac are listed in Tab.7.1, the seed pulse is Gaussian with a 120 fs RMS length and an energy of about 3  $\mu$ J, the waist of the seed is at half of the first undulator section.

The first informations about the evolutions of such beam comes from the analysis of

Parameter	Uncompressed
Energy [MeV]	177.2
Energy Spread projec. [%]	0.13
Energy Spread slice [%]	0.05
Norm. Emittance x [mm-mrad]	2.9
Norm. Emittance y [mm-mrad]	2.5
Beam length [ps]	2.64
Beam Charge [pC]	400
Beam Current [A]	54

**Table 7.1: Beam parameters for HGHG**

the SASE regime. The results of the main parameters for a 2 ps flat top beam with a current of 72 A are listed in Tab.7.2.

The main results for SASE simulation are shown in Fig.7.1, where in the (a) windows are shown the peak power evolution of the fundamental(red) and odd harmonics the 3rd(green), 5th(blue) and 7th(black). In the (b) window are shown the peak power evolution of the even harmonics 2nd(red), 4th(blue) and 6th(black). The harmonics emission is inhibited by the exponential growth of the fundamental harmonic, when the power of the fundamental reaches few MW than the harmonics start to grow exponentially. In the (c) windows is shown the bandwidth evolution that reaches its minimum (0.2%) at saturation and it is comparable with the  $\rho$  value. In (d) window is shown the temporal multispikes pulse at saturation, the simulated windows is only a fraction of the whole beam but it is however useful to show the behaviour of the beam and the

## 7.2 Superradiant Spike Generation in HGHG SEED FEL

Parameter	1D theory	3D theory	Simulation
$\rho[10^{-3}]$	3.2	2	1.9
$L_c[\mu\text{m}]$	5.8	9.1	9.7
$L_g[\text{m}]$	0.4	0.64	0.67
$L_{SS}[\mu\text{m}]$	36.4	51.2	61
$P_{sat}[\text{MW}]$	40	25	24
$b_w[\%](\text{min})$	0.32	0.2	0.2

**Table 7.2: High harmonics in SASE regime results:** The gain length in the simulation is calculated as the inverse of the mean increment during the exponential amplification, from its value is possible to calculate the cooperation length and the effective  $\rho$

powers of the harmonics. The energy of the first seven harmonics are respectively 17.2  $\mu\text{J}$ , 0.9 nJ, 0.27  $\mu\text{J}$ , 0.27 nJ, 12.4 nJ, 0.225 nJ, 3.52 nJ. The length of the seed pulse is 120 fs with variable energy because we use a dedicated amplifier system. The seed length is of the order of the single spike length for this set of parameters and it is a good candidate to observe the self similar evolution and superradiance during the SEED FEL interaction.

## 7.2 Superradiant Spike Generation in HGHG SEED FEL

The spectra shown in Fig.7.2 were acquired with all the undulator modules tuned to 400 nm, after ensuring temporal and spatial overlap between the seed and the electron beam. The vertical axis on the image represents the vertical position on the input spectrometer slit, while the horizontal axis represents the wavelength. The window is centred at 400 nm and the represented wavelength range is about 45nm. The figures Fig.7.2(a) to Fig.7.2(c) represent spectra obtained at different seed energy as indicated in the figure caption. The multi-peak structure, corresponding to the presence of various spectral lines, slightly red-shifted compared to the unseeded and HHG is about a factor two larger than the expected SASE bandwidth. The Pierce parameter  $\rho$  is  $3.2 \cdot 10^{-3}$ , corresponding to a bandwidth of the order of 1.3 nm, while the spectrum in Fig.7.2(c) is larger than 2 nm. The observed pattern, appearing at high seed energy (Fig.7.3), is completely different both in shape and in intensity from the typical SASE spiking where the number of peaks and their position change from shot to shot. The sidebands structure which appears in the spectrum at high seed energy only, is a

## 7. EXPERIMENTAL AND SIMULATION RESULTS OF SUPERRADIANT SINGLE SPIKE IN A HGHG-FEL

---

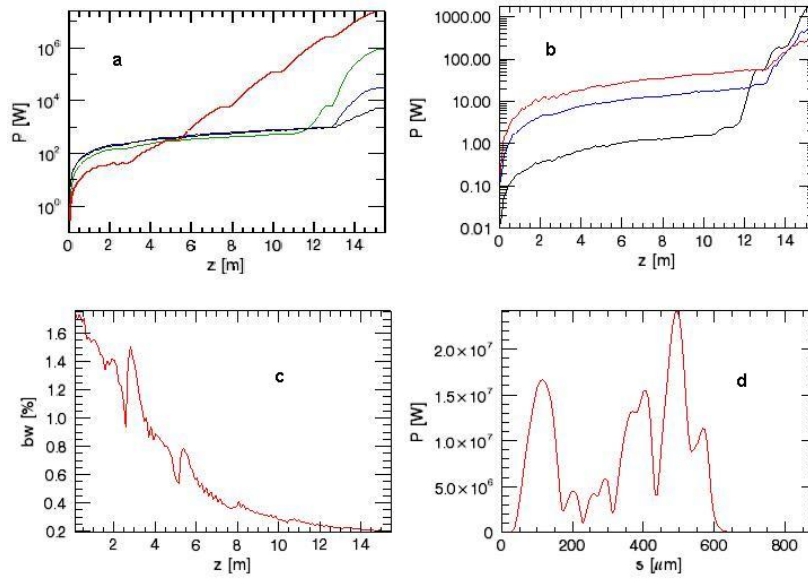


**Figure 7.1: Simulated linewidth and power evolution of the harmonics in SASE at 400nm** - In the (a) window are shown the peak power evolution of the fundamental (red) and odd harmonics the 3rd (green), 5th (blue) and 7th (black). In the (b) window are shown the peak power evolution of the even harmonics 2nd (red), 4th (blue) and 6th (black). In the (c) window is shown the linewidth evolution that reaches its minimum (0.2%) at saturation and it is comparable with the  $\rho$  value. In (d) window is shown the temporal multispikes pulse at saturation, the simulated window is only a fraction of the whole beam but it is however useful to show the behaviour of the beam and the powers of the harmonics.



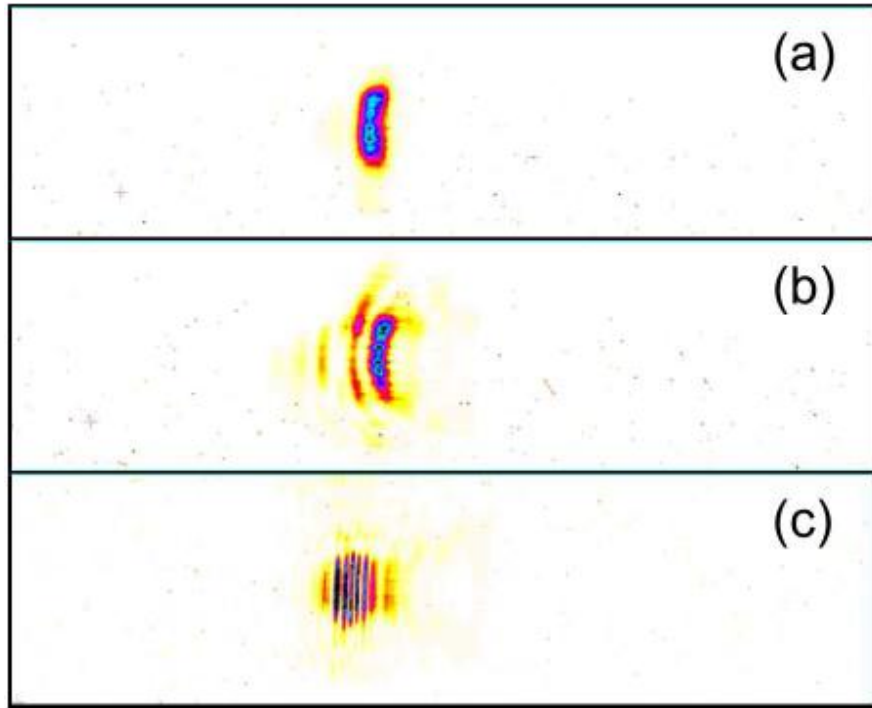


**Figure 7.2: Spectrum of the seeded amplifier with different seed energy** - Spectrum of the seeded amplifier. The horizontal axis represents the wavelength, the window range is 45 nm and the central wavelength is 400 nm. The vertical axis indicates the position on the (vertical) entrance slit of the spectrometer. The images with labels (a), (b) and (c) have been obtained with different seed energy: (a)  $E < 0.5 \mu\text{J}$ , (b)  $E \sim 3 \mu\text{J}$ , (c)  $E \sim 9 \mu\text{J}$ .

## 7. EXPERIMENTAL AND SIMULATION RESULTS OF SUPERRADIANT SINGLE SPIKE IN A HGHG-FEL

---

saturation effect. This structure may be interpreted as the effect of a saturated pulse slipping forward along the electron pulse, with the radiation emitted by fresh electrons in the pulse front, interfering with radiation out of phase produced by overbunched electrons in the rear part of the pulse. Numerical simulations have been carried out with the GENESIS 1.3, taking into account the spectral overlap and three-dimensional effects, such as the transverse mismatch. An amplification of the seed in the exponential regime in the first two sections of the undulator, and superradiance in the other four ones is observed in the simulations. One of the results obtained is shown in Fig.7.4

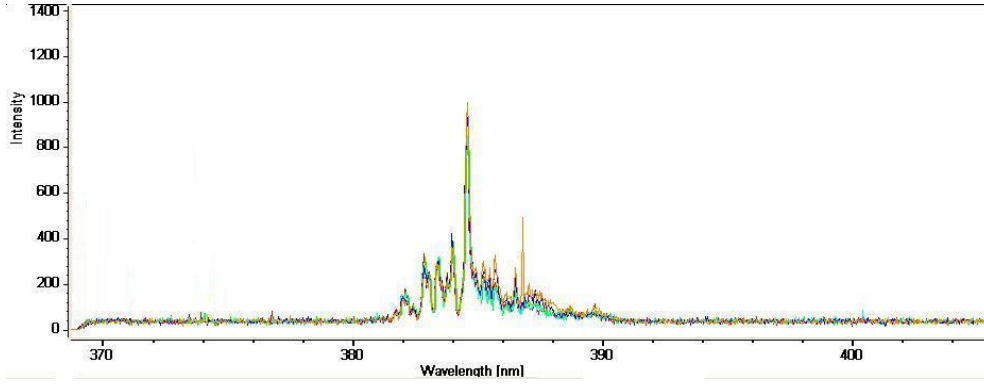


**Figure 7.3: Overlap of some measured spectra at 400nm** - The overlap of some shots of the amplified seeded pulses show the stability of the 0.5 nm modulation

where the spectrum has been deduced from GENESIS1.3. The energy measured in a sequence of 100 consecutive shots is presented in Fig.7.5. Harmonics of the fundamental frequency  $\lambda_n = \lambda_r/n$  have been observed up to  $n=11$ . The spectral emission on the harmonics presents regular Gaussian shape pulse to pulse. In fig.7.6 the spectrum from 32 up to 115 nm is shown with the presence of eight harmonics from 11th up to 4th from left (in sequence: 36.18 nm, 39.8nm, 44.2 nm, 49.75 nm, 58.6 nm, 66.3 nm, 79.6 nm, 99.5 nm). Both even and odd harmonics are visible, with the odd ones slightly more intense. The spatial shape seems to be similar to the unseeded emission. The process of coherent higher order harmonics generation in this regime of operation, i.e. with a seed pulse shorter then the e-bunch length was studied in [72]. The regime was originally analysed in ref. [73] and explored in a single pass FEL amplification experiment in [42]. It is characterized by a self similar pulse amplified while it propagates through the undulator. The main reason of the expected intense harmonics emission can be found in the structure of the front side of the pulse and in the interaction with the

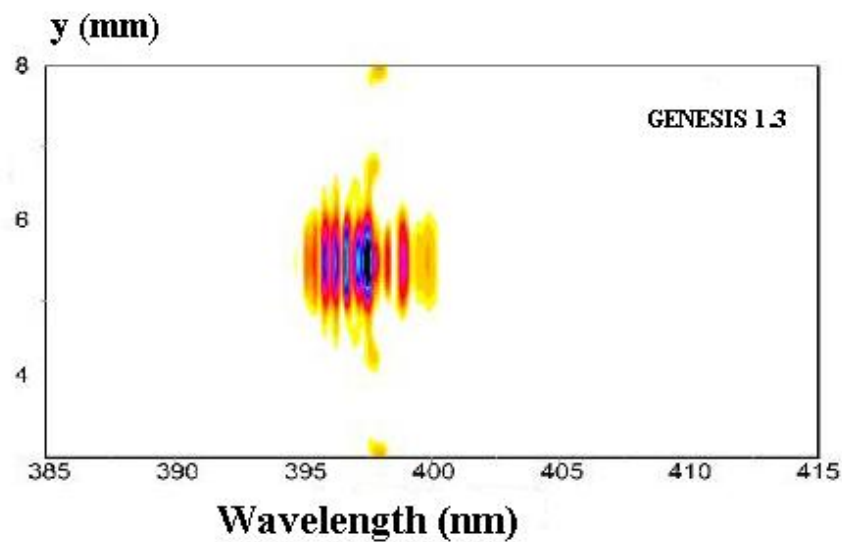


**Figure 7.4:** Reconstructed spectrum from simulation at 400 nm SEED FEL - GENESIS simulation reconstructed data, obtained with the reference parameters in Tab.7.1.

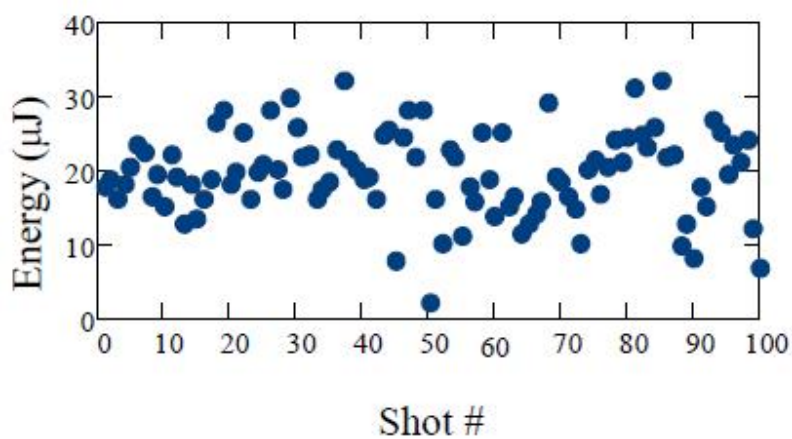


**Figure 7.5:** Experimental shot-to-shot energy of the SEED FEL at 400 nm - Energy measured in a sequence of 100 consecutive shots

## 7. EXPERIMENTAL AND SIMULATION RESULTS OF SUPERRADIANT SINGLE SPIKE IN A HGHG-FEL

---

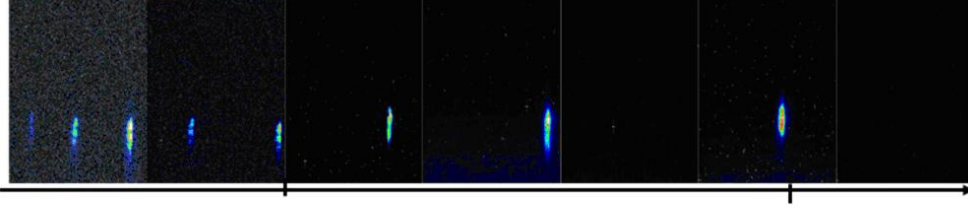


**Figure 7.6: Experimental spectrum of the HGHG FEL at SPARC** - Spectrum from 32 up to 115 nm is shown with the presence of eight harmonics from 11th up to 4th from left (in sequence: 36.18 nm, 39.8nm, 44.2 nm, 49.75 nm, 58.6 nm, 66.3 nm, 79.6 nm, 99.5 nm)

co-propagating electron beam. In Fig. 7.7(a) it is shown a plot of the short radiation pulse shifting from left to right because of slippage. In Fig.7.7(b) the expanded view of the electron beam phase space in the pulse front side (colored region in Fig.7.7(a)) and the bunching coefficients for the first harmonics, are represented. The experimental results for the eleven harmonic are shown in Fig.7.8, the mean energy content (bottom) and the bandwidth (top) for the first six harmonics are averaged on 100 shots, the others measure on the bandwidth are shot to shot to illustrate the large fluctuations. The results of Genesis simulation are shown in figs.7.9 and 7.10. The window simulated is only a fraction of the electron beam but it allows to observe the evolution of seed pulse along the beam. In Fig.7.9(left window) the amplification of the seed pulse stop it exponential gain and a first saturation at the exit of the second undulator sections is reached, after the pulse advances over fresh electrons on the right side inducing an increasing modulation and bunching while its energy continues to grow. The bunching factor at the fundamental wavelength grows from right to left until reaches the maximum value approximately at the peak of the pulse. Bunching factors at the higher order harmonics follow a similar behaviour, reaching the maximum value in a position in the pulse front side with a length scaling as  $1/n$ . Simulations predict extremely narrow pulses at the highest harmonics. Several aspects of this dynamical regime suggest an intense high harmonics emission. Saturation dynamics is governed by the slippage process. At a given position along the bunch the field grows because of slippage and not because of exponential gain. The self similar behaviour of this particular solution of the FEL dynamics causes the fact that the bunching distribution is preserved along the undulator. There is no de-bunching due to dispersion. The experimental observation confirms the predicted behaviour. The experimental results for the eleven harmonic

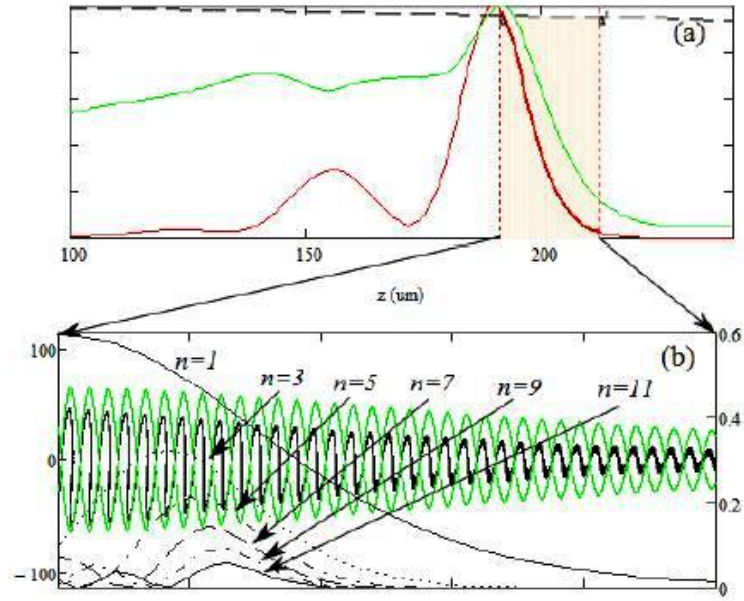


**Figure 7.7: Power pulse profile and longitudinal phase space with microbunching for the seed pulse FEL at saturation** - Graphical representation of the radiation pulse slipping from left to right in the e-beam frame (red) and of the induced energy spread (green) (Fig.7.7(a)). Longitudinal e-beam phase space in the front part of the pulse (Fig.7.7(b)). In Fig.7.7(b) the square moduli of the bunching coefficients for the first eleven (odd) harmonics are plotted. The green line represents the motion separatrix whose envelope is proportional to the square root of the laser field (simulation with PERSEO TD)(courtesy by L.Giannessi)

## 7. EXPERIMENTAL AND SIMULATION RESULTS OF SUPERRADIANT SINGLE SPIKE IN A HGHG-FEL

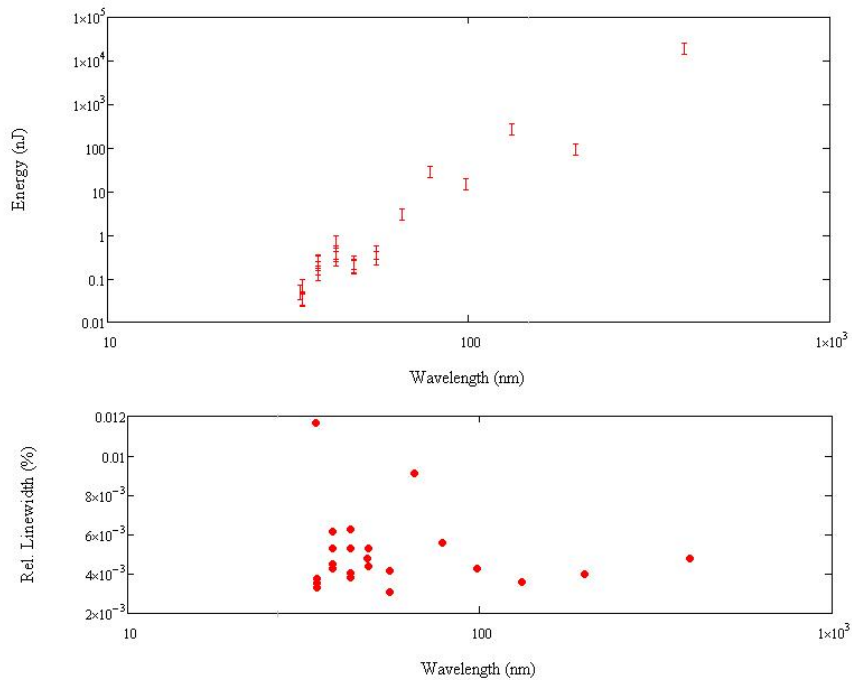


**Figure 7.8: Experimental bandwidth and energy of the first eleven harmonics in HGHG at SPARC** - Top: bandwidth of the first eleven harmonics, the value of the first six harmonics is the mean value while the last five harmonics are shot to shot. Bottom: The mean energy of the harmonics with the error bars

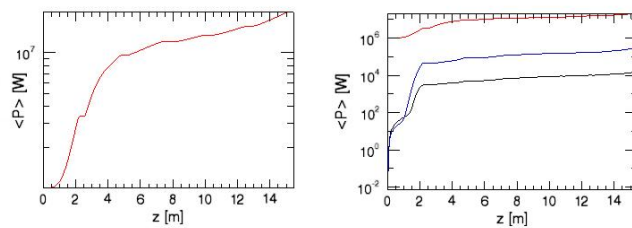


**Figure 7.9: Simulated exponential gain of fundamental wavelength** - (left plot) Mean power evolution with a simulated windows of 3ps: the changing of the slope after the first two sections of the undulator is due to the saturation, after the pulse starts to slip with  $c$  velocity over the bunch extracting other energy by the 'fresh' electrons behind it. (right plot) Log-plot of the evolution of the first three odd harmonics: fundamental (red), third (blue) and fifth (black)

## 7.2 Superradiant Spike Generation in HGHG SEED FEL

---

are shown in Fig.7.8, the mean energy content (bottom) and the bandwidth (top) for the first six harmonics are averaged on 100 shots, the others measure on the bandwidth are shot to shot to illustrate the large fluctuations. The results of Genesis simulation are shown in figs.7.9 and 7.10. The window simulated is only a fraction of the electron beam but it allows to observe the evolution of seed pulse along the beam. In Fig.7.9(left window) the amplification of the seed pulse stop it exponential gain and a first saturation at the exit of the second undulator sections is reached, after the pulse advances over fresh electrons on the right side inducing an increasing modulation and bunching while its energy continues to grow. The bunching factor at the fundamental wavelength grows from right to left until reaches the maximum value approximately at the peak of the pulse. Bunching factors at the higher order harmonics follow a similar behaviour, reaching the maximum value in a position in the pulse front side with a length scaling as  $1/n$ . Simulations predict extremely narrow pulses at the highest harmonics. Several aspects of this dynamical regime suggest an intense high harmonics emission. Saturation dynamics is governed by the slippage process. At a given position along the bunch the field grows because of slippage and not because of exponential gain. The self similar behaviour of this particular solution of the FEL dynamics causes the fact that the bunching distribution is preserved along the undulator. There is no de-bunching due to dispersion. The experimental observation confirms the predicted behaviour. In fig.7.10 we show at left the pulse of the first and third harmonic at the end of the undulator, the third harmonic is shorter than the fundamental while the bandwidth (Fig.7.10(c)) follows a similar behaviour during the superradiant evolution. In Fig.7.10(a) and (c)), are shown the fundamental and the third harmonic at saturation. The simulated energy for the first nine harmonics are, respectively from the fundamental,  $34.6 \mu\text{J}$ ,  $0.88 \text{ nJ}$ ,  $960 \text{ nJ}$ ,  $0.33 \text{ nJ}$ ,  $32.7 \text{ nJ}$ ,  $0.14 \text{ nJ}$ ,  $2.67 \text{ nJ}$ ,  $0.1 \text{ nJ}$ ,  $0.75 \text{ nJ}$ . A comparison with the experimental results, Genesis and Perseo[71] simulations are shown in Fig.7.11. The agreement with genesis simulation is very good for the odd harmonics while for the even harmonics the experimental results are systematically higher than the Genesis ones. The possible explanations on this results can come from a misalignment of the undulator sections or from the period average model, which the GENESIS and PERSEO code are based. To solve this question some experiments and numerical calculation are in progress.

## 7. EXPERIMENTAL AND SIMULATION RESULTS OF SUPERRADIANT SINGLE SPIKE IN A HGHG-FEL

---

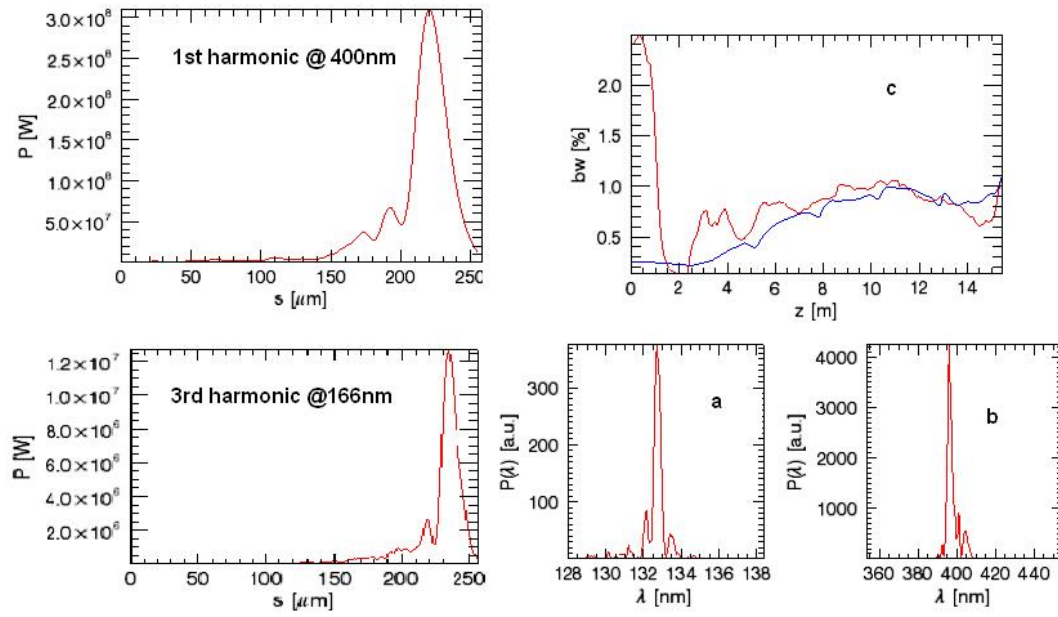


**Figure 7.10: Genesis simulation for the fundamental and the third harmonics**

- At left columns is shown the pulse shape of the first and third harmonic the width of the third is less than the half respect the first one. The (a) and (b) figures show the spectra at the end of the undulator while the evolution of the bandwidth is shown in fig.(c) the behaviour after some wavelength is similar and the bandwidth is the same magnitude(blue fundamental and red the third harm.)



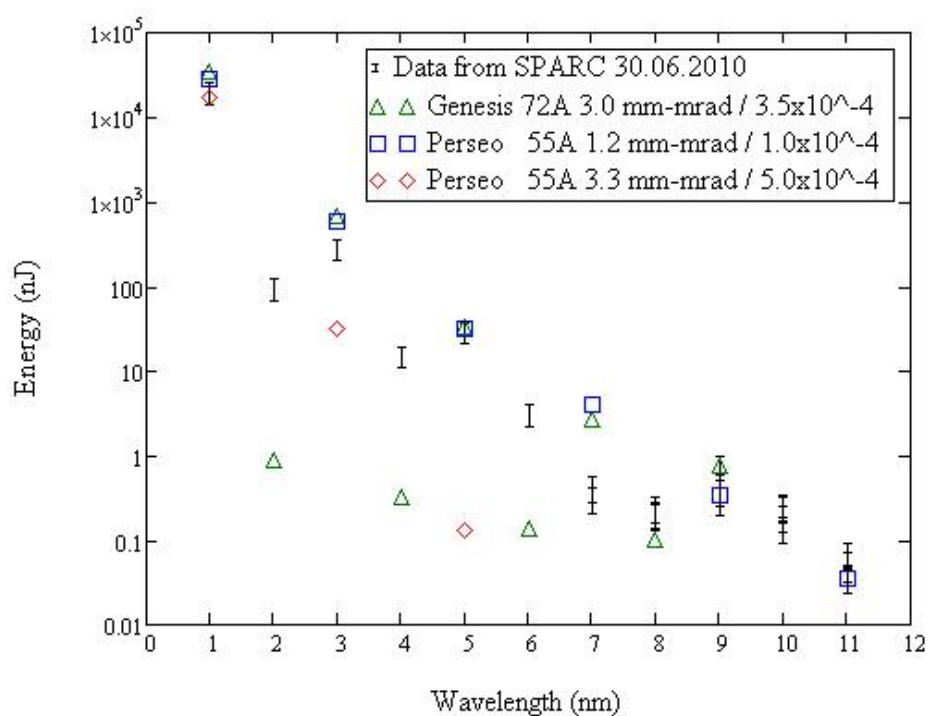


**Figure 7.11: Energy of the first eleven harmonics: experimental and simulated**  
 - Comparison between the experimental results of HGHG (data with error), Genesis for the first nine harm.(green triangle) and PERSEO for the even harm. with two different emittance (red rhombus and blue)

## **7. EXPERIMENTAL AND SIMULATION RESULTS OF SUPERRADIANT SINGLE SPIKE IN A HGHG-FEL**

---

# References

- [1] P.Emma, R.Akre, J.Arthur, R.Bionta, C.Bostedt, J.Bozek, A.Brachmann, P.Bucksbaum, R.Coffee, F.-J.Decker, Y.Ding, D.Dowell, S.Edstrom, A.Fisher, J.Frisch, S.Gilevich, J.Hastings, G.Hays, Ph.Hering, Z.Huang, R.Iverson, H.Loos, M.Messerschmidt, A.Miahnahri, S.Moeller, H.-D.Nuhn, G.Pile, D.Ratner, J.Rzepiela, D.Schultz, T.Smith, P.Stefan, H.Tompkins, J.Turner, J.Welch, W.White, J.Wu, G.Yocky, and J.Galayda, “First lasing and operation of an angstrom-wavelength free-electron laser,” *Nat Photon* **4** (2010), no. 9 641–647. 1
- [2] J. M. Glownia, J. Cryan, J. Andreasson, A. Belkacem, N. Berrah, C. I. Blaga, C. Bostedt, J. Bozek, L. F. DiMauro, L. Fang, J. Frisch, O. Gessner, M. Ghr, J. Hajdu, M. P. Hertlein, M. Hoener, G. Huang, O. Kornilov, J. P. Marangos, A. M. March, B. K. McFarland, H. Merdji, V. S. Petrovic, C. Raman, D. Ray, D. A. Reis, M. Trigo, J. L. White, W. White, R. Wilcox, L. Young, R. N. Coffee, and P. H. Bucksbaum, “Time-resolved pump-probe experiments at the LCLS,” *Optics Express* **18** (2010), no. 17 17620–17630. 2
- [3] L.Palumbo, M. Ferrario, A. Bacci, M. Bellaveglia, R. Boni, M. Boscolo, M. Castellano, E. Chiadroni, A. Cianchi, L. Cultrera, G. D. Pirro, L. Ficcadenti, D. Filippetto, V. Fusco, A. Gallo, G. Gatti, L. Giannessi, M. Labat, B. Marchetti, C. Marrelli, M. Migliorati, A. Mostacci, E. Pace, L. Palumbo, M. Quattromini, C. Ronsivalle, A. R. Rossi, J. Rosenzweig, L. Serafini, M. Serluca, B. Spataro, C. Vaccarezza, and C. Vicario, “Sparc team : ‘sparc tdr’,” SPARC Technical Design Report 1, Laboratori Nazionali di Frascati LNF, <http://www.lnf.infn.it/acceleratori/sparc>, May, 2002. 2
- [4] M. Ferrario, J. E. Clendenin, D. T. Palmer, J. B. Rosenzweig, and L. Serafini, “Homdyn study for the lcls rf photo-injector,” *SLAC-PUB 8400* (March, 2000). 3, 59, 68
- [5] E. L. Saldin, E. A. Schneidmiller, and M. V. Yurkov, “Self-amplified spontaneous emission FEL with energy-chirped electron beam and its application for generation of attosecond x-ray pulses,” *Physical Review Special Topics - Accelerators and Beams* **9** (May, 2006) 050702. 3, 37, 82
- [6] V. Petrillo, I. Boscolo, A. Bacci, M. Boscolo, M. Ferrario, M. Serluca, L. Giannessi, and C. Ronsivalle, “Analysis of single-spike FEL visible radiation from three-dimensional and realistic beams,” *Nuclear Instruments and Methods in Physics Research Section A: Accelerators, Spectrometers, Detectors and Associated Equipment* **621** (Sept., 2010) 1–14. 3, 6
- [7] S. Reiche, “GENESIS 1.3: a fully 3D time-dependent FEL simulation code,” *Nuclear Instruments and Methods in Physics Research Section A: Accelerators, Spectrometers, Detectors and Associated Equipment* **429** (June, 1999) 243–248. 3, 5, 39, 42
- [8] A. Bacci, F. Broggi, C. DeMartinis, D. Giove, C. Maroli, V. Petrillo, A. Rossi, L. Serafini, P. Tomassini, L. Cultrera, G. D. Pirro, M. Ferrario, D. Filippetto, G. Gatti, E. Pace, C. Vaccarezza, C. Vicario, F. Bosi, D. Giulietti, L. Gizzi, and P. Oliva, “Status of thomson source at SPARC/PLASMONX,” *Nuclear Instruments and Methods in Physics Research Section A: Accelerators, Spectrometers, Detectors and Associated Equipment* **608** (Sept., 2009) S90–S93. 3
- [9] L.N.F., “Sparc team : First lasing at sparc,” *Proceedings of FEL conference 2009* (2009). 3
- [10] M. Ferrario, A. Bacci, M. Bellaveglia, R. Boni, M. Boscolo, M. Castellano, E. Chiadroni, A. Cianchi, L. Cultrera, G. D. Pirro, L. Ficcadenti, D. Filippetto, V. Fusco, A. Gallo, G. Gatti, L. Giannessi, M. Labat, B. Marchetti, C. Marrelli, M. Migliorati, A. Mostacci, E. Pace, L. Palumbo, M. Quattromini, C. Ronsivalle, A. R. Rossi, J. Rosenzweig, L. Serafini, M. Serluca, B. Spataro, C. Vaccarezza, and C. Vicario, “Experimental demonstration of emittance compensation with velocity bunching,” *Physical Review Letters* **104** (feb, 2010) 054801. 3, 6, 67
- [11] M. Ferrario, D. Alesini, A. Bacci, M. Bellaveglia, R. Boni, M. Boscolo, P. Calvani, M. Castellano, E. Chiadroni, A. Cianchi, L.Cultrera, G.DiPirro, L.Ficcadenti, D.Filippetto, A.Gallo, G.Gatti, L.Giannessi, M.Labat, S.Lupi, B.Marchetti, C.Marrelli, M.Migliorati, A.Mostacci, D.Nicoletti, E.Pace, L.Palumbo, V.Petrillo, M.Quattromini, C.Ronsivalle, A. J.Rosenzweig, L.Serafini, M.Serluca, B.Spataro, H.Tomizawa, C.Vaccarezza, and C.Vicario, “Laser comb with velocity bunching: Preliminary results at SPARC,” *Nuclear Instruments and Methods in Physics Research Section A: Accelerators, Spectrometers, Detectors and Associated Equipment* (2010). 4

## REFERENCES

---

- [12] L. Giannessi, F. Ciocci, G. Dattoli, M. D. Franco, A. Petralia, M. Quattromini, C. Ronsivalle, E. Sabia, I. Spassovsky, V. Surrenti, M. Bougeard, B. Carr, M. Moreno, M. Serluca, D. Alesini, M. Bellaveglia, M. Castellano, E. Chiadroni, L. Cultrera, G. D. Pirro, M. Ferrario, L. Ficcadenti, D. Filippetto, A. Gallo, G. Gatti, E. Pace, B. Spataro, C. Vaccarezza, C. Vicario, J. V. Rau, V. R. Albertini, A. Bacci, V. Petrillo, A. R. Rossi, L. Serafini, G. Lambert, F. Frassetto, L. Poletto, A. Mostacci, F. Briquez, M.-E. Couprie, M. Labat, G. Marcus, J. Rosenzweig, and A. Cianchi, "Sparc operation in seeded and chirped mode," in *Proceedings of FEL conference 2010*, 2010. 4, 7, 37, 63
- [13] L. Giannessi, F. Ciocci, G. Dattoli, M. D. Franco, A. Petralia, M. Quattromini, C. Ronsivalle, E. Sabia, I. Spassovsky, V. Surrenti, M. Bougeard, B. Carr, M. Moreno, M. Serluca, D. Alesini, M. Bellaveglia, M. Castellano, E. Chiadroni, L. Cultrera, G. D. Pirro, M. Ferrario, L. Ficcadenti, D. Filippetto, A. Gallo, G. Gatti, E. Pace, B. Spataro, C. Vaccarezza, C. Vicario, J. V. Rau, V. R. Albertini, A. Bacci, V. Petrillo, A. R. Rossi, L. Serafini, G. Lambert, F. Frassetto, L. Poletto, A. Mostacci, F. Briquez, M.-E. Couprie, M. Labat, G. Marcus, J. Rosenzweig, and A. Cianchi, "Self-amplified spontaneous emission free-electron laser with energy chirped electron beam and undulator tapering," *Physical Review Letters* **submitted to PRL** (2010). 4, 7
- [14] P. Salieres and M. Lewenstein, "Generation of ultrashort coherent XUV pulses by harmonic conversion of intense laser pulses in gases: towards attosecond pulses,". 4, 38
- [15] G. Lambert, T. Hara, D. Garzella, T. Tanikawa, M. Labat, B. Carre, H. Kitamura, T. Shintake, M. Bougeard, S. Inoue, Y. Tanaka, P. Salieres, H. Merdji, O. Chubar, O. Gobert, K. Tahara, and M. Couprie, "Injection of harmonics generated in gas in a free-electron laser providing intense and coherent extreme-ultraviolet light," *Nat Phys* **4** (Apr., 2008) 296–300. 4, 38
- [16] L. Giannessi, F. Ciocci, G. Dattoli, M. D. Franco, A. Petralia, M. Quattromini, C. Ronsivalle, E. Sabia, I. Spassovsky, V. Surrenti, M. Bougeard, B. Carr, M. Moreno, M. Serluca, D. Alesini, M. Bellaveglia, M. Castellano, E. Chiadroni, L. Cultrera, G. D. Pirro, M. Ferrario, L. Ficcadenti, D. Filippetto, A. Gallo, G. Gatti, E. Pace, B. Spataro, C. Vaccarezza, C. Vicario, J. V. Rau, V. R. Albertini, A. Bacci, V. Petrillo, A. R. Rossi, L. Serafini, G. Lambert, F. Frassetto, L. Poletto, A. Mostacci, F. Briquez, M.-E. Couprie, M. Labat, G. Marcus, J. Rosenzweig, and A. Cianchi, "Fel experiments at sparc," in *Proceedings of FEL conference 2010*, 2010. 4, 7
- [17] M. Xie, "Exact and variational solutions of 3D eigenmodes in high gain FELs," *Nuclear Instruments and Methods in Physics Research Section A: Accelerators, Spectrometers, Detectors and Associated Equipment* **445** (May, 2000) 59–66. 5, 9, 28
- [18] R. Bonifacio, C. Maroli, and N. Piovella, "Slippage and superradiance in the high-gain FEL: linear theory," *Optics Communications* **68** (1988), no. 5 369–374. 10, 32
- [19] R. Bonifacio, L. D. Salvo, P. Pierini, N. Piovella, and C. Pellegrini, "Spectrum, temporal structure, and fluctuations in a high-gain free-electron laser starting from noise," *Phys. Rev. Lett.* **73** (July, 1994) 70–73. 10, 31, 32, 34, 37, 45
- [20] S. Reiche, *Numerical Studies for a Single Pass High Gain Free-Electron Laser*. PhD thesis, Hamburg, 1999. 11, 22, 23
- [21] W. B. Colson, "One-body electron dynamics in a free electron laser," *Physics Letters A* **64** (Dec., 1977) 190–192. 14
- [22] Z. Huang and K. Kim, "Review of x-ray free-electron laser theory," *Phys. Rev. ST Accel. Beams* **10** (Mar, 2007) 034801. 15, 18, 25, 35
- [23] J. M. J. Madey, "Stimulated emission of bremsstrahlung in a periodic magnetic field," *Journal of Applied Physics* **42** (1971), no. 5 1906. 16
- [24] C. Rulliere, *Femtosecond Laser Pulses: Principles and Experiments*. Springer, 2nd ed., Oct., 2004. 17
- [25] R. Bonifacio, C. Pellegrini, and L. Narducci, "Collective instabilities and high-gain regime in a free electron laser," *Optics Communications* **50** (1984), no. 6 373–378. 19, 22
- [26] A. Gover and Z. Livni, "Operation regimes of Cerenkov-Smith-Purcell free electron lasers and T.W. amplifiers," *Optics Communications* **26** (Sept., 1978) 375–380. 22
- [27] G. Schmidt, *Physics of High Temperature Plasmas*. Academic Pr, 2 ed., June, 1979. 22
- [28] K. Kim, "Three-Dimensional analysis of coherent amplification and Self-Amplified spontaneous emission in Free-Electron lasers," *Physical Review Letters* **57** (Oct., 1986) 1871. 23, 24
- [29] R. Bonifacio, L. D. Salvo, and P. Pierini, "Large harmonic bunching in a high-gain free-electron laser," *Nuclear Instruments and Methods in Physics Research Section A: Accelerators, Spectrometers, Detectors and Associated Equipment* **293** (Aug., 1990) 627–629. 25
- [30] Z. Huang and K. Kim, "Nonlinear harmonic generation of coherent amplification and self-amplified spontaneous emission," *Nuclear Instruments and Methods in Physics Research Section A: Accelerators, Spectrometers, Detectors and Associated Equipment* **475** (Dec., 2001) 112–117. 25

## REFERENCES

- 
- [31] S. G. Biedron, R. J. Dejus, Z. Huang, S. V. Milton, V. Sajaev, W. Berg, M. Borland, P. K. D. Hartog, M. Erdmann, W. M. Fawley, H. P. Freund, E. Gluskin, K. J. Kim, J. W. Lewellen, Y. Li, A. H. Lumpkin, E. R. Moog, A. Nassiri, G. Wiemerslage, and B. X. Yang, "Measurements of nonlinear harmonic generation at the advanced photon source's SASE FEL," *Nuclear Instruments and Methods in Physics Research Section A: Accelerators, Spectrometers, Detectors and Associated Equipment* **483** (May, 2002) 94–100. 25
  - [32] A. Tremaine, X. J. Wang, M. Babzien, I. Ben-Zvi, M. Cornacchia, H. Nuhn, R. Malone, A. Murokh, C. Pellegrini, S. Reiche, J. Rosenzweig, and V. Yakimenko, "Experimental characterization of nonlinear harmonic radiation from a visible Self-Amplified spontaneous emission Free-Electron laser at saturation," *Physical Review Letters* **88** (May, 2002) 204801. 25
  - [33] D. A. Edwards and M. J. Syphers, *An Introduction to the Physics of High Energy Accelerators*. Wiley-VCH, Nov., 1992. 26
  - [34] S. Krinsky and L. H. Yu, "Output power in guided modes for amplified spontaneous emission in a single-pass free-electron laser," *Physical Review A* **35** (Apr., 1987) 3406. 27, 32
  - [35] E. T. Scharlemann, A. M. Sessler, and J. S. Wurtele, "Optical guiding in a Free-Electron laser," *Physical Review Letters* **54** (Apr., 1985) 1925. 27
  - [36] D. Prosnitz, A. Szoke, and V. K. Neil, "High-gain, free-electron laser amplifiers: Design considerations and simulation," *Physical Review A* **24** (1981), no. 3 1436. 27
  - [37] G. Moore, "High-gain small-signal modes of the free-electron laser," *Optics Communications* **52** (Nov., 1984) 46–51. 27
  - [38] R. Dicke, "Coherence in spontaneous radiation processes," *Physical Review* **93** (1954), no. 1 99–110. 29
  - [39] K. Kim and S. J. Hahn, "Finite pulse effects in self-amplified-spontaneous-emission," *Nuclear Instruments and Methods in Physics Research Section A: Accelerators, Spectrometers, Detectors and Associated Equipment* **358** (Apr., 1995) 93–95. 31
  - [40] N. Piovella, R. Bonifacio, and W. Barletta, "A multi-frequency approach to free electron lasers driven by short electron bunches," in *The workshop on single pass, high gain FELs starting from noise, aiming at coherent x-rays*, vol. 413, (Garda Lake (Italy)), pp. 205–218, AIP, June, 1997. 31
  - [41] R. Bonifacio and F. Casagrande, "The superradiant regime of a free electron laser," *Nuclear Instruments and Methods in Physics Research Section A: Accelerators, Spectrometers, Detectors and Associated Equipment* **239** (Aug., 1985) 36–42. 31, 32, 45, 46
  - [42] T. Watanabe, X. J. Wang, J. B. Murphy, J. Rose, Y. Shen, T. Tsang, L. Giannessi, P. Musumeci, and S. Reiche, "Experimental characterization of superradiance in a Single-Pass High-Gain Laser-Seeded Free-Electron laser amplifier," *Physical Review Letters* **98** (Jan., 2007) 034802. 31, 102
  - [43] D. A. Jaroszynski, P. Chaix, N. Piovella, D. Oepts, G. M. H. Knippels, A. F. G. van der Meer, and H. H. Weits, "Superradiance in a Short-Pulse Free-Electron-Laser oscillator," *Physical Review Letters* **78** (Mar., 1997) 1699. 31
  - [44] J. Goodman, *Statistical Optics*. John Wiley and Sons, New York, 1985. 36
  - [45] P. Emma, "Issues and challenges for short pulse radiation production," in *2004 European Particle Accelerator Conference (EPAC)*, (Lucerne, Switzerland), p. 225, 2004. 37
  - [46] L. Yu, "Generation of intense uv radiation by subharmonically seeded single-pass free-electron lasers," *Physical Review A* **44** (Oct., 1991) 5178. 38
  - [47] L. H. Yu, L. DiMauro, A. Doyuran, W. S. Graves, E. D. Johnson, R. Heese, S. Krinsky, H. Loos, J. B. Murphy, G. Rakowsky, J. Rose, T. Shafan, B. Sheehy, J. Skaritka, X. J. Wang, and Z. Wu, "First ultraviolet High-Gain Harmonic-Generation Free-Electron laser," *Physical Review Letters* **91** (2003), no. 7 074801. 38
  - [48] J. Feldhaus, E. L. Saldin, J. R. Schneider, E. A. Schneidmiller, and M. V. Yurkov, "Method for reducing the radiation bandwidth of an x-ray FEL," *AIP Conference Proceedings* **413** (June, 1997) 219–230. 38
  - [49] M. Boscolo, M. Ferrario, I. Boscolo, F. Castelli, S. Cialdi, V. Petrillo, R. Bonifacio, L. Palumbo, and L. Serafini, "Single spike operation in SPARC SASE-FEL," *Nuclear Instruments and Methods in Physics Research Section A: Accelerators, Spectrometers, Detectors and Associated Equipment* **593** (Aug., 2008) 137–142. 39, 50
  - [50] S. Reiche, P. Musumeci, C. Pellegrini, and J. Rosenzweig, "Development of ultra-short pulse, single coherent spike for SASE x-ray FELs," *Nuclear Instruments and Methods in Physics Research Section A: Accelerators, Spectrometers, Detectors and Associated Equipment* **593** (Aug., 2008) 45–48. 39

## REFERENCES

---

- [51] M. Ferrario, D. Alesini, A. Bacci, M. Bellaveglia, R. Boni, M. Boscolo, M. Castellano, L. Catani, E. Chiadroni, S. Cialdi, A. Cianchi, A. Clozza, L. Cultrera, G. D. Pirro, A. Drago, A. Esposito, L. Ficcadenti, D. Filippetto, V. Fusco, A. Gallo, G. Gatti, A. Ghigo, L. Giannessi, C. Ligi, M. Mattioli, M. Migliorati, A. Mostacci, P. Musumeci, E. Pace, L. Palumbo, L. Pellegrino, M. Petrarca, M. Quattromini, R. Ricci, C. Ronsivalle, J. Rosenzweig, A. R. Rossi, C. Sanelli, L. Serafini, M. Serio, F. Sgamma, B. Spataro, F. Tazzioli, S. Tomassini, C. Vaccarezza, M. Vescovi, and C. Vicario, "Direct measurement of the double emittance minimum in the beam dynamics of the sparc High-Brightness photoinjector," *Physical Review Letters* **99** (Dec., 2007) 234801. 48
- [52] L. Young, "Pamela," *LANL Report NoLA-UR-96-1835* **96** (1996) 1835. 48, 75
- [53] K. Floetmann, "Astra," *DESY Internal report* **00** (2000). 48
- [54] A. Bacci, C. Maroli, V. Petrillo, A. Rossi, and L. Serafini, "Maximizing the brightness of an electron beam by means of a genetic algorithm," *Nuclear Instruments and Methods in Physics Research Section B: Beam Interactions with Materials and Atoms* **263** (Oct., 2007) 488–496. 50
- [55] J. Kim, F. Ludwig, J. Chen, Z. Zhang, and F. X. Karten, "Femtosecond synchronization and stabilization techniques," *Proc. FEL06, Berlin* (2006). 59
- [56] M. Bellaveglia, C. Vicario, A. Drago, A. Gallo, A. Ghigo, L. Cacciotti, G. Gatti, P. Musumeci, and M. Petrarca, "Laser timing and synchronization measurement at sparc," *SPARC-LS-06/001* (2006). 59
- [57] L. Ficcadenti, L. Palumbo, A. Mostacci, D. Alesini, C. Vaccarezza, G. D. Pirro, and J. Rosenzweig, "RF measurements results of the final brazed SPARC RF deflector," in *2007 IEEE Particle Accelerator Conference (PAC)*, (Albuquerque, NM), pp. 3994–3996, 2007. 61
- [58] M. Quattromini, M. DelFranco, L. Giannessi, M. Labat, E. Sabia, and V. Surrenti, "Detailed k and phase error analysis of the sparc undulator," *SPARC Note FEL/09/005* (2009). 62
- [59] L. Poletto, G. Tondello, S. D. Silvestri, M. Nisoli, S. Stagira, P. Musumeci, M. Petrarca, M. Couprie, G. Lambert, H. Merdji, P. Breger, D. Garzella, J. Hergott, P. Monchicourt, P. Salieres, B. Carr, D. Alesini, M. Biagini, A. Clozza, G. D. Pirro, A. Drago, M. Ferrario, V. Fusco, S. Gallo, A. Ghigo, V. Lollo, M. Migliorati, L. Palumbo, L. Pellegrino, C. Sanelli, F. Sgamma, B. Spataro, C. Vaccarezza, C. Vicario, L. Serafini, M. Carpanese, F. Ciocci, G. Dattoli, A. Dipace, A. Doria, G. P. Gallerano, L. Giannessi, E. Giovenale, P. L. Ottaviani, G. Parisi, I. Spassovsky, M. Quattromini, S. Pagnutti, A. Renieri, C. Ronsivalle, E. Sabia, S. Spampanati, E. Campana, G. Ronci, and M. Sassi, "1st technical design report for the seeding@sparc experiment," *EUROFEL-Report-2005-DS4-008* (2005). 63
- [60] G. Marcus, G. Andonian, A. Fukasawa, S. Reiche, J. B. Rosenzweig, L. Giannessi, M. Ferrario, and L. Palumbo, "Longitudinal diagnostic for single- spike sase fel operation in sparc," in *Proceedings of FEL conference 2008*, 2008. 65
- [61] C. Limborg-Deprey and P. R. Bolton, "Optimum electron distributions for space charge dominated beams in photoinjectors," *Nuclear Instruments and Methods in Physics Research Section A: Accelerators, Spectrometers, Detectors and Associated Equipment* **557** (Feb., 2006) 106–116. 68
- [62] O. J. Luiten, S. B. van der Geer, M. J. de Loos, F. B. Kiewiet, and M. J. van der Wiel, "How to realize uniform Three-Dimensional ellipsoidal electron bunches," *Physical Review Letters* **93** (2004), no. 9 094802. 68
- [63] L. Serafini and J. B. Rosenzweig, "Envelope analysis of intense relativistic quasilaminar beams in rf photoinjectors: mA theory of emittance compensation," *Physical Review E* **55** (June, 1997) 7565. 68, 73
- [64] P. Musumeci, J. T. Moody, R. J. England, J. B. Rosenzweig, and T. Tran, "Experimental generation and characterization of uniformly filled ellipsoidal Electron-Beam distributions," *Physical Review Letters* **100** (June, 2008) 244801. 68
- [65] K. L. F. Bane, F. Decker, Y. Ding, D. Dowell, P. Emma, J. Frisch, Z. Huang, R. Iverson, C. Limborg-Deprey, H. Loos, H. Nuhn, D. Ratner, G. Stupakov, J. Turner, J. Welch, and J. Wu, "Measurements and modeling of coherent synchrotron radiation and its impact on the linac coherent light source electron beam," *Physical Review Special Topics - Accelerators and Beams* **12** (Mar., 2009) 030704. 70
- [66] B. Carlsten, "New photoelectric injector design for the los alamos national laboratory XUV FEL accelerator," *Nuclear Instruments and Methods in Physics Research Section A: Accelerators, Spectrometers, Detectors and Associated Equipment* **285** (Dec., 1989) 313–319. 72
- [67] L. Serafini and M. Ferrario, "Velocity bunching in photo-injectors," *AIP Conference Proceedings* **581** (2001), no. 1 87–106. 72
- [68] S. Reiche, P. Musumeci, and K. Goldammer, "Recent upgrate to the free-electron laser code genesis1.3," in *Proceedings of PAC 2007*, 2007. 79, 97

## REFERENCES

---

- [69] Z. Huang and S. Krinsky, “Femtosecond x-ray pulses from a frequency-chirped SASE FEL,” *Nuclear Instruments and Methods in Physics Research Section A: Accelerators, Spectrometers, Detectors and Associated Equipment* **528** (Aug., 2004) 28–33. 82
- [70] S. J. Hahn and J. K. Lee, “Nonlinear short-pulse propagation in a free-electron laser,” *Physical Review E* **48** (1993), no. 3 2162. 84
- [71] L. Giannessi, “Perseo fel simulator,” in *PERSEO*, 2000. 97, 107
- [72] L. Giannessi, P. Musumeci, and S. Spampinati, “Nonlinear pulse evolution in seeded free-electron laser amplifiers and in free-electron laser cascades,” *Journal of Applied Physics* **98** (2005), no. 4 043110. 102
- [73] R. Bonifacio, B. W. J. McNeil, and P. Pierini, “Superradiance in the high-gain free-electron laser,” *Physical Review A* **40** (Oct., 1989) 4467. 102